Design and Evaluation of a Flutter-Suppression Control System for a High-Aspect-Ratio Wing

by

Shaneel Jivan

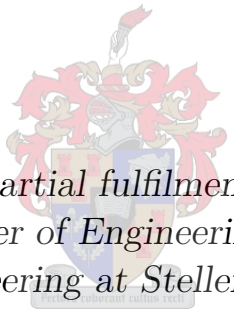

Thesis presented in partial fulfilment of the requirements for the degree of Master of Engineering (Mechanical) in the Faculty of Engineering at Stellenbosch University

Supervisor: Prof. G. Venter
Co-supervisor: Prof. S.J. van der Spuy

March 2017

Declaration

By submitting this thesis electronically, I declare that the entirety of the work contained therein is my own, original work, that I am the sole author thereof (save to the extent explicitly otherwise stated), that reproduction and publication thereof by Stellenbosch University will not infringe any third party rights and that I have not previously in its entirety or in part submitted it for obtaining any qualification.

Date: March 2017 .....

Abstract

Design and Evaluation of a Flutter-Suppression Control System for a High-Aspect-Ratio Wing

S. Jivan

Department of Mechanical and Mechatronic Engineering,
University of Stellenbosch,
Private Bag X1, Matieland 7602, South Africa.

Thesis: MEng (Mech)

March 2017

Flutter is a form of aeroelastic instability. This instability is prevalent among aircraft which use high-aspect-ratio wings. Previous studies have been conducted in which control surfaces were used to suppress flutter using mathematical models to perform the aeroelastic analysis. This thesis documents the design and evaluation of a flutter-suppression control system for a high-aspect-ratio wing. The project made use of ANSYS software where a numerical Fluid-Structure Interaction (FSI) model was established and used in performing the aeroelastic analysis. The goal of the active controller was to suppress flutter by regulating the wing tip displacement with the use of control surfaces. A Linear Quadratic (LQ) controller was constructed and embedded within the FSI model using ANSYS Parametric Design Language (APDL) scripting. Initial simulations indicated that a translational base excitation could not induce aeroelastic instability. However, a rotational base excitation proved to successfully excite flutter. Open- and closed-loop simulations were performed at a velocity of 50 m/s. Open-loop simulations indicated that the wing tip displacement was observed to grow without bound. The closed-loop simulations indicated that the LQ controller displayed the capability to suppress flutter by increasing the aerodynamic damping of the system. Non-classical flutter was encountered at a velocity of 70 m/s.

Uittreksel

Ontwerp en Evaluering van 'n Beheerstelsel vir Fladderonderdrukking van 'n Vlerk met Hoë Slankheidsverhouding.

("Design and Evaluation of a Flutter-Suppression Control System for a High-Aspect-Ratio Wing")

S. Jivan

Departement Meganiese en Megatroniese Ingenieurswese,
Universiteit van Stellenbosch,
Privaatsak X1, Matieland 7602, Suid Afrika.

Tesis: MIng (Meg)

Maart 2017

Fladder is 'n vorm van aëroelastiese onstabiliteit. Hierdie onstabiliteit is algemeen onder vliegtuie wat vlerke met 'n hoë slankheidsverhouding gebruik. Vorige studies behels die gebruik van beheeroppervlaktes om fladder met behulp van wiskundige modelle te onderdruk ten einde 'n aëroelastiese analise uit te voer. Hierdie tesis dokumenteer die ontwerp en evaluering van 'n beheerstelsel vir fladderonderdrukking. Dié projek het van ANSYS-sagteware gebruik gemaak om 'n numeriese model vir vloei-struktuur-interaksie (Fluid-Structure Interaction [FSI]) daar te stel en te gebruik tydens die aëroelastiese analise. Die doel van die aktiewe beheerder was om fladder te onderdruk deur die vlerkpunt-verplasing met behulp van beheeroppervlaktes te reguleer. 'n Lineêr-kwadratiese (Linear Quadratic [LQ]) beheerder is saamgestel en ingebed in die FSI-model deur gebruik te maak van ANSYS se Parametriese Ontwerptaal (Parametric Design Language [APDL]). Aanvanklike simulasies het aangedui dat 'n verplasings basisopwekking nie aëroelastiese onstabiliteit kon induseer nie. Daar is egter bewys dat 'n rotasie-basisopwekking wel fladder kon opwek. Ope en geslote lus-simulasies is teen 'n snelheid van 50 m/s uitgevoer. Ope lus-simulasies het aangedui dat vlerkpunt-verplasing oneindig toeneem. Geslote lus-simulasies het aangedui dat die lineêr-kwadratiese beheerder die kapasiteit vertoon om fladder te onderdruk deur die aërodinamiese demping van die sisteem te verhoog. Nie-klassieke fladder is teen 'n snelheid van 70 m/s teëgekom.

Acknowledgements

The author would like to thank the following individuals and entities for their contributions to the thesis.

- Prof. Gerhard Venter and Prof. Johan van der Spuy for their continued support and guidance throughout the span of the project
- Prof. Thomas Jones for providing the funding for the project
- ARMSCOR for sponsoring the project
- Charl Moller for assisting with the High Performance Computing facility
- Dawais Marais and his colleagues from Qfinsoft
- My family and friends for their support and proof reading the thesis on such short notice

Contents

List of Figures

List of Tables

Nomenclature

Scalar variables

A	Aerofoil area
c	Chord length
E	Young's modulus
e	Measured error
f	Frequency
f_d	Damped frequency
I	Area moment of inertia
J	Infinite horizon cost function
k	Turbulent kinetic energy
h_d	Characteristic length
p	Fluid pressure
S	Surface area
s	Spring constant
t	Time
u	Input-signal
V	Volume
v	Fluid velocity
Y	Amplitude

y	System output

α	Mass-proportional damping coefficient
β	Stiffness-proportional damping coefficient
δ	Kronecker delta
ϵ	Dissipation rate
Γ	Diffusion coefficient
μ	Dynamic viscosity
μ_t	Turbulent eddy viscosity
ω	Specific dissipation rate
ρ	Density
ξ	Damping ratio

Vectors and Matrices

$\mathbf{B}$	Strain-displacement matrix
$\mathbf{C}$	Damping matrix
$\mathbf{d}$	Degree of freedom vector
$\mathbf{E}$	Direct transmission term
$\mathbf{F}$	System matrix
$\mathbf{f}$	Body force vector
$\mathbf{G}$	Input matrix
$\mathbf{H}$	Output matrix
$\mathbf{K}$	Stiffness matrix
$\mathbf{K}_{Gain}$	Controller gain vector
$\mathbf{L}$	State estimator gain vector

$\mathbf{M}$	Mass matrix
$\mathbf{N}$	Shape function
$\mathbf{p}$	Concentrated load vector
$\mathbf{r}$	Load force vector
$\mathbf{s}$	Node displacement vector
$\mathbf{u}$	Input-signal vector
$\boldsymbol{\varepsilon}$	Node strain vector
Φ	Surface traction vector
$\boldsymbol{\sigma}$	Stress vector

Subscripts and superscripts

$\dot{(\bullet)}$	First derivative
$\tilde{(\bullet)}$	Estimate of value
$\overline{(\bullet)}$	Mean component of value
$(\bullet)'$	Fluctuating component of value
$(\bullet)_\infty$	Free-stream velocity
$(\bullet)_{ext}$	External source
$(\bullet)_{int}$	Internal source
$(\bullet)_{\mathbf{e}}$	Local element form
$(\bullet)_c$	Centroid axis
$(\bullet)_l$	Lower aerofoil surface
$(\bullet)_u$	Upper aerofoil surface
$(\bullet)_i, (\bullet)_k$	Node numbers
$(\bullet)_F$	Property of fluid environment
$(\bullet)_S$	Property of structural environment

$(\bullet)_x, (\bullet)_y, (\bullet)_z$ Cartesian components

$(\bullet)^j$ Number of stagger-iteration

$(\bullet)^N$ Number of time-step

$(\bullet)^T$ Matrix transpose

$(\bullet)^+$ Wall coordinate

Abbreviations

APDL ANSYS Parametric Design Language

CAD Computer Aided Design

CFD Computational Fluid Dynamics

DARE Discrete Time Algebraic Ricatti Equation

DOF Degree of Freedom

FE Finite Element

FSI Fluid-Structure Interaction

LQ Linear Quadratic

MIMO Multiple Input Multiple Output

RANS Reynolds-Averaged Navier-Stokes

RSM Reynolds Stress Model

SISO Single Input Single Output

SOLSH190 Solid Shell Elements

UAV Unmanned Aerial Vehicle

$SST\ k-\omega$ Shear-Stress Transport k-omega

Chapter 1

Introduction

1.1 Background

Flutter is defined as an unstable self-excited oscillation of a structure, at its natural frequency. Flutter arises from the existence of aeroelastic instability. This instability stems from the aerodynamic forces feeding energy into the structural system, by virtue of its position or configuration, as rapidly as it is dissipated by the structure's damping [11].

The motion of a structural system can be considered as the superposition of its normal modes of vibration. The vibration of a structure would naturally be dissipated if not for the aerodynamic forces acting upon it. Depending on the speed of the air, the aerodynamic forces could decrease, maintain or increase the amplitude of the vibration. It must be noted that the aerodynamic forces, which maintain the oscillations, exist purely because of the vibration of the system. In other words, if the system were not disturbed, it would be possible to exceed the critical speed, of the wing, without inducing any vibration. Flutter can therefore be classified as a self-exited, aeroelastic vibration [12].

This phenomenon plays a significant role in the design, development and commissioning of vehicles in the aerospace industry. Flutter can be detrimental to the performance of an aircraft's structural components, with regards to its structural integrity and endurance. It was first identified during World War I on the Handley Page bomber where the flutter mechanism consisted of the fuselage torsional mode with anti-symmetric elevator rotation [13].

In the modern era, aircraft design is focused on maximising the performance by improving several facets of the aircraft. An example of such improvements would involve structural mass reduction of the wing by using lighter and more flexible material [14]. Another potential means of developing more efficient aircraft may involve the use of high-aspect-ratio wings. High-aspect-ratio wings benefit from superior lift-drag ratios.

However, these wings tend to be less rigid which, coupled with the fact that mass reduction may result in reduced stiffness, increases their susceptibility to aeroelastic instability [15] [16].

This aeroelastic instability can be resolved by increasing the aerodynamic damping of the system. The wing's control surfaces provide a means of suppressing vibration, by increasing the aerodynamic damping of the wing. Marretta and Marino (2007) demonstrated the use of control surfaces to suppress flutter, using a mathematical model to perform the aeroelastic analysis.

The aim of this project was to design and evaluate a flutter-suppression control system for a high-aspect-ratio wing. The flutter-suppression control system was required to suppress vibration of a wing. Suppression of vibration would aid in the dissipation of energy being fed into the system by the fluid, thereby increasing the aerodynamic damping of the system. Modelling aeroelastic phenomena requires a means of accounting for both the structural and fluid environments. This multi-physics phenomenon, known as Fluid-Structure Interaction (FSI), is to be modelled by means of numerical analysis using the commercially available software, ANSYS.

1.2 Objectives

The following details the objectives of this thesis:

- Establish a structural and fluid environment, in ANSYS, which constitutes a numerical FSI model
- A high-aspect-ratio wing is to be used in the FSI model
- Construct an active control system
- Derive a state-space model of the FSI and implement the model in the control system
- Embed the control system within the FSI model
- Use existing control surfaces to suppress vibration

1.3 Thesis outline

The literature study, presented in Chapter 2, lays the foundation for key principles used in the project. A classical flutter analysis is performed in Chapter 3 where strip theory and a beam model was used in the analysis. Chapter 4 details the structural environment. This chapter documents the computer aided design (CAD) models of the structure, the manner in which discretization was performed, mesh details, a modal analysis, the base excitation used and where the FSI interface was defined on the FE model. Chapter 5 elaborates on the fluid environment. Similar to chapter 4, it documents the CAD models of the fluid domain, the discretization performed, mesh details, boundary conditions, dynamic mesh settings and where the FSI interface was defined on the CFD model. Chapter 6 then documents how the controller was constructed. This includes derivation of the state-space model, the manner in which the controller was embedded within the FSI model, the logic of the controller and the subsequent modification to the original FSI process. Chapter 7 documents the results of the initial FSI simulations and the results of the refined FSI simulations. Lastly, the conclusions drawn from the project and the accompanying recommendations are presented in Chapter 8.

Chapter 2

Literature study

2.1 Wing theory

A moving body submersed in fluid is subject to forces. If the force opposite to the direction of motion is small or negligible compared to the force normal to the direction of motion, the body is considered to be a wing. The cross-sectional area of the wing is referred to as the wing profile whereas the shape is known as the aerofoil. Figure 2.1 depicts the characteristic geometrical quantities of an aerofoil [1].

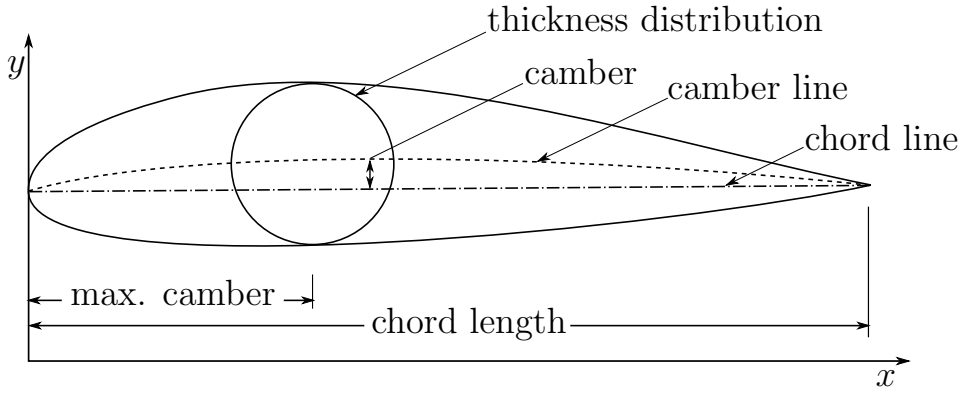

Figure 2.1: Aerofoil characteristic geometrical quantities [1]

The coordinates of the profile are plotted against an appropriate x- and y-axis. The profile may be regarded as the superposition of a symmetric thickness distribution, which varies along the camber line. The camber line influences the shape and camber of the aerofoil. The camber is defined as the vertical distance between the camber line and chord line, at corresponding positions along the x-axis. It reaches a maximum value, the location of which is expressed as a percentage of the chord length. These geometrical quantities ultimately influence the aerodynamic characteristics of the aerofoil.

A wing displaces the fluid it's submersed in. In the case of free-flight of an aircraft, displacement of air results in an increase in streamline density lateral to the surface of the wing, in order to satisfy continuity [2]. Figure 2.2 depicts how the free-stream velocity (v_∞) generates the streamline pattern as the streamlines curve around the wing.

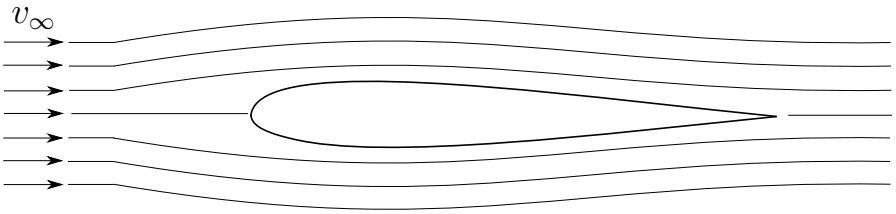

Figure 2.2: Streamline pattern over a wing [2]

The velocity of the air approaches its maximum value at the wing's maximum thickness where the static pressure is at its minimum. The curvature of the streamlines results in an increase in static pressure in a direction normal to the streamlines expressed by:

$$dp = \frac{\rho V}{R} dy \tag{2.1}$$

These elementary centrifugal forces compensate for the difference between the low static pressure, at the surface of the wing, and the higher static pressure in the undisturbed free-stream [2].

The wing's planform geometry has a significant influence on an aircraft's performance. High-aspect-ratio wings are long and narrow whereas low-aspect-ratio wings are short and stubby. Figure 2.3 illustrates the transition of an aircraft's wings as the aspect ratio varies from a low, to moderate and finally a high aspect ratio [15].

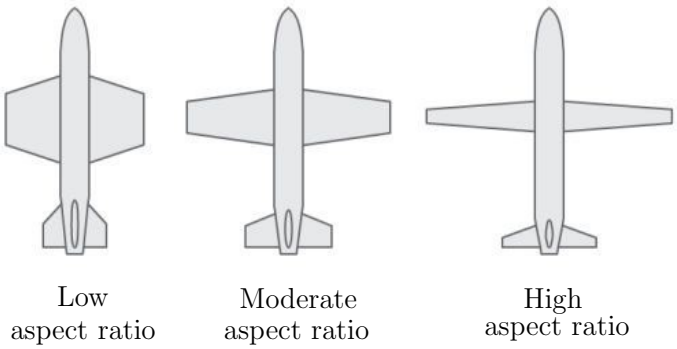

Figure 2.3: Wing aspect ratio [3]

Geometry of high-aspect-ratio aerofoils implies that the wing has aerofoil geometrical quantities which results in the center of aerodynamic pressure generally being located more towards the back of the wing [15].

Quantifying the aspect ratio of a wing is expressed by equation 2.2. Figure 2.4 depicts the top view of a wing planform, illustrating the wing's span and chord.

$$Aspect\ ratio = \frac{Span}{Chord} \tag{2.2}$$

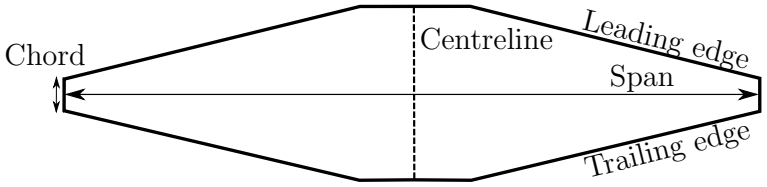

Figure 2.4: Top view of a wing planform

High-aspect-ratio wings are desirable since they benefit from a superior lift-drag ratio and are lightweight. An undesirable feature of these wings include a lack of manoeuvrability. As a result, these wings are not found on aerospace vehicles such as fighter aircraft but are used in applications such as high-altitude long-endurance (HALE) aircrafts and unmanned aerial vehicles (UAV) [15].

High-aspect-ratio wings tend to undergo larger deformation, due to their flexibility. The large deformation and accompanying changes in aerodynamic loads may prove significant. In addition, the structure endures fatigue which compromises its service life or may cause immediate failure if the vibration amplitude is too large [17].

2.2 Flight control

All aircraft adhere to the same basic principle of flight, which entail altering the aircraft's yaw, pitch and roll. The flight control system allows the pilot to exercise control over the aircraft via flight control surfaces. The flight control surfaces are grouped into 2 categories, namely primary and secondary controls [4]. Figure 2.5 illustrates the location of each component of the flight control system, where the corresponding numbering of the components are shown in Table 2.1.

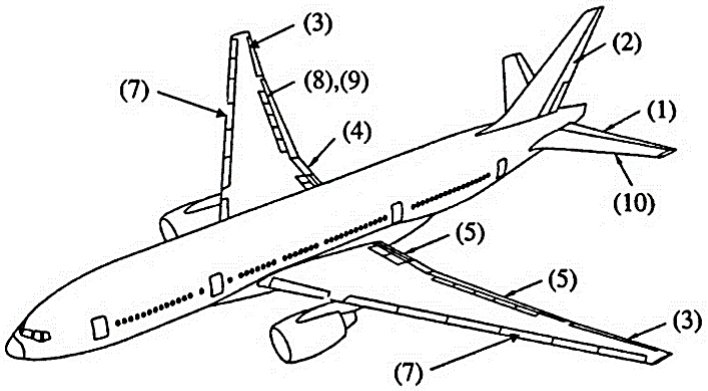

Figure 2.5: Aircraft flight control [4]

Table 2.1: Flight control surfaces

Number	Component	Category
1	Elevators	Primary
2	Rudder	Primary
3	Ailerons	Primary
4	Flaperons	
5	Flaps	Secondary
7	Slats	Secondary
8	Spoilers	Secondary
9	Airbrakes	Secondary
10	Stabilizer Trim	Secondary

2.2.1 Primary controls

The primary control surfaces consist of the elevators, rudders, ailerons and canards. These surfaces control the pitch, yaw and roll of the aircraft. The pitch is controlled via elevators, located at the trailing edge of the tailplane. Roll-control is exercised by the ailerons located at the outboard of the wings. Yaw-control is provided by rudders located on the trailing edge of the vertical stabilizer [4].

2.2.2 Secondary controls

Secondary control surfaces consist of the flaps, slats, spoilers and speed brakes. These control surfaces offer the pilot the ability to alter the lift of the aircraft, when the need arises. Flaps are located inboard on the wings, along the trailing edge.

Flaps are the simplest ways of increasing the maximum lift characteristic of the wing [1]. The flaps extend rearwards and downwards thereby increasing lift due to an increase in wing camber and chord. Slats are situated at the leading edge of the wing. They are able to extend forward and downwards which, similarly to the flaps, increase wing chord and camber to increase the wing's lift characteristic. Speed brakes are deployed when all of the wing's spoilers are extended. These control surfaces increase drag to allow adjustment of the airspeed [4]. Figure 2.6 depicts the control surfaces found on a wing. The active controller was required to suppress vibration using existing control surfaces therefore, table 2.2 lists the possible control surfaces (in accordance with figure 2.6) that could have been used for the project.

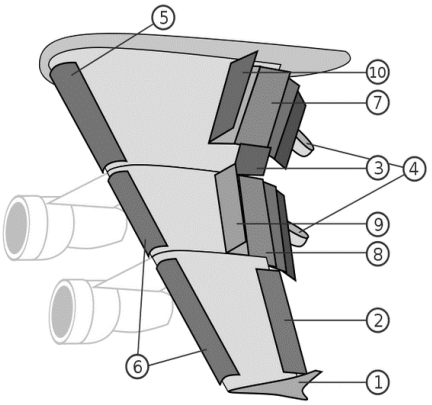

Figure 2.6: Wing control surfaces [5]

Table 2.2: Wing control surfaces

Number	Component
1	Winglet
2	Low speed aileron
3	High speed aileron
4	Flap track fairing
5	Leading edge flaps
6	Leading edge slats
7	Inboard flaps
8	Outboard flaps
9	Spoilers
10	Spoiler air brakes

2.3 Aeroelastic instability

Aeroelasticity is the discipline which combines aerodynamics, elasticity and dynamics. Aeroelasticity can be described as the reciprocal interaction (static or dynamic) between the aerodynamic forces and the deformations induced by these forces in the structure, its control mechanisms or the aircraft's propulsion systems [18].

2.3.1 Classical flutter

Lifting surfaces, found on an aircraft, can be subject to several aerodynamic self-excited oscillations. Classical flutter refers to an occurrence in which the flutter mechanism may, though not necessarily, involve the coupling of several degrees-of-freedom (DOF) of the structure [12]. In the case of aircraft wings, this may include a coupling of the bending and torsional modes. This instability occurs when the fluid flow is attached to the wing. Analyses of non-classical flutter prove to be more difficult as it may involve flow separation, stalling, shock and time-lag effects between the flow field and motion. Only a single DOF of the structure may be involved in this flutter mechanism.

An aeroelastic problem, such as flutter, can be decomposed into its mechanical and aerodynamic constituents. The former requires the motion of the aircraft's structure to be taken into account as a continuous vibrating system, subject to the external air forces and internal damping of the structure. The latter requires a means of determining the nature of the aerodynamic forces acting on the structure. These aerodynamic forces are independent of the static forces which tend to maintain the system in an equilibrium system. The oscillatory aerodynamic forces, acting on the system, tend to maintain the structures oscillations about the equilibrium position [12].

2.3.2 Simple 2-DOF system

Figure 2.7 depicts a structural system where a rotational spring and plunge spring constitutes a 2-DOF system. The plunge spring represents the bending stiffness of the wing whereas the rotational spring represents the torsional stiffness. The shape of the aerofoil determines where the aerodynamic center is located. The aerofoil's center of gravity is dependent on the mass distribution of the cross-section [14].

Aerodynamic forces excite this spring/mass system. The critical speed, of the wing, is encountered when the energy input would equal that of the energy being dissipated by the structural system.

Once the critical speed is exceeded, the 2-DOF system could excite one of its two natural modes or a coupled mode which is a coalescence of the two natural modes [14].

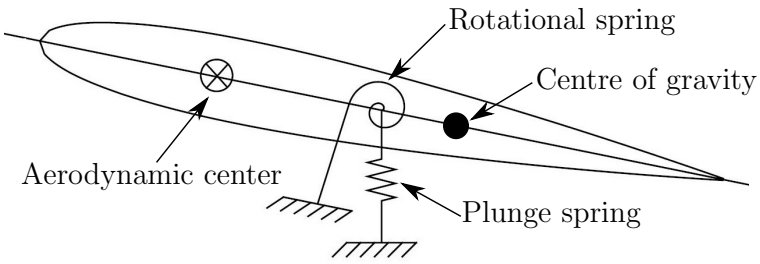

Figure 2.7: 2-DOF aerofoil system

The system above does not account for control surfaces that may exist on an actual aircraft. Aeroelastic instability may arise from the presence of control surfaces, as their DOF will have their own natural modes. An example includes the Handley Page bomber, mentioned in section 1, where the rotational DOF of the elevator contributed to the particular flutter mechanism.

2.4 Structural modelling

The structure of the wing can be represented by a FE model. The FE model consists of a system of equations and is derived by discretizing the structure into elements. The governing equation for structural dynamics is expressed by equation 2.3. This equation states that work done on a single element (with a volume V, and surface area S) be equal to work absorbed by the inertial, dissipative and internal forces [19].

$$\int (\delta \mathbf{s})^T \ \mathbf{f} \ dV + \int (\delta \mathbf{s})^T \ \Phi \ dS + \sum_{i=1}^{n} (\delta \mathbf{s})_i^T \ \mathbf{p}_i = \int \left((\delta \mathbf{s})^T \ \rho_S \ \ddot{\mathbf{s}} + (\delta \mathbf{s})^T c \ \dot{\mathbf{s}} + (\delta \boldsymbol{\varepsilon})^T \boldsymbol{\sigma} \right) \ dV \quad (2.3)$$

where $\mathbf{f}$ and Φ represent the body force vector and surface traction vector, $\mathbf{p}_i$ and $\delta \mathbf{s}$ the concentrated load vector (located at the nodes) and their corresponding virtual displacements at n points. $\boldsymbol{\varepsilon}$ serves as the strain vector, ρ_S the structural mass density, c the damping parameter (analogous to viscosity) and $\boldsymbol{\sigma}$ the stress vector.

Equation 2.4 expresses the relationships between virtual displacement and the shape function ($\mathbf{N}$) and the relationship between strain and the strain-displacement ($\mathbf{B}$). Equation 2.5 is formed after substituting these relationships in equation 2.3.

$$\mathbf{s} = \mathbf{N}\ \mathbf{d} \qquad \dot{\mathbf{s}} = \mathbf{N}\ \dot{\mathbf{d}} \qquad \ddot{\mathbf{s}} = \mathbf{N}\ \ddot{\mathbf{d}} \qquad \varepsilon = \mathbf{B}\ \mathbf{d} \tag{2.4}$$

$$\delta\mathbf{d}\left[\int \rho_S\ \mathbf{N}^T\mathbf{N}\ dV\ \ddot{\mathbf{d}} + \int c\ \mathbf{N}^T\mathbf{N}\ dV\ \dot{\mathbf{d}} + \int \mathbf{B}^T\ \sigma\ dV - \int \mathbf{N}^T\ \mathbf{F}\ dV - \int \mathbf{N}^T\ \mathbf{\Phi}\ dS - \sum_{i=1}^{n}\ \mathbf{p}_i\right] = 0 \tag{2.5}$$

The element mass and damping matrices, following discretization are:

$$\mathbf{M_e} = \int \rho_S\ \mathbf{N}^T\mathbf{N}\ dV \qquad \mathbf{C_e} = \int c\ \mathbf{N}^T\mathbf{N}\ dV \tag{2.6}$$

Elemental internal and external forces and moments are accounted for by equations 2.7 and 2.8 respectively.

$$(\mathbf{r_{int}})_\mathbf{e}\ = \mathbf{K_e}\ \mathbf{d_e} = \int \mathbf{B}^T\ \sigma\ dV \tag{2.7}$$

$$(\mathbf{r_{ext}})_\mathbf{e} = \int \mathbf{N}^T\ \mathbf{F}\ dV + \int \mathbf{N}^T\ \mathbf{\Phi}\ dS + \sum_{i=1}^{n}\ \mathbf{p}_i \tag{2.8}$$

Substituting equations 2.6, 2.7 and 2.8 into 2.5 yields:

$$\mathbf{M_e}\ddot{\mathbf{d}}_\mathbf{e} + \mathbf{C_e}\dot{\mathbf{d}}_\mathbf{e} + \mathbf{K_e}\mathbf{d}_e = (\mathbf{r_{ext}})_\mathbf{e} \tag{2.9}$$

for a multi-element structure, equation 2.9 assumes the global form of:

$$\mathbf{M}\ddot{\mathbf{d}} + \mathbf{C}\dot{\mathbf{d}} + \mathbf{K}\mathbf{d} = \mathbf{r_{ext}} \tag{2.10}$$

Equation 2.10 represents the generalized equation of motion. This system of equations accounts for the dynamics of the structural environment without the influence of other physical environments [20]. The damping matrix is calculated using the Rayleigh viscous damping model, shown in equation 2.11. This damping model is the standard model used by the ANSYS Mechanical APDL solver. This model defines the global damping matrix as a linear combination of the global mass and stiffness matrix.

$$\mathbf{C} = \alpha\mathbf{M} + \beta\mathbf{K} \tag{2.11}$$

where α is the mass-proportional damping parameter and β, the stiffness-proportional damping parameter. These values can be determined from equation 2.12 where ξ represents the damping ratio and f the frequency of the natural mode [19].

$$\xi = \frac{1}{2}\left(\frac{\alpha}{2\pi f} + \beta\ 2\pi f\right) \tag{2.12}$$

If damping is present, the damped frequency is expressed with equation 2.13:

$$f_d = f\sqrt{1-\xi^2} \tag{2.13}$$

2.5 Fluid modelling

CFD entails the analysis of a fluid system that may involve fluid flow, heat transfer and associated chemical reactions via computer-based simulation [6]. The behaviour of fluid under motion is described by the continuity and momentum equations in 3 dimensions. In the derivation of these equations for unsteady and incompressible flow (specific for this project), body forces such as gravity are neglected [21].

2.5.1 Governing equations

The conservation of mass states that the rate at which mass increases, in a fluid element, must equal the net rate at which mass flows into the fluid element. For a 3-dimensional case, this can be expressed as:

$$\frac{\partial \rho_F}{\partial_t} + \frac{\partial(\rho_F v_x)}{\partial_x} + \frac{\partial(\rho_F v_y)}{\partial_y} + \frac{\partial(\rho_F v_z)}{\partial_z} = 0 \tag{2.14}$$

Equation 2.14 is known as the continuity equation for an unsteady and compressible flow. The equation can further be simplified, for the purpose of this project, by applying incompressible conditions and yielding:

$$\frac{\partial v_x}{\partial_x} + \frac{\partial v_y}{\partial_y} + \frac{\partial v_z}{\partial_z} = 0 \tag{2.15}$$

The momentum equations, in their respective dimensions, are as follows:

x-dimension:

$$\rho_F\left(\frac{\partial v_x}{\partial t}+v_x\frac{\partial v_x}{\partial x}+v_y\frac{\partial v_x}{\partial y}+v_z\frac{\partial v_x}{\partial z}\right)=-\frac{\partial p}{\partial_x}+\mu\left(\frac{\partial^2 v_x}{\partial x^2}+\frac{\partial^2 v_x}{\partial y^2}+\frac{\partial^2 v_x}{\partial z^2}\right) \quad (2.16a)$$

y-dimension:

$$\rho_F\left(\frac{\partial v_y}{\partial t}+v_x\frac{\partial v_y}{\partial x}+v_y\frac{\partial v_y}{\partial y}+v_z\frac{\partial v_y}{\partial z}\right)=-\frac{\partial p}{\partial_y}+\mu\left(\frac{\partial^2 v_y}{\partial x^2}+\frac{\partial^2 v_y}{\partial y^2}+\frac{\partial^2 v_y}{\partial z^2}\right) \quad (2.16b)$$

z-dimension:

$$\rho_F\left(\frac{\partial v_z}{\partial t}+v_x\frac{\partial v_z}{\partial x}+v_y\frac{\partial v_z}{\partial y}+v_z\frac{\partial v_z}{\partial z}\right)=-\frac{\partial p}{\partial_z}+\mu\left(\frac{\partial^2 v_z}{\partial x^2}+\frac{\partial^2 v_z}{\partial y^2}+\frac{\partial^2 v_z}{\partial z^2}\right) \quad (2.16c)$$

Equations 2.15 and 2.16a-2.16c form the fundamental equations of fluid flow. Common parameters exist among the equations which calls for introducing a variable, ϕ. The transport equation is therefore introduced and expressed by equation 2.17, where Γ is the diffusion coefficient.

$$\rho_F\left(\frac{\partial \phi}{\partial t}+v_x\frac{\partial \phi}{\partial x}+v_y\frac{\partial \phi}{\partial y}+v_z\frac{\partial \phi}{\partial z}\right)=\mathsf{div}(\Gamma\ \mathsf{grad}\ \phi) \quad (2.17)$$

Determining the flow regime of a fluid in motion requires the Reynolds number (Re) to be determined. This dimensionless parameter represents the ratio of inertial forces to viscous forces. The Reynolds number was determined using equation 2.18 where h_d refers to the characteristic length and v the fluid velocity. Transition of laminar to transitional flow occurs at a critical Re number which varies for different bodies and freestream conditions.

$$Re=\frac{\rho_F\ v\ h_d}{\mu} \quad (2.18)$$

2.5.2 Turbulence modelling

The final state of flow behaviour, turbulent flow, is defined as a chaotic and random state of motion. Unlike laminar flow, which can be analytically solved by the equations stated in section 2.5.1, turbulent flow requires a more intricate manner of solving the fluid domain [6].

The random nature of turbulence is illustrated by figure 2.8. The magnitude of the fluid velocity is the sum of its mean component ($\bar{v}$) and its corresponding fluctuating component ($v'(t)$). The process of characterising the velocity into a mean and fluctuating component is known as Reynolds decomposition, shown by equation 2.19.

$$v = \bar{v} + v'(t) \tag{2.19}$$

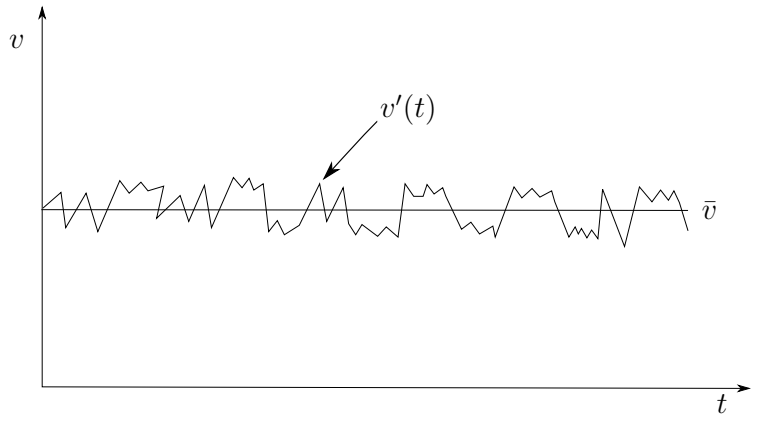

Figure 2.8: Random nature of turbulence [6]

In order to account for the fluctuating and mean velocity components, the continuity and momentum equations are modified to incorporate Reynolds decomposition in order to compensate for the random nature that stems from the turbulent flow.

The continuity equation that incorporates the fluctuating and mean velocity components is obtained by substituting equation 2.19 into equation 2.15. Separating with respect to the velocity components and then taking a time average over the entire equation yields:

$$\frac{\partial \bar{v_x}}{\partial x} + \frac{\partial \bar{v_y}}{\partial y} + \frac{\partial \bar{v_z}}{\partial z} = 0 \tag{2.20}$$

Similarly, the modified momentum equations in their respective dimensions are shown below, once Reynolds decomposition is implemented. Note, the terms without the mean or fluctuating superscripts represent the average velocity terms.

x-dimension:

$$\rho_F\Big(\frac{\partial v_x}{\partial t} + v_x\frac{\partial v_x}{\partial x} + v_y\frac{\partial v_x}{\partial y} + v_z\frac{\partial v_x}{\partial z}\Big) = -\frac{\partial p}{\partial_x} + \mu\Big(\frac{\partial^2 v_x}{\partial x^2} + \frac{\partial^2 v_x}{\partial y^2} + \frac{\partial^2 v_x}{\partial z^2}\Big) \left[\frac{\partial(-\rho_F\overline{v_x'^2})}{dx} + \frac{\partial(-\rho_F\overline{v_x'v_y'})}{dy} + \frac{\partial(-\rho_F\overline{v_x'v_z'})}{dz}\right] \tag{2.21a}$$

y-dimension:

$$\rho_F\Big(\frac{\partial v_y}{\partial t}+v_x\frac{\partial v_y}{\partial x}+v_y\frac{\partial v_y}{\partial y}+v_z\frac{\partial v_y}{\partial z}\Big)=-\frac{\partial p}{\partial_y}+\mu\Big(\frac{\partial^2 v_y}{\partial x^2}+\frac{\partial^2 v_y}{\partial y^2}+\frac{\partial^2 v_y}{\partial z^2}\Big)$$
$$\Big[\frac{\partial(-\rho_F\overline{v'_x v'_y})}{dx}+\frac{\partial(-\rho_F\overline{v'^2_y})}{dy}+\frac{\partial(-\rho_F\overline{v'_y v'_z})}{dz}\Big] \quad (2.21b)$$

z-dimension:

$$\rho_F\Big(\frac{\partial v_z}{\partial t}+v_x\frac{\partial v_z}{\partial x}+v_y\frac{\partial v_z}{\partial y}+v_z\frac{\partial v_z}{\partial z}\Big)=-\frac{\partial p}{\partial_z}+\mu\Big(\frac{\partial^2 v_z}{\partial x^2}+\frac{\partial^2 v_z}{\partial y^2}+\frac{\partial^2 v_z}{\partial z^2}\Big)$$
$$\Big[\frac{\partial(-\rho_F\overline{v'_x v'_z})}{dx}+\frac{\partial(-\rho_F\overline{v'_y v'_z})}{dy}+\frac{\partial(-\rho_F\overline{v'^2_z})}{dz}\Big] \quad (2.21c)$$

Equations 2.20 and 2.21a-2.21c are classified as the Reynolds-Averaged Navier-Stokes (RANS) equations.

The implementation of Reynolds decomposition generates additional terms in the time-averaged equations as a result of the fluctuating components. A 3-dimensional case introduces additional viscous terms, consisting of 3 normal stresses ($\overline{v'^2_x}, \overline{v'^2_y}, \overline{v'^2_z}$) and 3 shear stresses ($\overline{v'_x v'_y}, \overline{v'_x v'_z}, \overline{v'_y v'_z}$) and take the form of a tensor called the Reynolds stress tensor, shown by the matrix below. The normal stresses constitutes the respective variances of the x-,y- and z-velocity fluctuations while shear stresses are associated with correlations between different velocity components. Which implies that 6 additional terms are to be solved in a 3-dimensional case [6].

$$\tau=-\rho_F\begin{bmatrix}\tau_{xx}&\tau_{xy}&\tau_{xz}\\ \tau_{xy}&\tau_{yy}&\tau_{yz}\\ \tau_{xz}&\tau_{yz}&\tau_{zz}\end{bmatrix}=-\rho_F\begin{bmatrix}\overline{v'^2_x}&\overline{v'_x v'_y}&\overline{v'_x v'_z}\\ \overline{v'_x v'_y}&\overline{v'^2_y}&\overline{v'_y v'_z}\\ \overline{v'_x v'_z}&\overline{v'_y v'_z}&\overline{v'^2_z}\end{bmatrix}$$

The Reynolds stress model (RSM) is a turbulence model which calls for a transport equation to be solved for each term in the Reynolds stress tensor. In addition to this, a scale-determining equation is also constructed which results in 7 additional transport equations to be solved for a 3-dimensional case. As a result, the RANS equations can be solved. However, such a turbulence model is quite computationally intensive [22].

The Boussinesq approximation is introduced as a means of estimating the Reynolds stress terms. This notion states that the turbulent stresses are proportional to the rate of deformation. Using Einstein's notation, equation 2.22 expresses this approximation.

$$\tau_{ij}=-\rho_F\,\overline{v'_i v'_j}=\mu_t\Big(\frac{\partial v_i}{\partial x_j}+\frac{\partial v_j}{\partial x_i}\Big)-\frac{2}{3}\rho_F k\delta_{ij} \quad (2.22)$$

Where k is the turbulent kinetic energy and δ, the Kronecker delta. Equation 2.22 allows for the RANS equations to be solved and provides the advantage of relatively low computational cost (as opposed to the RSM) associated with the computation of the turbulent viscosity, μ_t. However, one of the assumptions that the Boussinesq approximation relies on is that μ_t is a isotropic scalar quantity, which does not hold true in certain instances [6].

A RANS based turbulence model is widely accepted in industry. The Mixing length, Spalart-Allmaras, $k-\epsilon$ and the $k-\omega$ models are all based on the RANS equations. Although some prove better than others, no turbulence model is universally accepted. Table 2.3 lists the aforementioned turbulence models with their respective number of transport equations [22].

Table 2.3: Transport equations amongst turbulence models

Model	Number of transport eq.
Mixing length	0
Spalart-Allmaras	1
$k-\epsilon$	2
$k-\omega$	2

The mixing-length turbulence model is completely incapable of describing fluid flow with separation and recirculation despite being easy to implement and less computational intensive than its counterparts. The Spalart-Allmaras turbulence model requires less computational effort than the $k-\epsilon$ and the $k-\omega$ turbulence models as it relies on using only one transport equation. This turbulence model was specifically designed for aerospace applications and has been gaining popularity in turbo machinery applications. However, this model is relatively new and its approach to using a single transport equation has been criticised regarding its ability to resolve changes in length scale. This might be an issue when flow changes, abruptly, from a wall-bounded to a free shear flow [22].

The standard $k-\epsilon$ model became the workhorse of engineering flow calculations in practice as a result of its robustness, economy and reasonable accuracy. This semi-empirical model is based on transport equations for the turbulent kinetic energy and the dissipation rate (ϵ). The $k-\epsilon$ model assumes that flow is fully turbulent and that the effects of viscous forces are negligible. However, as time has progressed, the strengths and weaknesses associated with the model have become known and subsequent improvements have lead to the formulation of improved versions of the model, such as the realizable $k-\epsilon$ model and the RNG $k-\epsilon$ model.

Similarly, the standard $k-\omega$ model is based on empirical transports equations for the turbulent kinetic energy and the specific dissipation rate (ω).

This model is based on the Wilcox $k-\epsilon$ model which includes modifications for low-Reynolds-number effects, compressibility and shear flow spreading [22].

2.6 FSI

The quantitative treatment of any problem begins with the formulation of the mathematical models. In the study of aeroelasticity, this entails the behaviour of a deformable body under the simultaneous effect of the aerodynamic heating and pressure acting upon the structure [18]. However, for the scope of this project, the effects of aerodynamic heating are neglected. Equation 2.10 is modified to form equation 2.23, where the additional vector ($\mathbf{r_F}$) accounts for the generalised force vector that stems from the aerodynamic pressure [20].

$$\mathbf{M\ddot{d}} + \mathbf{C\dot{d}} + \mathbf{Kd} = \mathbf{r_{ext}} + \mathbf{r_F} \tag{2.23}$$

When the need to combine multiple physical environments arises, some form of coupling between the environments is required. Such is the case for FSI where the fluid and structural environments are not analytically combined but influence each other [23]. This intricate coupling of the two different environments allows the outputs of each environment to be the inputs for its respective counterpart. The structure and fluid environments are governed by separate, independent systems of equations. These systems of equations interact at the interface of the FSI model. Displacement and force transfers are typical for FSI simulations. Forces from the CFD environment are transferred to the structural environment whereas displacements are transferred from the structural environment to the fluid environment [24].

Equations 2.25a and 2.25b form the generic coupled system with two environments, which is a decomposition of equation 2.24. The splitting of environments (partitioning), stems from different physics, separate spatial domains or the need for numerical implementation [25]. The monolithic and staggered approaches are two methods in which a coupling can be formed in a multi-physics problem [21].

$$\mathbf{X} = (\mathbf{X}_S, \mathbf{X}_F)^T \tag{2.24}$$

$$\dot{\mathbf{X}}_S = f_S(\mathbf{X}_S, \mathbf{X}_F) \tag{2.25a}$$

$$\dot{\mathbf{X}}_F = f_F(\mathbf{X}_S, \mathbf{X}_F) \tag{2.25b}$$

2.6.1 Monolithic approach

The monolithic approach relies on combining two or more systems of equations that are solved simultaneously. In the case of equations 2.25a and 2.25b, the two systems of equations are combined into one large system of equations. This large system of equations is then solved with a single solver. As a result, this approach is ideally suited when the characteristic behaviour of the coupled environments share a similar nature. This approach also proves to be computationally intensive as it requires a large system of equation to be solved [23].

2.6.2 Staggered approach

The staggered approach solves each environment with independent solvers. Equations 2.25a and 2.25b would therefore be solved individually, within their respective environments, at every time-step. The output of each environment is then shared, sequentially, as each environment is solved with synchronization points to exchange information at the interface. This offers the ability to optimise the solvers to suit their respective environments, unlike the monolithic approach [21] [26].

An important concept in a multi-physics problem is strong coupling. This coupling requires that solutions of both environments achieve convergence at each time-step. The monolithic approach is intrinsically strongly coupled, as a result of forming one large system of equations. The staggered approach lags between solutions, stemming from the fact that each environment is sequentially solved before the next. Advancing a coupled system once per time-step (loosely-coupled staggered approach) will not guarantee convergence. A strong coupling (strongly-coupled staggered approach) requires several computations of each environment per time-step. These sub-iterations are referred to as stagger-iterations in this project. The additional computations per time-step leads to an increase in computational effort but is a necessity to increase stability of the coupled algorithm [25]. Equations 2.26a and 2.26b describe the staggered coupled algorithm. Parameters N and j denote the time-step and stagger-iteration respectively. A strongly-coupled staggered algorithm can be achieved if sufficient stagger-iterations are performed and equation 2.27 is resolved. It must be noted that if zero stagger-iterations are performed ($j = 0$) then the equations revert to a loosely-coupled staggered approach.

$$\mathbf{X}_S^{N,j} = f_S(\mathbf{X}_S^{N,j}, \mathbf{X}_S^{N-1}, \mathbf{X}_F^{N,j-1}) \tag{2.26a}$$

$$\mathbf{X}_F^{N,j} = f_F(\mathbf{X}_F^{N,j}, \mathbf{X}_F^{N-1}, \mathbf{X}_S^{N,j}) \tag{2.26b}$$

$$(\mathbf{X}_S^{N,j}, \mathbf{X}_F^{N,j})^T = (\mathbf{X}_S^{N,j-1}, \mathbf{X}_F^{N,j-1})^T = (\mathbf{X}_S^{N}, \mathbf{X}_F^{N})^T \tag{2.27}$$

The staggered approach was selected to perform the FSI analysis since ANSYS provides ANSYS Mechanical APDL and ANSYS FLUENT as the solvers for the structural and fluid environments respectively. A staggered coupled system could therefore be established using the ANSYS Multi-field solver (ANSYS MFX) [27]. It was assumed that a strong coupling would be achieved with enough stagger-iterations performed per time-step. Figure 2.9 illustrates the FSI process, using staggered coupling. Both FE and CFD models are initialised before the first time-step is executed. Forces are transferred to the structural environment before solving the FE model. The resultant displacements are then transferred to the fluid environment. If no remeshing of the CFD model is required, the CFD model is solved before reaching the end of the time-step, provided the maximum stagger-iterations have been performed or convergence of both environments has been achieved.

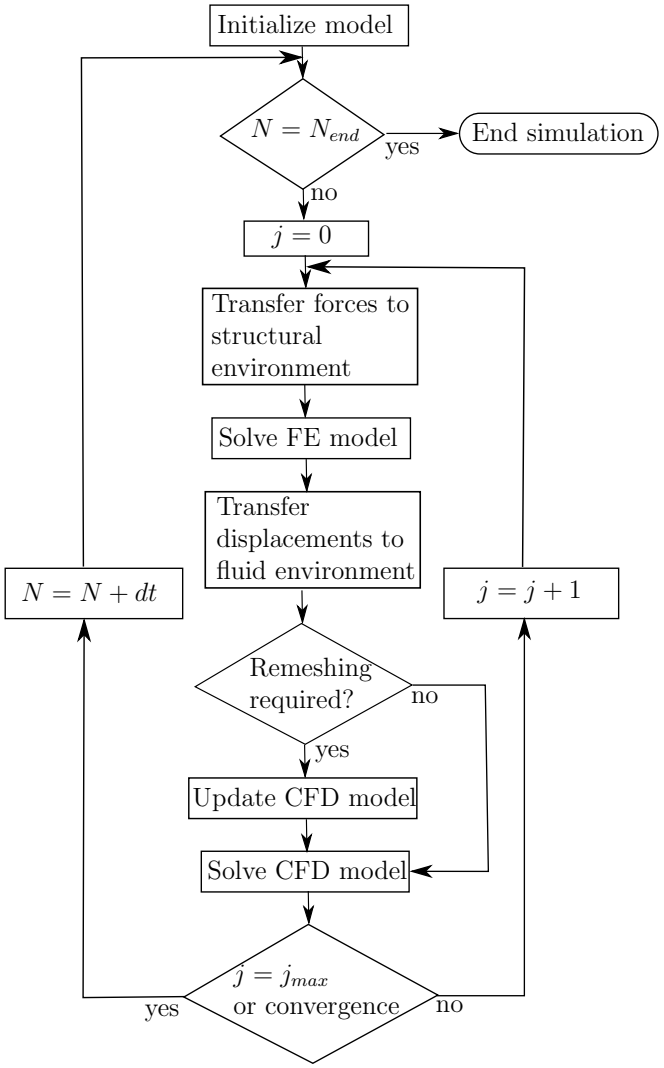

Figure 2.9: Staggered FSI coupling flowchart [7]

2.7 Control system

Control is undertaken to obtain a desired behaviour of a system. Control theory may be applied to a system to force the system to follow a desired input signal. This control can be applied as an open- or a closed-loop process. Open-loop control systems are typically less expensive and simpler, compared to their closed-loop counterparts, but are limited to systems which have well-established characteristics and are not prone to disturbances. As a result, closed-loop control systems are commonly used in practice. Typically, the primary goal is to produce an output that follows an input or reference as closely as possible [8]. Figure 2.10 depicts the block diagram of a closed-loop control system. Where the measured error is the difference between the measured output and the reference. This measured error is used by the controller to attenuate the system input to the system.

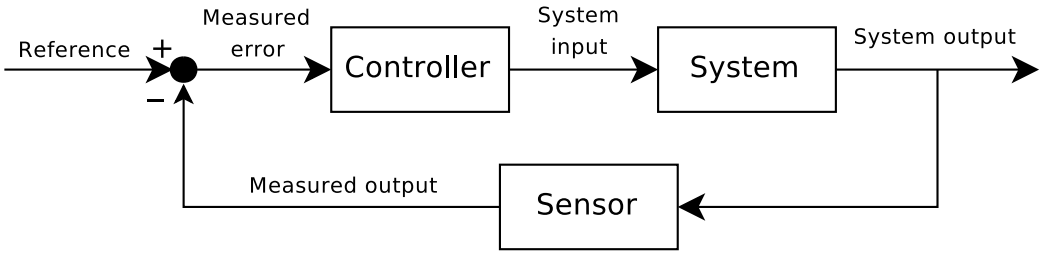

Figure 2.10: Closed-loop feed-back control system [8]

2.7.1 SISO and MIMO systems

A dynamic system interacts with its surroundings by means of input and output variables. Input variables are not directly dependent on what occurs in the system and originate outside the system. The output variables are chosen from a set of variables generated by the system. The objective(s) of the system analysis generally dictates the choice of the output variables. Figure 2.11 depicts a single input single output (SISO) system. The relationship between the input and output signals can be represented by an n^{th}-order differential equation, where $m \leq n$ (see equation 2.28) [8].

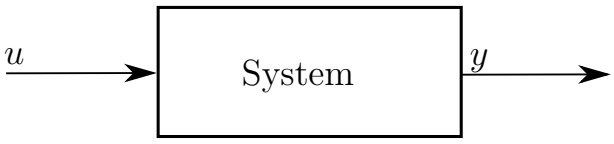

Figure 2.11: SISO system [8]

$$g\left(y, \frac{dy}{dt}, ..., \frac{d^n y}{dt^n}, u, \frac{du}{dt}, ..., \frac{d^m y}{dt^m}, t\right) = 0 \tag{2.28}$$

In the case of a stationary linear model, the function g is a sum of terms that are linear with respect to the arguments of g. A multiple input multiple output (MIMO) system is encountered when more than a single output variable is of interest. Figure 2.12 depicts a MIMO system with l inputs and p outputs Kulakowski *et al.*.

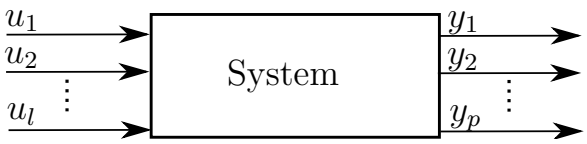

Figure 2.12: MIMO system [8]

Similar to the SISO system, a linear system can be represented by:

$$\begin{aligned}
g_1\left(y_1^{(n)}, ..., \dot{y}_1, y_1, u_1^{(m)}, ..., \dot{u}_1, u_1, u_2^{(m)}, ..., \dot{u}_2, u_2, ..., u_l^{(m)}, ..., \dot{u}_l, u_l, t\right) &= 0 \\
g_2\left(y_2^{(n)}, ..., \dot{y}_2, y_2, u_1^{(m)}, ..., \dot{u}_1, u_1, u_2^{(m)}, ..., \dot{u}_2, u_2, ..., u_l^{(m)}, ..., \dot{u}_l, u_l, t\right) &= 0 \\
\vdots \qquad\qquad\qquad\qquad & \qquad \vdots \\
g_p\left(y_p^{(n)}, ..., \dot{y}_p, y_p, u_1^{(m)}, ..., \dot{u}_1, u_1, u_2^{(m)}, ..., \dot{u}_2, u_2, ..., u_l^{(m)}, ..., \dot{u}_l, u_l, t\right) &= 0
\end{aligned} \tag{2.29}$$

where $m \leq n$

2.7.2 PID control design

The PID controller is expressed by equation 2.30. K_P, K_I and K_D represents the proportional, integral and derivative terms respectively. The difference between the output of the system and the reference is the measured error ($e(t)$) which is used by the controller to yield the input signal ($u(t)$). The K_P, K_I and K_D parameters are adjusted to generate desired closed-loop dynamics. These type of controllers are widely used in industry, are well established and are suited to SISO systems. However; PID controllers are of limited use when considering intricate designs such as MIMO systems [9].

$$u(t) = K_P e(t) + K_I \int e(t)dt + K_D \frac{d}{dt} e(t) \tag{2.30}$$

2.7.3 State-space control design

State-space control design is a technique in which the control engineer is able to design a dynamic compensation by working directly with the state-variable description of the system. One way of representing a physical system is by using linear state-space models, expressed by equations 2.31a - 2.31b. Where $\mathbf{x}$ represents the state vector, $\mathbf{F}$ the system matrix, $\mathbf{G}$ the input matrix, $\mathbf{u}$ the input-signal vector, $\mathbf{H}$ the output matrix, $\mathbf{E}$ the direct transmission term and $\mathbf{y}$ the output-signal [9].

$$\dot{\mathbf{x}} = \mathbf{F}\mathbf{x} + \mathbf{G}\mathbf{u} \tag{2.31a}$$

$$\mathbf{y} = \mathbf{H}\mathbf{x} + \mathbf{E}\mathbf{u} \tag{2.31b}$$

In most instances, the state variables of a system are not known or are not measurable by the control designer. A means of estimating the state variables is to construct the full-order model of the plant dynamics, shown in equation 2.32, where $\tilde{\mathbf{x}}$ is the state-estimate of the system. Figure 2.13 illustrates how a state-estimate and control law are used in compensating a system. The state-estimate is computed before the controller gain ($\mathbf{K}$) compensates the input-signal (u) to the system (using equation 2.33) [9].

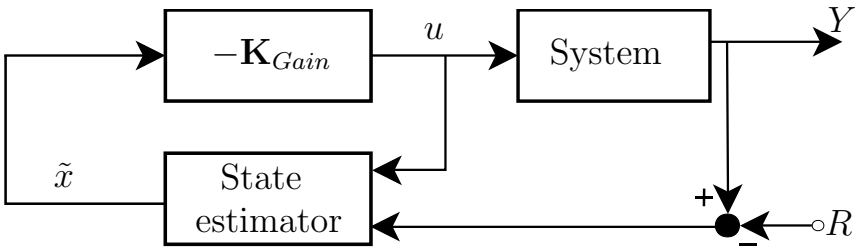

Figure 2.13: Control law with a state-estimator [9]

$$\dot{\tilde{\mathbf{x}}} = \mathbf{F}\tilde{\mathbf{x}} + \mathbf{G}\mathbf{u} \tag{2.32}$$

$$\mathbf{u} = \text{-}\mathbf{K}_{Gain}\tilde{\mathbf{x}} \tag{2.33}$$

Chapter 3

Classical flutter analysis

The following section describes the classical flutter analysis that was performed on the selected wing model. The mathematical formulation is established using a 2-DOF cantilever beam model. This idealised model neglects the presence of control surfaces. Strip theory assumes quasi-steady aerodynamics to establish the aerodynamic matrix before the critical flutter speed is determined by solving the eigenvalues.

Assuming w and θ to be the deviations from the equilibrium state, the equations of motion are defined as [28]:

$$\frac{\partial^2}{\partial x^2}\left(EI\frac{\partial^2 w}{\partial x^2}\right) + m\frac{\partial^2 w}{\partial t^2} + my_\theta\frac{\partial^2 \theta}{\partial t^2} + L = 0 \tag{3.1}$$

$$-\frac{\partial}{\partial x}\left(GJ\frac{\partial \theta}{\partial x}\right) + I_\theta\frac{\partial^2 \theta}{\partial t^2} + my_\theta\frac{\partial^2 w}{\partial t^2} + M = 0 \tag{3.2}$$

Where EI and GJ represent the bending and torsional rigidity of the wing and m and I_θ are the mass and mass moment of inertia (per unit length) about the elastic axis. The bending and torsional normal modes are expressed using Galerkin's method shown by [29]:

$$W = \sum_{j=1}^{n} a_j\phi_j \qquad\qquad \Theta = \sum_{j=n+1}^{n+m} a_j\phi_j$$

where ϕ_j are the modal functions. The j^{th} bending mode for the beam model is expressed by:

$$\phi_j = (cosh\ a_n x - cos\ a_n x) - \sigma_n(sinh\ a_n x - sin\ a_n x) \tag{3.3}$$

with boundary conditions:

$$\phi_j(x=0)=0 \qquad \phi_j'(x=0)=0 \qquad (j=1,2...n)$$

$$\sigma_n = \frac{(cosh\ a_nL - cos\ a_nL)}{(sinh\ a_nL - sin\ a_nL)} \tag{3.4}$$

a_n is computed to satisfy the following equation:

$$cosh(a_nL).cosh(a_nL)+1=0 \tag{3.5}$$

Similarly, the j^{th} torsional mode is expressed by:

$$\phi_j = sin\left(\frac{2k-1}{2L}\pi x\right) \tag{3.6}$$

with boundary conditions:

$$\phi_j(x=0)=0 \qquad \phi_j'(x=L)=0 \qquad (j=n+1,n+2...n+m)$$

The complete eigenvalue problem is represented by [28]:

$$[\mathbf{K}+v^2\mathbf{H}+\lambda v\mathbf{L}+\lambda^2\mathbf{M}]a=0 \tag{3.7}$$

The eigenvalue, λ, is a function of the air speed v. When v is not zero, λ is complex and assumes the form:

$$\lambda = \alpha + i\omega \tag{3.8}$$

For small values of v, α is negative and hence the system's motion is damped since the wing loses energy to the surrounding air. As v increases, α increases until it reaches a positive value and the system becomes unstable.

The mass and stiffness matrices are defined as follows:

$$k_{ij} = \int_0^L EI\phi_i''\phi_j''dx \qquad (i,j=1,2...n)$$

$$k_{ij}=0 \qquad (i\neq j)$$

$$k_{ij} = \int_0^L GJ\phi_i'\phi_j'dx \qquad (i,j=n+1,n+2...n+m) \tag{3.9}$$

$$m_{ij} = m_{ji} = \int_0^L m\phi_i\phi_j dx \qquad (i,j = 1,2...n)$$

$$m_{ij} = m_{ji} = \int_0^L m y_\theta \phi_i\phi_j dx \qquad (i = 1,2...n; j = n+1, n+2n, ..., n+m)$$

$$m_{ij} = m_{ji} = \int_0^L I_\theta \phi_i\phi_j dx \qquad (i,j = n+1, n+2...n+m) \quad (3.10)$$

enforcing the orthogonality condition:

$$m_{ij} = 0 \qquad (i \neq j)$$

the aerodynamic matrix is defined as:

$$h_{ij} = 0 \qquad (i,j = 1,2...n)$$

$$h_{ij} = h_{ji} = \frac{\rho_F}{2}\frac{dC_L}{d\theta}\int_0^L c\phi_i\phi_j dx \qquad (i = 1,2...n; j = n+1, n+2n, ..., n+m)$$

$$h_{ij} = 0 \qquad (i = n+1, n+2...n+m; j = 1,2,...,n)$$

$$h_{ij} = -\frac{\rho_F}{2}\frac{dC_L}{d\theta}\int_0^L c^2\left(\frac{y_o}{c} - \frac{1}{4}\right)\phi_i\phi_j dx \qquad (i,j = n+1, n+2...n+m) \quad (3.11)$$

where y_o is the pitching axis and was assumed to be half the chord length.

$$l_{ij} = \frac{\rho_F}{2}\frac{dC_L}{d\theta}\int_0^L c\phi_i\phi_j dx \qquad (i,j = 1,2...n)$$

$$l_{ij} = \frac{\rho_F}{2}\frac{dC_L}{d\theta}\int_0^L c^2\left(\frac{3}{4} - \frac{y_o}{c}\right)\phi_i\phi_j dx \quad (i = 1,2...n; j = n+1, n+2n, ..., n+m)$$

$$l_{ij} = -\frac{\rho_F}{2}\frac{dC_L}{d\theta}\int_0^L c^2\left(\frac{y_o}{c} - \frac{1}{4}\right)\phi_i\phi_j dx \quad (i = n+1, n+2...n+m; j = 1,2,...,n)$$

$$l_{ij} = \frac{\rho_F}{2} \int_0^L c^3 \left[\frac{\pi}{8} - \left(\frac{y_o}{c} - \frac{1}{4} \right) \left(\frac{3}{4} - \frac{y_o}{c} \right) \frac{dC_L}{d\theta} \right] \phi_i \phi_j dx$$

$$(i, j = n+1, n+2, ..., n+m) \tag{3.12}$$

equation 3.7 is reformulated to reduce the problem to:

$$\mathbf{K^*} a^* = \lambda \mathbf{M^*} a^* \tag{3.13}$$

where:

$$\mathbf{K^*} = \begin{bmatrix} 0 & 1 \\ -(\mathbf{K} + v^2\mathbf{H}) & -v\mathbf{L} \end{bmatrix} \quad \mathbf{M^*} = \begin{bmatrix} 1 & 0 \\ 0 & \mathbf{M} \end{bmatrix}$$

Table 3.1 lists the parameters used to establish the beam model. Assuming a 2-DOF system (m=1, n=1), the matrices that follow are obtained using the aforementioned method.

Table 3.1: Cantiliever beam specifications

Property	
L [mm]	700
c [mm]	70
t [mm]	8.4
E [GPa]	1
G [GPa]	25.9
m [kg/m]	1.6288
ρ_s [kg/m^3]	2770

$$\mathbf{M} = \begin{bmatrix} 0.9613 & 0 \\ 0 & 0.0002 \end{bmatrix} \quad \mathbf{K} = \begin{bmatrix} 110.7340 & 0 \\ 0 & 24.3513 \end{bmatrix}$$

$$\mathbf{H} = \begin{bmatrix} 0 & 0.1181 \\ 0 & -0.0017 \end{bmatrix} \quad \mathbf{L} = \begin{bmatrix} 0.1590 & 0.0021 \\ -0.0021 & 0.000016 \end{bmatrix}$$

The natural frequencies could be generated using the classical analysis by solving the eigenvalue problem shown in equation 3.14.

$$\mathbf{K}a = -\lambda^2 \mathbf{M}a \tag{3.14}$$

Table 3.2 lists the natural frequency of the bending and torsional mode.

Table 3.2: Natural frequencies of the cantilever beam model

Mode	Frequency [Hz]
Bending mode	1.7081
Torsional mode	51.1101

The eigenvalue problem of equation 3.13 is then solved for a variety of air velocities to determine the critical flutter speed. Figure 3.1 plots the values of the real part of the eigenvalues as the air velocity is increased. Figure 3.2 plots the imaginary values of the eigenvalue which represent the frequency plot. The flutter speed for the model was encountered at 68 m/s as it is the first instance when α reaches a value greater than zero. This bending mode was also observed to flutter at a low frequency compared to the torsional mode, as shown in figure 3.2.

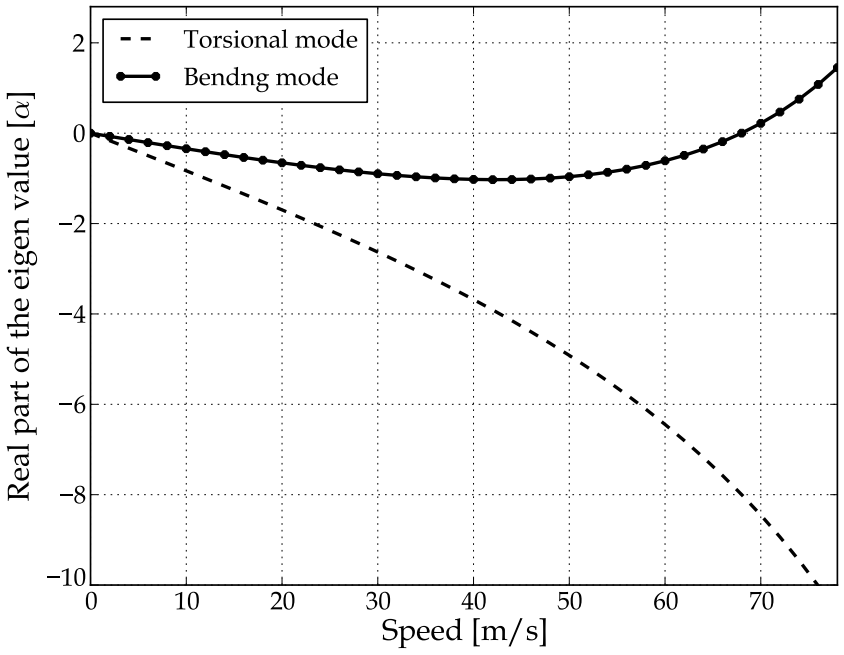

Figure 3.1: Damping plot

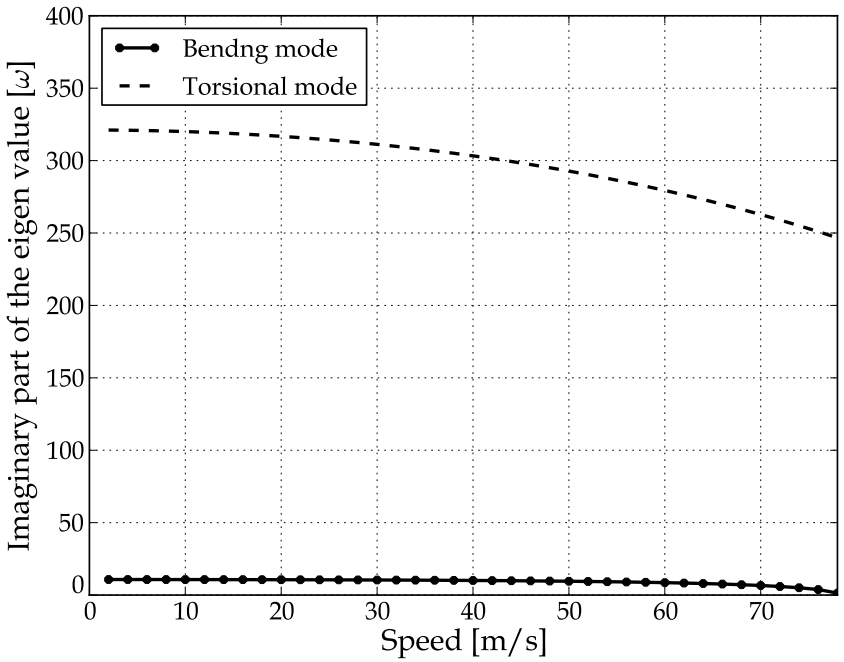

Figure 3.2: Frequency plot

Chapter 4

Structural environment

The following chapter elaborates on the structural environment. The wing's geometry and material are discussed before detailing the manner in which the CAD models were created. The connection used to secure the ailerons to the wing is discussed before detailing the process in which the FE model was discretized. The modal analysis used to determine the wing's natural modes and corresponding frequencies is then documented. The base excitation used to excite the first natural mode is elaborated on and lastly, the surfaces which formed part of the FSI interface are discussed.

4.1 Geometry and CAD model

The geometry was selected to be suitable for the creation of a high-aspect-ratio wing. The NACA 0012 aerofoil was chosen for its simplistic profile and the availability of additional test data over a wide range of test conditions, which offers a means of validating the model [30]. In addition to yielding a high-aspect-ratio wing, the wing's dimensions were chosen such that it would be possible to conduct testing in a wind tunnel. In order to yield a high-aspect-ratio wing, the wing's chord and span were chosen as 70 mm and 1400 mm respectively, to generate an aspect ratio of 20 (see table 4.1). Figure 4.1 depicts the aerofoil generated from 102 data points.

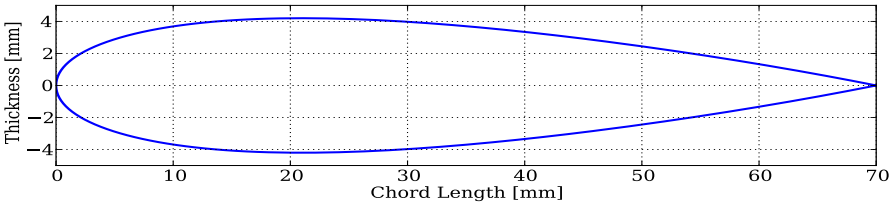

Figure 4.1: NACA 0012 aerofoil

Table 4.1: Wing geometry

Property	
Chord [mm]	70
Wing span [mm]	1400
Material	Aluminium Alloy

An aluminium alloy was chosen as the material for the wing and control surfaces. The wing and control surfaces were created as solid bodies, meaning structural components such as spars, ribs and internal braces were neglected. Although this is not representative of an actual wing, it simplifies the problem but remains sufficient for the scope of the project. The resulting structure was however too rigid. Appendix A.2 details the procedure in which the structure's bending stiffness was decreased. The area, centroid axis and area moment of inertia of the NACA 0012 aerofoil were computed before the bending stiffness of the wing was determined. The bending stiffness, using the default properties of the aluminium alloy, exhibited a large value compared to those found in other studies. The Young's modulus was therefore decreased to yield a less rigid structure. The material properties of the aluminium alloy are shown in table 4.2 where the Young's modulus was decreased from 10 GPa to 1 GPa. These material properties were used in the final FSI model for both the wing and ailerons.

Table 4.2: Structure material properties

Property	
Young's modulus [GPa]	1
Modulus of Rigidity [GPa]	25.9
Density [kg/m^3]	2770
Poisson's ratio	0.33

The flutter-suppression control system made use of the standard control surfaces on the wing, as stated in section 1.2. Section 2.2 conducted a study of the control surfaces that may be present on a wing. Control surfaces have previously been used in mathematical studies, in which aeroelastic vibrations were successfully suppressed [31] [32]. Ailerons possess a rotational DOF capable of rotating about an axis, parallel to the span of the wing, in both clockwise and anti-clockwise directions. Although the design of an aircraft may vary from one to another, ailerons were ultimately chosen as the control surfaces to be used in the control system. Ailerons are typically found on the outboard of the wing. A total of 6 ailerons were used in the FSI model.

CAD models of the wing and ailerons were created using Autodesk Inventor. The wing and ailerons are shown in figures 4.2a and 4.2b respectively. The areas devoid of material on the wing were used to accommodate the 6 ailerons. All the ailerons were identical in geometry and were placed along the span of the trailing edge. Dimensions of both the wing and ailerons are presented in Appendix A.1.

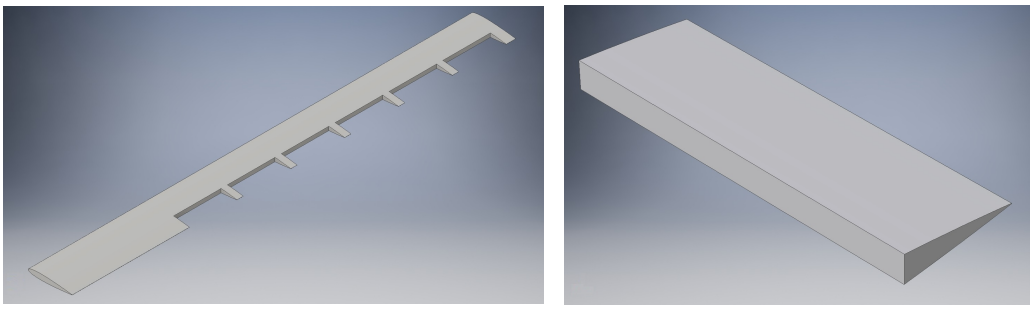

(a) (b)

Figure 4.2: CAD models of the (a) wing and (b) ailerons

The assembled wing is shown in figure 4.3. Modelling a direct connection between the wing and aileron would compromise the mesh as it would require protrusions and cavities to form the connection. A remote connection was therefore used to locate each aileron to the wing, in order to retain a desirable mesh. These remote connections restrained all the ailerons' DOF except for its rotational DOF which permitted the ailerons to rotate about the axis parallel to the span of the wing.

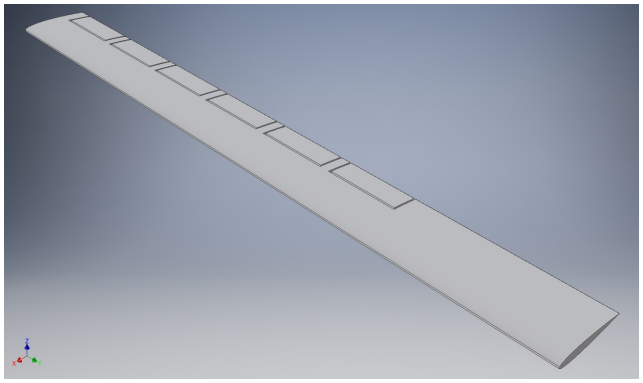

Figure 4.3: Fully assembled wing

Each aileron was identified with a name which would allow the control system to select the ailerons based on these names. Figure 4.4 identifies each aileron on the wing, starting with Aileron1 (located furthest to the outboard) to Aileron6 (located closest to the base of the wing).

These names are consistent with those used in the control system documented in Appendix C (further explained in section 6). Permitting the control system to access the ailerons, via their respective names, allowed the control system to manipulate the ailerons' rotational DOF.

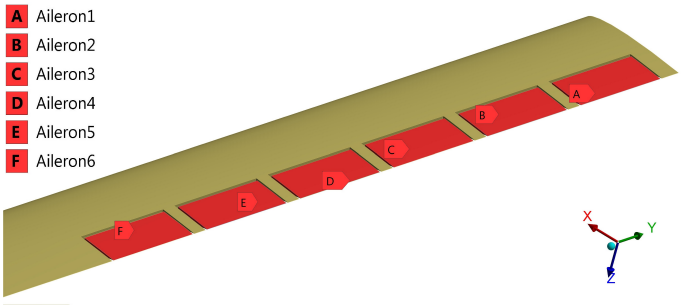

Figure 4.4: Identification of the ailerons

The revolute connection, provided in ANSYS, was used to connect each aileron to the wing. These remote connections are shown in figure 4.5. Each aileron required two revolute connections to locate its sides to the wing's adjacent surfaces. Figure 4.5 illustrates how two revolute connections, A and B, were applied to the sides of Aileron1 to link them against the adjacent sides of the wing. A local coordinate system is defined against the edge of the aileron to allow the desired rotational DOF, about the z-axis. As mentioned previously in section 2.3, control surfaces could contribute to the flutter mechanism. Since the aim of this project was to suppress vibration with the use of the control surfaces, it was assumed that ailerons did not contribute to the flutter mechanism. This was achieved by not assigning a rotational stiffness for the wing-aileron connection and fixing the rotational DOF once the aileron's rotation was altered. This implies that the aileron was fully fixed once the control system altered its DOF.

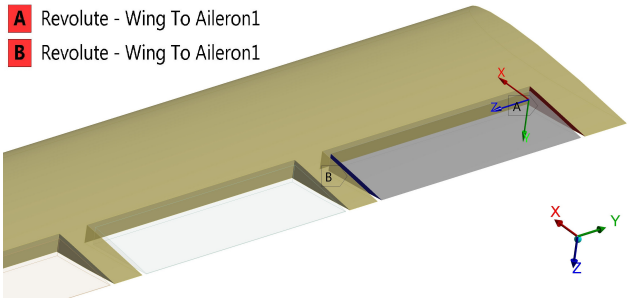

Figure 4.5: Revolute connection

4.2 FE model

ANSYS provides solid shell elements (SOLSH190) which are applicable for structures with a thin to moderate thickness [33]. Therefore, discretization of the wing and ailerons made use of these elements. Meshing of the structure required two parallel faces which, in turn, required the chord to be trimmed by 1% (0.5% at both the leading and trailing edge [7]). Brandsen (2013) documented the use of solid shell elements, where compressor blades were discretized in a similar manner, which yielded promising results. Figures 4.6 and 4.7 depicts the meshed wing and ailerons using the SOLSH190 elements.

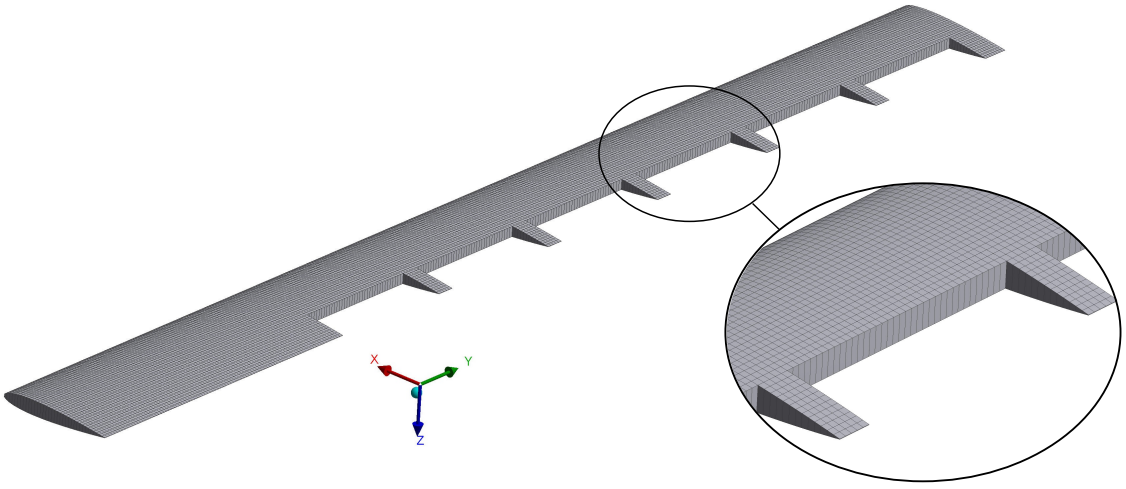

Figure 4.6: FE model of the wing

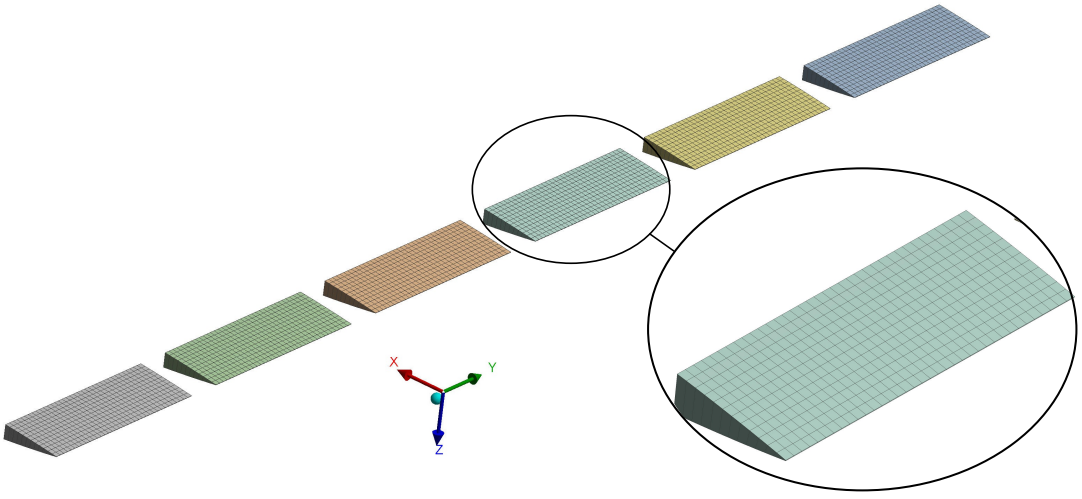

Figure 4.7: FE model of the ailerons

Mesh refinement was performed on the FE model to achieve mesh independence. Table 4.3 lists the details of the coarse, medium and fine meshes used in the FE refinement process.

Table 4.3: Mesh refinement of the FE model

Mesh	Elements	Nodes
Coarse	1,350	3,240
Medium	5,418	11,858
Fine	12,228	25,974

The following documents the refinement process of the FE model, where the 3 meshes of varying densities were used. The wing tip displacement, using the fine, medium and coarse meshes, are illustrated in figure 4.8. All 3 simulations used a base excitation with an amplitude of 0.001 mm (as described in section 4.4).

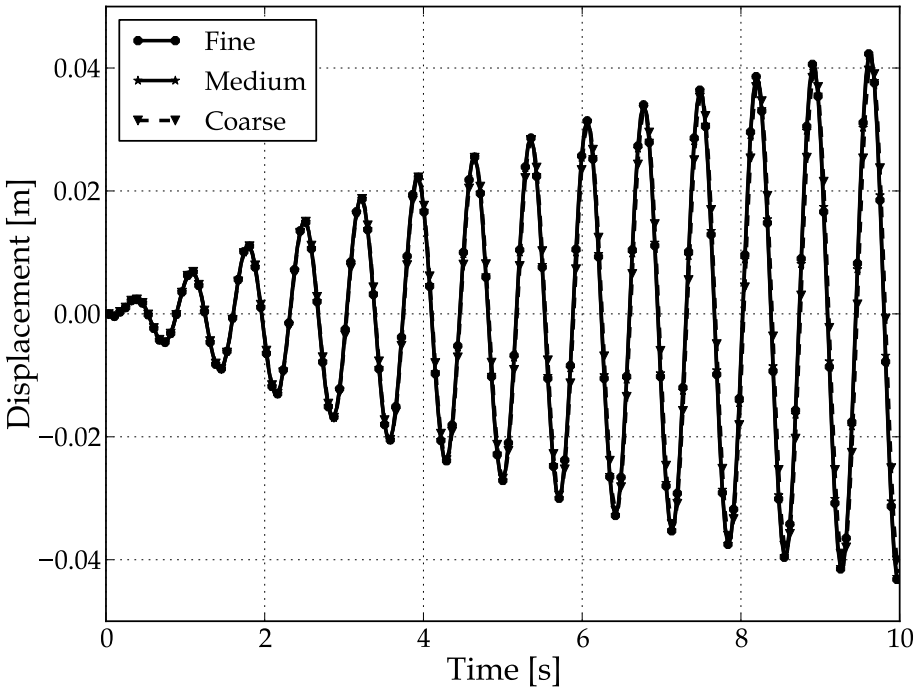

Figure 4.8: FE mesh refinement

Figure 4.9 is an enlarged view of figure 4.8, between 8 s and 10 s. The curve of the coarse mesh was observed to slightly lag behind the curves of the medium and fine meshes. Also, the amplitude of the curve generated from the coarse mesh was observed to be slightly smaller compared to those generated from the medium and fine meshes.

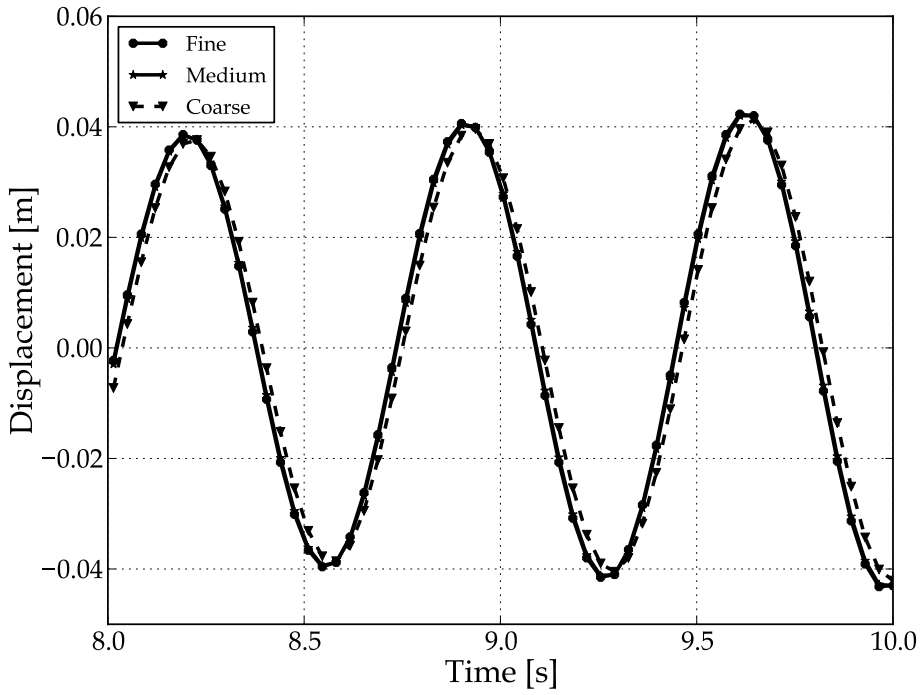

Figure 4.9: Enlarged view of the FE mesh refinement

This refinement process revealed that the curves generated from using the 3 meshes were almost coincident and therefore, all 3 meshes were declared mesh independent. However, the fine mesh was used in the FSI model as the computational effort for the FE model was negligible, compared to that of the CFD model.

In addition, ANSYS Inc (2005) states that the data transfer algorithms use a combination of mapping/interpolation algorithms for a multi-physics simulation. The precision of data transferred to the target of the interface is restricted by the least refined part of the interface. Selecting the fine mesh would therefore also provide better data transfer between the structural and fluid environments.

4.3 Modal analysis

A modal analysis was performed to determine the structure's natural modes and their corresponding frequencies. The following documents the modal analysis of the fine mesh. As stated previously, the ailerons were constrained in a manner to ensure that their own natural modes did not contribute to the analysis. Therefore, the modal analysis computes the natural modes of the wing, without the influence of the ailerons' DOF. However, the mass of the ailerons are still taken into account and subsequently influenced the mass matrix of the entire strucutre. The first 5 natural modes were computed.

Table 4.4 lists the natural frequencies of the wing and their corresponding dominant modes.

Table 4.4: Results of the structure's modal analysis

	Frequency [Hz]	Dominant mode
First	1.4091	Bending
Second	8.7856	Bending
Third	11.273	In-plane
Fourth	24.483	Bending
Fifth	32.739	Torsional

Figure 4.10 depicts the first natural mode where bending is dominant. Figures 4.11a - 4.11d depict the next four natural modes as listed in table 4.4. Huang *et al.* (2012) states that in-plane natural modes contribute much less to flutter. The in-plane mode at the third natural frequency was therefore neglected. The bending modes are the most common mode shapes amongst the 5 generated. This could be attributed to the geometry of the high-aspect-ratio wing. Huang *et al.* (2012) also documented the natural frequencies of a low-aspect ratio wing where the first and second frequencies were a bending and torsional mode, respectively. In addition, the increase between the two frequencies was not as large as was observed in the modal analysis for this project. Since the motion of a strucutre may be thought of as the superposition of its natural modes, the dominant mode expected would be a bending mode.

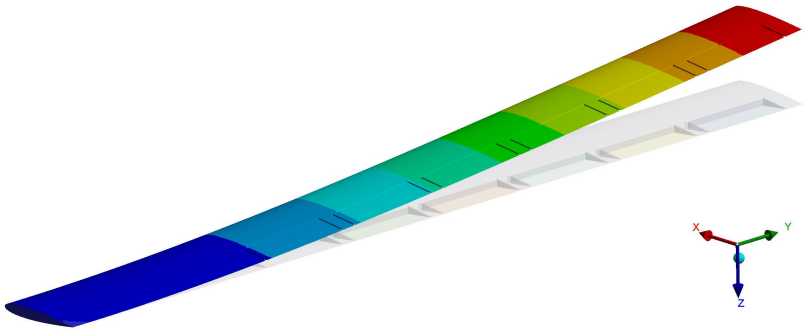

Figure 4.10: First natural mode of the structure

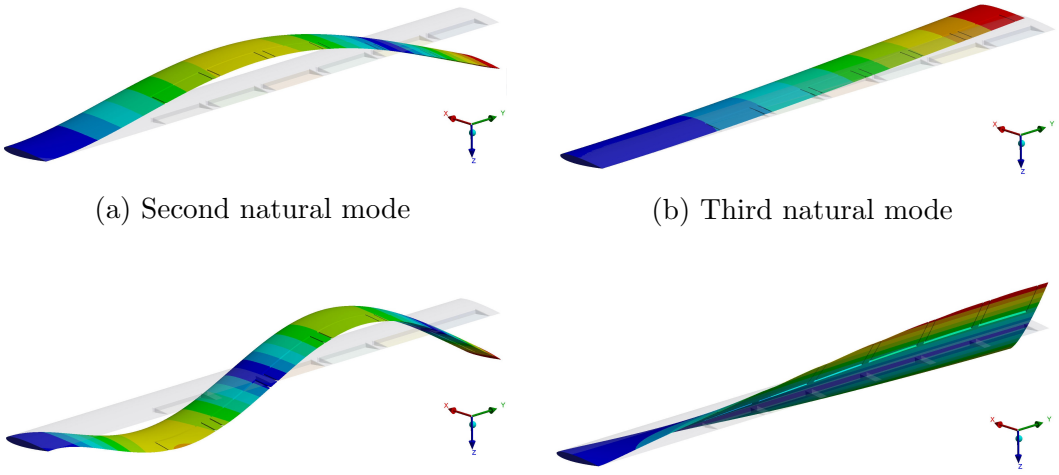

(a) Second natural mode

(b) Third natural mode

(c) Fourth natural mode

(d) Fifth natural mode

Figure 4.11: Subsequent natural modes of the structure

Modal analysis of the coarse, medium and fine meshes were performed to ensure the natural frequencies and their corresponding natural modes were independent of the mesh. The results of the modal analysis indicated that the natural frequencies amongst the 3 meshes were almost identical (see table 4.5). The largest difference observed was between the fine and coarse meshes with a difference of 0.44%, at the first natural frequency. This difference was deemed negligible. The natural modes generated amongst the 3 meshes were also identical which led to the conclusion that the natural modes and corresponding frequencies were all declared mesh independent.

Table 4.5: Modal analysis of the fine, medium and coarse meshes

	Fine [Hz]	Medium [Hz]	Coarse [Hz]
Mode 1	1.4091	1.4082	1.4028
Mode 2	8.7856	8.7802	8.7438
Mode 3	11.273	11.267	11.232
Mode 4	24.483	24.469	24.369
Mode 5	32.739	32.747	32.608

4.4 Base excitation

Equation 4.1 accounts for a harmonic base excitation, as defined by Inman (2014). Y represents the amplitude of the base motion, f the frequency of the base oscillation and the t the time. A base excitation was used to excite vibration of the first bending mode at its excitation frequency.

$$y_o(t) = Y \sin(2\pi f t) \tag{4.1}$$

ANSYS uses the Rayleigh damping model to compute the damping matrix. This viscous model, documented in section 2.4, is expressed by equation 2.11. Cook *et al.* (2007) states that structural damping is typically small and in the order of $\xi < 0.15$. The α and β parameters were solved using equation 2.12. Setting $\beta = 0$, $\xi = 0.01$ and using the results of the modal analysis of the first natural frequency, yielded $\alpha = 0.175929$. The damped natural frequency could therefore be determined, using equation 2.13 , as $f_d = 1.409$ Hz. Substituting a desired amplitude and the damped natural frequency yielded equation 4.2, which accounts for the base excitation used for the wing. The values for α and β were used in the Rayleigh damping model in the structural environment and the damped natural frequency was used in the base excitation equation. The process of determining the damped natural frequency was a formality as it was expected that the damping of the FSI model would be dominated by the aerodynamic damping, not the structure's damping. The base excitation is shown in figure 4.12. This translational base excitation was applied to the base of the wing.

$$y_o(t) = 0.001 \sin(2\pi(1.409)t) \tag{4.2}$$

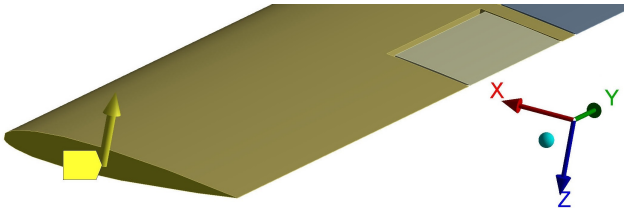

Figure 4.12: The translational base excitation applied at the base of the wing

4.5 FE FSI interface

Section 2.6 stated that a FSI interface was required between the structural and fluid environments, for the exchange of data. The FSI interface was defined on the wing and aileron surfaces, shown in figure 4.13. All the exterior surfaces were defined as part of the FSI interface as the wing was completely submerged

in the fluid. The adjacent areas between the ailerons and the wing were not defined as part of the interface as fluid was not present in these areas. The forces generated in the CFD solver are transferred to the FSI interface. In turn, the displacements calculated by the FE solver are transferred to the FSI interface defined in the CFD model (see section 5.7).

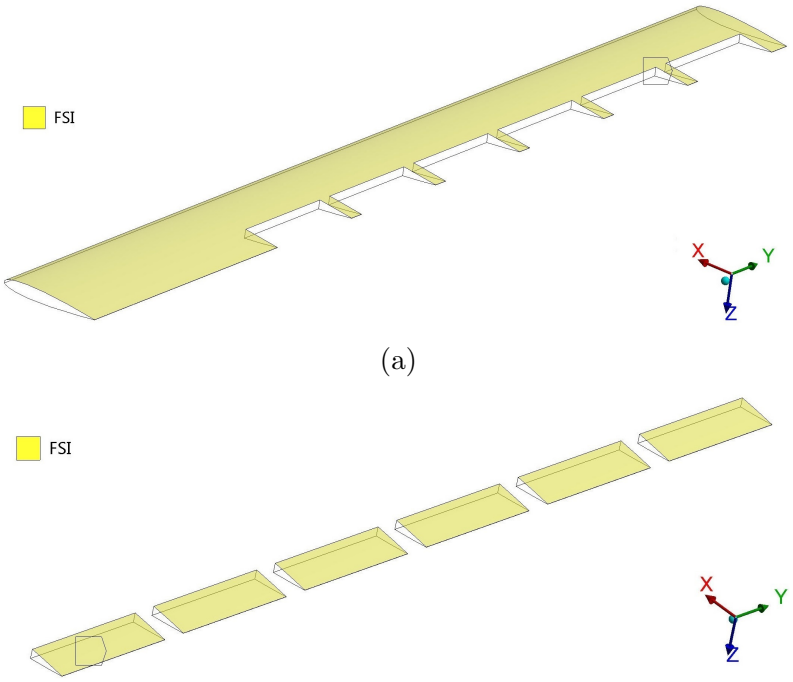

Figure 4.13: FSI interface defined on the (a) wing and the (b) ailerons surfaces in the FE model

Chapter 5

Fluid environment

The following chapter describes the construction of the fluid environment. The choice and reasoning for the fluid domain geometry are discussed, followed by the CFD discretization process. The mesh, boundary conditions, fluid properties, choice of turbulence model, dynamic mesh settings and wall functions are then discussed. The chapter concludes by illustrating what surfaces were defined as part of the CFD FSI interface.

5.1 Geometry and CAD model

The geometry of the fluid domain used dimensions 10×6 chord lengths. Figure 5.1 illustrates the fluid domain which made use of the aforementioned dimensions where 6 chords lengths (denoted by c) are used from the leading edge of the wing and 10 chord lengths are used from the trailing edge of the wing. This geometry was used as Mohammadi and Johari (2010) stated that a domain of 7×4 was not adequate for modelling a wing. The fluid domain spans 1000 mm, allowing 300 mm to account for the free-end since the wing spans 700 mm

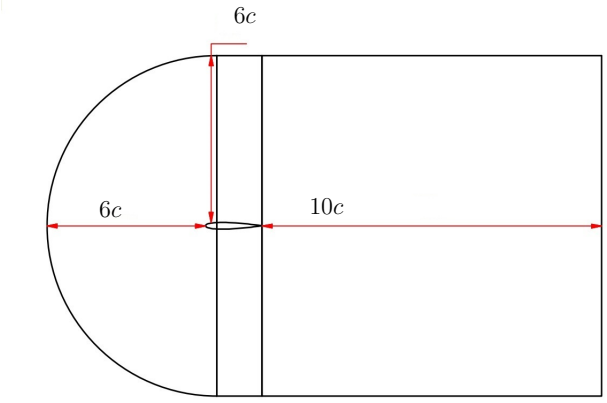

Figure 5.1: Fluid domain geometry

The CAD model for the fluid domain was generated using AutoDesk Inventor. Figure 5.2 depicts the 3-dimensional model of the meshed fluid domain. The fluid domain was partitioned to allow better control with regards to the generation of the mesh. Specifically to apply biasing on the edges of the mesh and to enforce a structured mesh in certain sections of the CFD model.

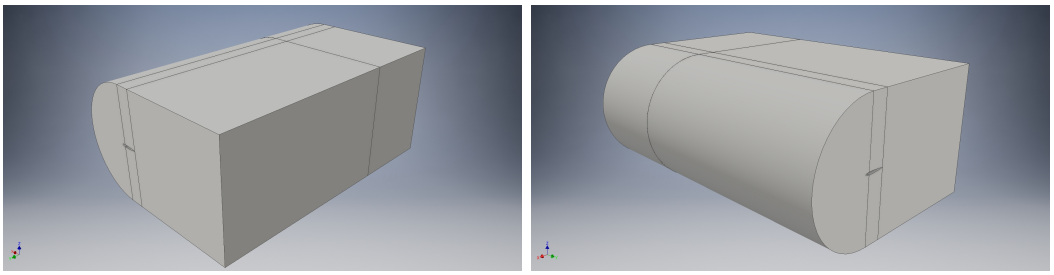

(a) (b)

Figure 5.2: CAD model

5.2 CFD model

Biasing of the fluid domain is shown in figures 5.3a and 5.3b. The edges labelled A-G were assigned a bias rate and sized according to a number of elements. Table 5.1 lists the number of elements and bias rate used on each edge in the fluid domain.

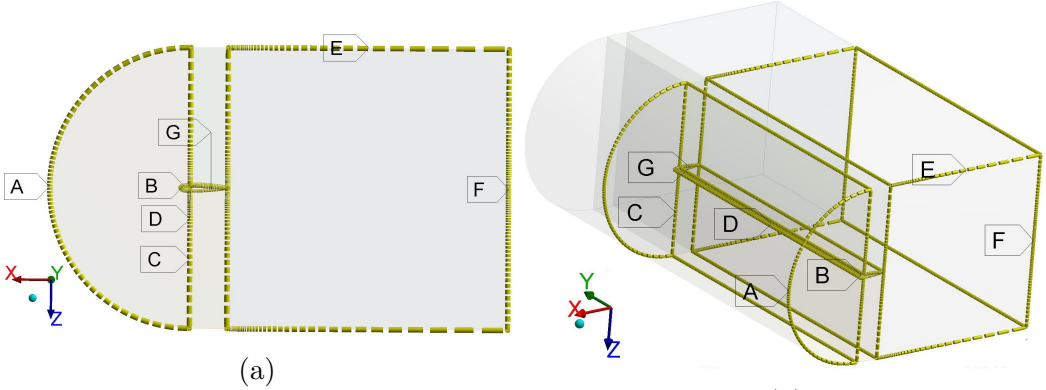

(a) (b)

Figure 5.3: Biasing of the fluid domain

Table 5.1: Edge sizing and bias rate

Edge	Number of edges	Number of elements	Smooth transition
A	2	60	1.05
B	4	30	1.15
C	8	40	1.1
D	10	125	-
E	4	50	1.12
F	2	80	1.05
G	4	50	1.1

The front view of the meshed fluid domain is shown in figure 5.4a. The aforementioned biasing of the fluid domain is evident as the resolution of the mesh is greater at the boundary for the wing. The greater mesh density was used to account for the boundary layer effect adjacent to the wing's surface. Figure 5.4b depicts the enlarged front view of the mesh.

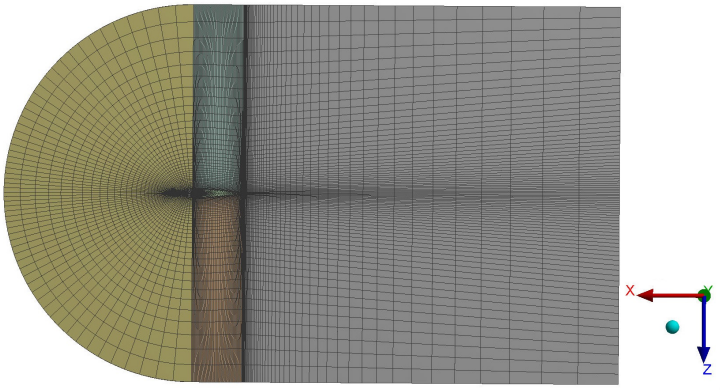

(a)

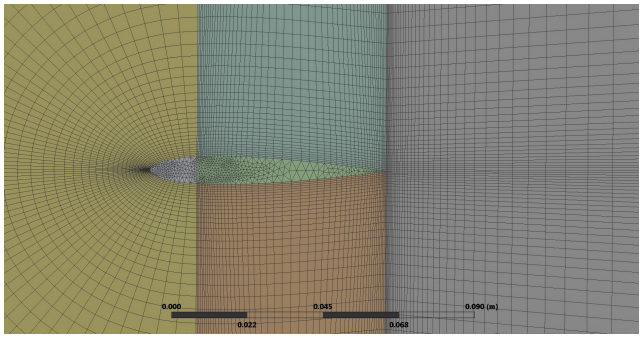

(b)

Figure 5.4: Front view of the meshed fluid domain

Partitioning of the fluid domain allowed partial sections to make use of a structured mesh, while other sections made use of an unstructured mesh. Figure 5.5 depicts a sectioned view of the CFD model, illustrating the sections which used a structured mesh and the sections which used an unstructured mesh. The sections, in which the wing was located, consisted entirely of hexahedral elements. The adjacent section, downstream, also consisted of hexahedral elements. The domains which models the free-stream sections consists of tetrahedral elements.

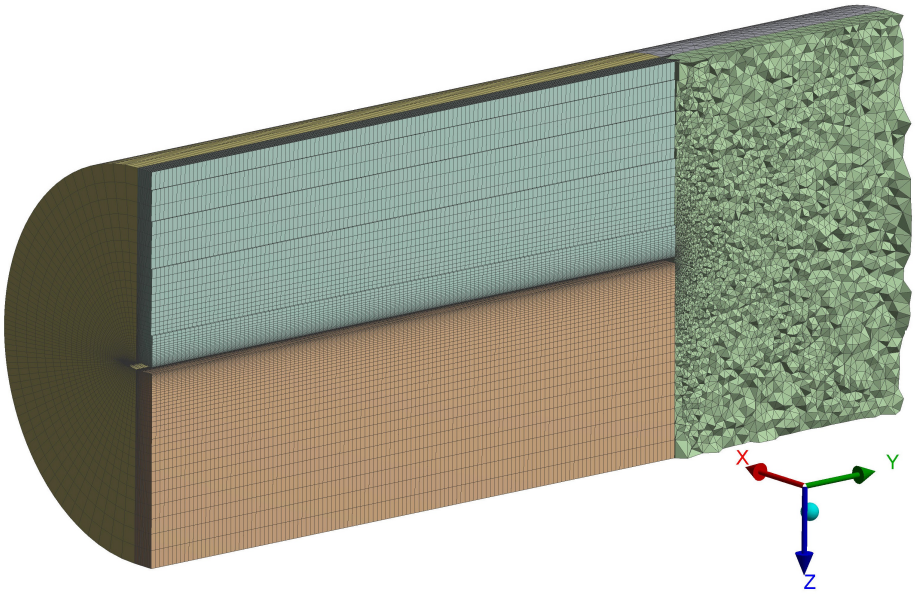

Figure 5.5: Sectioned view of the CFD model

Similarly to the FE model, a mesh refinement process was followed for the CFD model. Once again, a coarse, medium and fine mesh were used in the process of proving mesh independence. Table 5.2 lists the details of the coarse, medium and fine meshes. Mesh independence was critiqued using the wing's tip displacement.

Table 5.2: Mesh refinement of the CFD model

Mesh	Elements	Faces	Nodes
Coarse	510,515	1,313,275	329,808
Medium	1,452,584	2,872,865	652,801
Fine	1,889,854	3,842,255	1,221,365

Figure 5.6 depicts the curves generated of the wing's tip displacement, using the fine, medium and coarse meshes. The curve of the coarse mesh was observed to deviate from the curves generated from the fine and medium meshes.

The wing tip displacement was expected to oscillate about the resting position, unlike the coarse mesh. Therefore, the coarse mesh was not deemed mesh independent. An enlarged view is shown in figure 5.7. The results from the medium and fine meshes were nearly coincident, however, the fine mesh was selected as this mesh satisfied the criteria for the wall functions, stated in section 5.6.

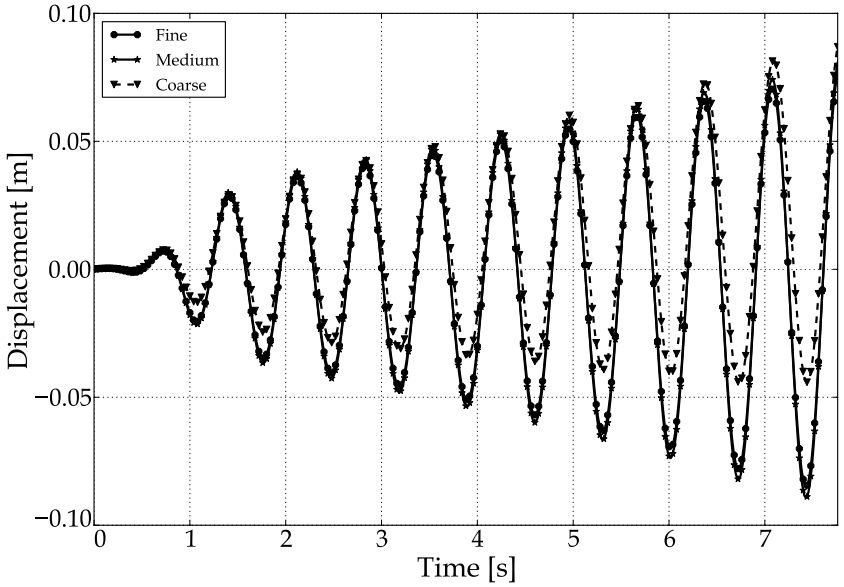

Figure 5.6: CFD mesh refinement

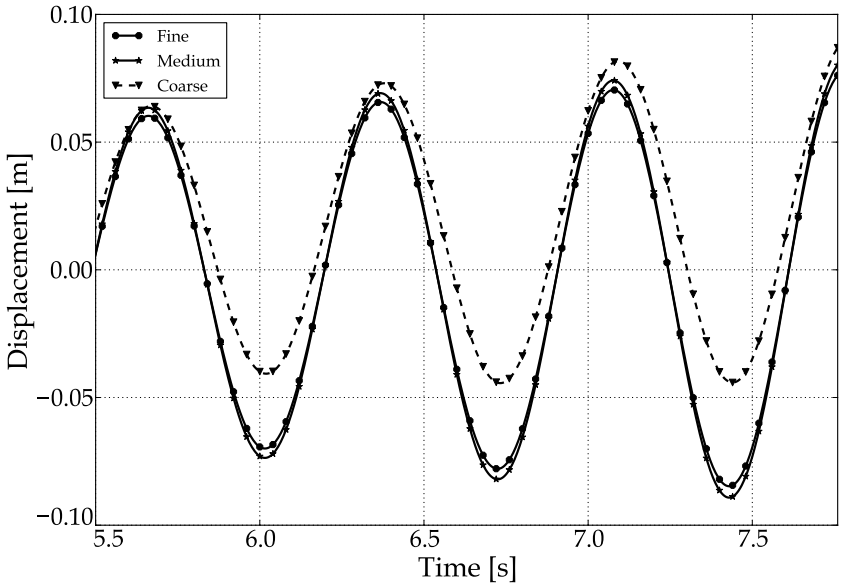

Figure 5.7: Enlarged view of the CFD mesh refinement

5.3 Fluid properties

The properties of the fluid are listed in table 5.3. In order to determine whether a turbulence model was required, the type of flow regime was determined by computing the Reynolds number.

Table 5.3: Fluid properties

Named surface	Boundary type
Speed [m/s]	50
Density [kg/m^3]	1.225
Dynamic viscosity [kg/(m$\cdot$ s)]	1.7×10^{-5}

The Reynolds number was determined using equation 5.1 where the chord length of the wing, was used and the aforementioned air properties in table 5.3 were used for the fluid properties. Kays *et al.* (2005) states that transition to a turbulent type of boundary layer, over a flat plate, tends to occur when the Reynolds number is in the order of $300,000 - 500,000$. Laminar flow was therefore not expected, which implied a turbulence model was required for the FSI simulation. Although a flat plate does not truly represent an aerofoil, this assumption was deemed conservative as the cavities used to accommodate the control surfaces would induce turbulent flow.

$$Re = \frac{\rho\ v\ c}{\mu} = \frac{(1.225)\ (50)\ (0.07)}{1.7 \times 10^{-5}} = 2.5 \times 10^5 \tag{5.1}$$

5.4 Turbulence model

Section 2.5 elaborated on some of the different RANS based turbulence models used in practice. Ultimately, the $SST\ k-\omega$ turbulence model was selected for the CFD model. The $SST\ k-\omega$ is a variation of the $k-\omega$ turbulence model which was developed by Menter (1994) in an effort to blend the robustness and accuracy of $k-\omega$ model, at the near-wall region, and the $k-\epsilon$ model which offers the free-stream independence in the far field. This is achieved using a blending function where the turbulence model alternates between the $k-\omega$ model for near-wall regions and the $k-\epsilon$ model in the far field. The $SST\ k-\omega$ turbulence model is thus more accurate and reliable for a wider range of fluid flow [38]. In addition, Eleni *et al.* (2012) concluded that the $SST\ k-\omega$ model was an appropriate turbulence model when modelling a NACA 0012 aerofoil.

5.5 Boundary conditions and dynamic mesh settings

The following section details the boundary conditions and dynamic mesh settings used in the CFD model. Figure 5.8 depicts the CFD model with its Inlet, Outlet, FSI, Wall and Basewall boundaries. The FSI boundary (which also functioned as the FSI interface) is concealed within the model. Figures E.1 and E.2 in Appendix E show comprehensive views of the CFD boundaries. Table 5.4 lists the boundaries of the CFD model, with their corresponding boundary type and dynamic mesh type (if applicable).

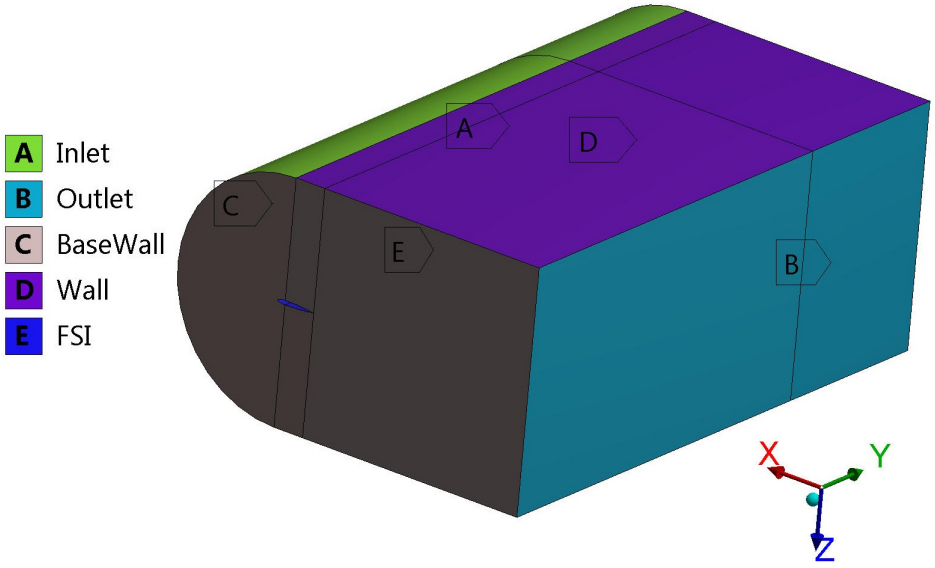

Figure 5.8: CFD boundaries

Table 5.4: Boundary type and dynamic mesh settings

Boundary	Boundary type	Dynamic mesh type
FSI	Wall	System coupling
Inlet	Velocity inlet	-
Outlet	Pressure outlet	-
Basewall	Symmetry	Deforming
Wall	Wall	-

The Inlet boundary was used to define the velocity and scalar properties of the fluid. ANSYS Inc (2009) recommends using this boundary for incompressible flows as compressible flows will generate non-physical results. The inlet air velocity was defined to be parallel to the x-axis and therefore the y- and z- velocity components were defined with zero values. The air velocity was ramped up during the simulation. This yielded a system which was much more stable as the convergence of the solution and remeshing of the dynamic mesh benefited from a gradual increase in air velocity. Figure 5.9 depicts the function used in the ramping of the air velocity. The simulation began with a zero velocity before it increased, linearly, to reach a maximum desired air velocity of 50 m/s at a time of 1 min. This maximum velocity was then sustained throughout the rest of the simulation. The Outlet boundary was defined as a pressure outlet where the static pressure was assigned a value of zero. The FSI boundary was defined as a wall and system coupling boundary to allow it to form part of the FSI interface. The Basewall boundary was defined as a symmetry and deforming boundary since the mesh of this boundary was expected to deform because of the base excitation. Lastly, the remaining boundary was the Wall boundary which was defined as zero slip walls.

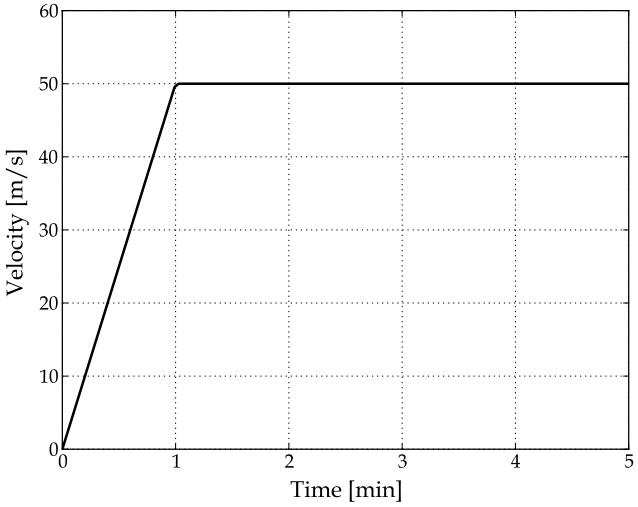

Figure 5.9: Ramping of the air velocity

Subsequent deformation of the CFD model's mesh, stemming from the structure's displacement, was accounted for by using a dynamic mesh. The smoothing and local remeshing methods were used to update the deforming fluid domain. The local remeshing method was used to remesh locally at deformed boundaries. If the moving boundaries' displacements were large, compared to the elements' local cell sizes, elements become too distorted and negative cell volumes could be encountered. To avoid this, ANSYS FLUENT agglomerates elements that fail to meet the skewness or size criteria. The CFD mesh proceeds to remesh the collected elements until it meets the threshold for the desired criteria [22].

5.5.1 Spring-based remeshing

The spring-based remeshing scheme assumes a network of interconnected springs between any two mesh nodes. Displacement of the nodes induces a force proportional to the displacement. This force can be represented by Hook's Law, shown by equation 5.2 [22].

$$\overrightarrow{F}_i = \sum_{k}^{n_i} s_{ik}(\Delta\ \overrightarrow{x}_k - \Delta\ \overrightarrow{x}_i) \tag{5.2}$$

where n_i represents the number of neighbouring nodes linked to node i, s_{ij} represents the stiffness constant, $\Delta\ \overrightarrow{x}_i$ and $\Delta\ \overrightarrow{x}_k$ represents the displacements at node i and its neighbouring node k. This remeshing scheme is typically used on fluid zones where the mesh is composed of triangular or tetrahedral elements. For instances when non-tetrahedral zones are used, this remeshing scheme is only recommended when the moving boundary's motion is predominantly in one direction and if the motion is normal to the boundary itself. Not complying with the aforementioned conditions may result in elements with high skewness [22]. Using this remeshing scheme for the FSI simulation resulted in generating negative cell volumes which could be attributed to the use of hexahedral elements in the CFD model. In addition, the mesh deformation was also not in one direction since the wing tip displacement was observed to oscillate about the resting position. The spring-based remeshing scheme was therefore replaced with the diffusion-based remeshing scheme.

5.5.2 Diffusion-based remeshing

The diffusion equation governs the diffusion-based remeshing scheme, expressed by equation 5.3.

$$\nabla\cdot(\Gamma\nabla\overrightarrow{x}) = 0 \tag{5.3}$$

where mesh displacement is represented by $\overrightarrow{x}$. This remeshing scheme proves to be more computational intensive however, it tends to generate better quality meshes (particularly for non-tetrahedral elements) than its counterpart and often allows larger boundary deformations. This remeshing scheme is also available for all element types [22]. Use of this scheme proved more robust than the spring-based remeshing scheme as negative cell volumes were not generated for identical mesh deformation. The diffusion-based remeshing scheme was therefore used for this project where the diffusion function was based on boundary-distance. The diffusion parameter was set to a value of 0.5 to allow remeshing to occur away from the moving boundary to maintain the mesh structure near the wing.

This remeshing method was based on the elements' minimum length scale, maximum length scale, maximum cell skewness and maximum face skewness in which marking of the elements occurred at every 5 intervals. Table 5.5 lists the parameters used in the smoothing and local remeshing methods.

Table 5.5: Dynamic mesh parameter settings

Parameter	Value
Diffusion parameter	0.5
Minimum length scale [m]	0.001819
Maximum length scale [m]	0.097235
Maximum cell skewness	0.914051
Maximum face skewness	0.702082
Size Remeshing interval	5

5.6 Wall functions

The presence of wall boundaries in a CFD model significantly affects the turbulent flow. Experiments have indicated that a multi-layered structure exists in the near-wall turbulent boundary layer, shown by figure 5.10. This multi-layered structure begins with a viscous sub-layer where the flow is almost completely laminar which means the fluid velocity is linear with distance from the wall. Next is the buffer region where the flow begins its transition to turbulent. The effects of viscosity and turbulence are equally important in this intermediate region. Lastly the turbulent core assumes the last regime of this multilayer multi-layered structure [40].

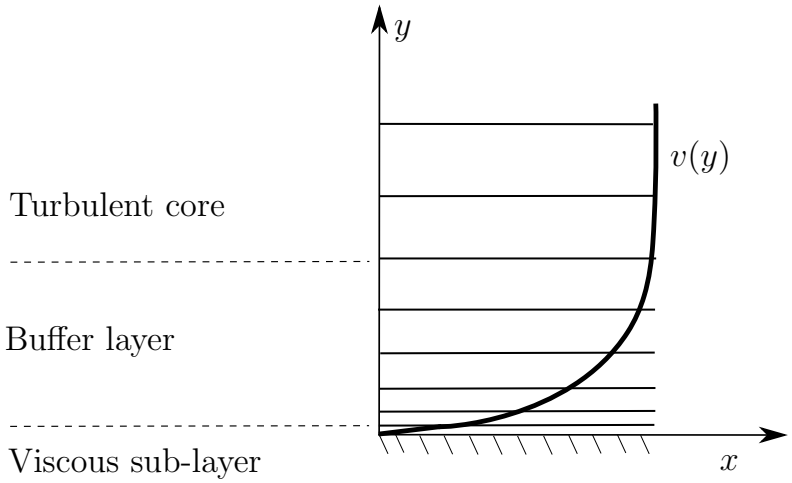

Figure 5.10: Multi-layered structure in the near-wall turbulent boundary layer

A strong and intricate interaction exists between turbulence and the fluid's mean flow. As a result, the numerical results of a turbulent flow simulation tend to be mesh dependent. Generating the mesh requires some consideration as mesh refinement should occur at regions where the mean flow experiences brisk changes and where the shear layers experience large strain rates. An upper and lower limit for the acceptable distance between the near-wall element's centroid and the wall is enforced. This distance is implemented using a dimensionless parameter, y^+ [22]. FLUENT Inc (2006) does not recommend having y^+ values that will have the first element located in the buffer layer, which occurs in the order of $5 < y^+ < 30$. In order to resolve the viscous sub-layer, FLUENT Inc (2006) recommends using a y^+ value in the order of $y^+ = 1$ to enforce enhanced wall treatment.

However, satisfying the criteria for enhanced wall treatment required extensive mesh refinement which would increase computational effort. It is also acceptable to enforce a standard wall function which entails using a y^+ value in the order of $30 < y^+ < 500$, where a value close to $y^+ \approx 30$ is most desirable [22] [6]. However, using y^+ values of this order results in an automatic wall treatment for the ω-equation in the $SST\ k - \omega$ turbulence model. This treatment automatically switches from the viscous sub-layer formulation to the wall function [40]. Nonetheless, this turbulence model was still deemed sufficient for the scope of the project.

The contour plots of the y^+ values used in the FSI model are shown in section B in figure B.1 where a maximum value of 255.2 and minimum value of 34.8 was observed on the wing.

5.7 CFD FSI interface

As performed in section 4.5 where a FSI interface was defined in the FE model, the fluid environment required a surface which would form part of the other half of the FSI interface. This surface was initially defined in table 5.4 where the FSI boundary was defined as a system coupling boundary to form part of the FSI interface, shown in figure 5.11. These surfaces are adjacent to the FE FSI interface defined in section 4.5 and forms the other half of the FSI interface.

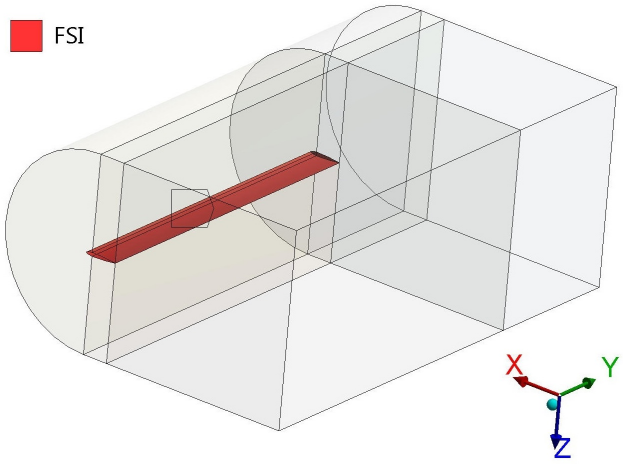

(a)

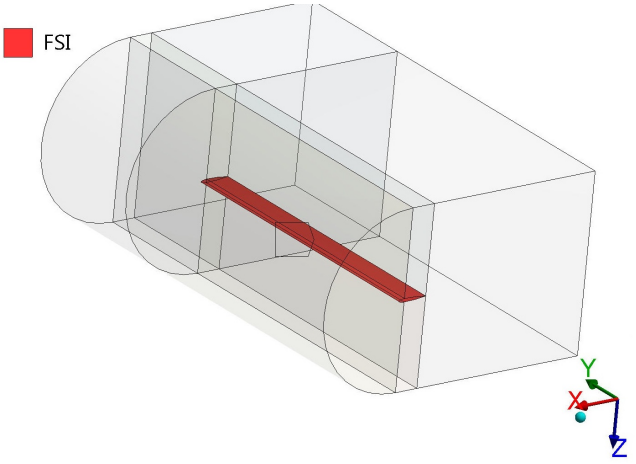

(b)

Figure 5.11: FSI boundary defined in the CFD model

Chapter 6

Control system

6.1 Linear quadratic controller

Initially, a proportional control system was used as a preliminary controller. This controller was elaborated on in section 2.7.2 however, the integral and derivative terms were neglected which yields a simple proportional controller. The framework used for the scripting was designed for this controller. A modern control law, in the form of a Linear Quadratic (LQ) controller, later replaced the proportional controller. The aforementioned framework was altered to accommodate the LQ controller (see Appendix C). Although a SISO control law was also used for this controller, Franklin *et al.* (2010) states that the state-variables method not only accounts for the input and output variables of the system but also the internal physical variables. The input variable would therefore be considered in the synthesis of the LQ controller unlike the proportional controller which might produce an input variable not obtainable by the system. In addition, state-space controllers are able to study linear, non-linear, time varying systems and are able to expand to a MIMO control law.

A LQ controller was chosen due to its successful implementation in smart structures [41] [42]. This type of controller requires the system to assume a state-space form, shown in equations 6.1a and 6.1b (adapted from Franklin *et al.* (2010)). These equations are modified from equations 2.31a and 2.31b to remain consistent with the notation used in section 2.6. Therefore, $\mathbf{x}^N$ and $\mathbf{u}^N$ denote the state-estimate and input-signal at the current time-step (N), respectively. These explicit discrete time-invariant equations also differ from the continuous time-invariant versions shown in section 2.7. The closed-loop feedback system is shown in figure 6.1. For the purpose of the project, the ailerons' rotational DOF was used in regulating the wing tip displacement since this approach has been performed, successfully, in previous studies [16] [43]. Each aileron were compensated with identical controller gains so they rotated with the same magnitude.

In accordance with figure 6.1, the wing's tip displacement was used as the output (y) whereas the ailerons' DOF was used as the input-signal (u).

$$\mathbf{x}^N = \mathbf{F}\mathbf{x}^{N-1} + \mathbf{G}\mathbf{u}^{N-1} \tag{6.1a}$$

$$\mathbf{y}^N = \mathbf{H}\mathbf{x}^{N-1} + J\mathbf{u}^{N-1} \tag{6.1b}$$

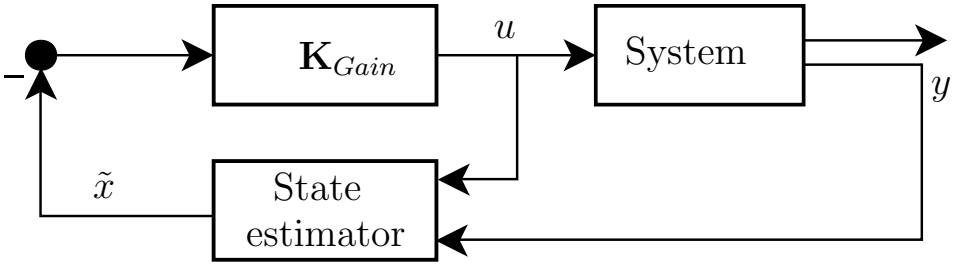

Figure 6.1: LQ control system [9]

Using the theory for constructing a full-order model of the system, as mentioned in section 2.7, an estimator was used to determine the state-estimate. This state-estimate was used in the feed-back of the control system to compute the controller's gain. Equation 6.2 was used in calculating the state-estimate whereas the input-signal is determined using equation 6.3 (adapted from Franklin *et al.* (2010)).

$$\tilde{\mathbf{x}}^N = \mathbf{F}\tilde{\mathbf{x}}^{N-1} + \mathbf{G}\mathbf{u}^{N-1} + \mathbf{L}(\mathbf{y} - \mathbf{H}\tilde{\mathbf{x}}^{N-1}) \tag{6.2}$$

$$\mathbf{u}^N = -\mathbf{K}_{Gain}\ \tilde{\mathbf{x}}^N \tag{6.3}$$

The LQ feed-back gain $\mathbf{K}_{Gain}$ is computed such that the infinite horizon cost function is minimised. Equation 6.4 accounts for the infinite horizon cost function [44] where $\mathbf{Q}$ and $\mathbf{R}$ represents the weighting parameters for $\mathbf{x}$ and $\mathbf{u}$, respectively.

$$J = \sum_{N=0}^{\infty} \left((\mathbf{x}^N)^T \mathbf{Q}\mathbf{x}^N + (\mathbf{u}^N)^T \mathbf{R}\mathbf{u}^N \right) \tag{6.4}$$

In order to minimise the cost function, equation 6.5 was used to compute the LQ feed-back gain. $\mathbf{P}$ is the solution of the discrete time algebraic Ricatti equation (DARE) and expressed by equation 6.6 [45].

$$\mathbf{K}_{Gain} = (\mathbf{R} + \mathbf{G}^T\mathbf{P}\mathbf{G})^{-1}\mathbf{G}^T\mathbf{P}\mathbf{F} \tag{6.5}$$

$$\mathbf{P} = \mathbf{Q} + \mathbf{F}^T(\mathbf{P} - \mathbf{P}\mathbf{G}(\mathbf{R} + \mathbf{G}^T\mathbf{P}\mathbf{G})^{-1}\mathbf{G}^T\mathbf{P})\mathbf{F} \tag{6.6}$$

6.2 State-space model

A simplified state-space model of the FSI system was constructed. This model can be determined from a first principle model, FE analysis or via experimental identification results. This project utilizes Matlab's System Identification toolbox, which entails estimating the state-space model of a system by supplying the toolbox with the system's input-data and corresponding output-data [45]. Assuming no particular knowledge of the internal structure of the system, a linear state-space model is estimated.

To compute a state-space model of the FSI, a characteristic behaviour simulation was performed in which the ailerons were forced to rotate with a desired input-signal which resulted in a subsequent output displacement of the wing tip. The wing tip displacement and ailerons' DOF curves are shown in figure 6.2 at an air velocity of 50 m/s.

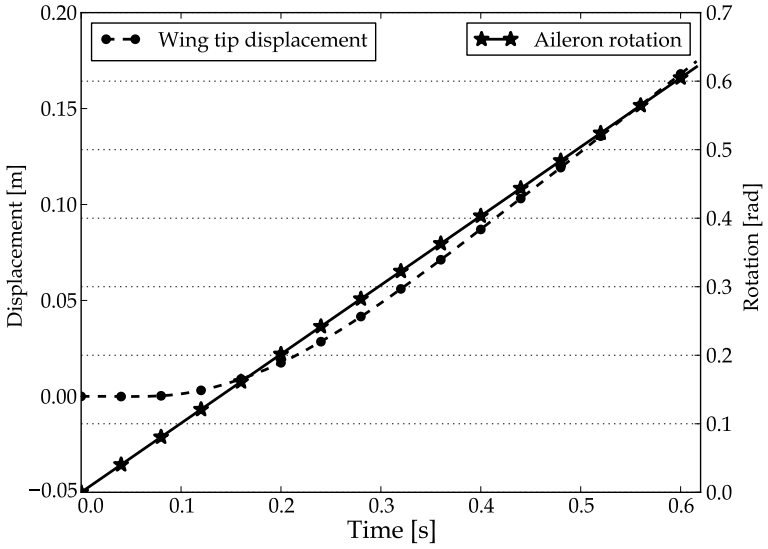

Figure 6.2: Characteristic behaviour simulation performed to generate input- and output-data

The curves of figure 6.2 are then used in generating the state-space model. The ailerons' rotational DOF was used as the input-data whereas the wing tip displacement was used as the output-data.

The sets of data were imported into Matlab where a data object was created to encapsulate the input- and output-data, using the *iddata* command. This data object was transferred to the System identification toolbox before choosing an order for the model. A second order model was used as this yielded a 98.09% fit to the estimation compared to a first-order and third order model which yielded a 94.56% and 90.44% fit to the estimation data, respectively.

$$\mathbf{F} = \begin{bmatrix} -0.495388032094521 & -0.245403183489207 \\ 0.029835235514845 & 0.977820603959600 \end{bmatrix}$$

$$\mathbf{G} = \begin{bmatrix} -1.3251854992698e+03 \\ 2.587471279129196e+01 \end{bmatrix}$$

$$\mathbf{H} = \begin{bmatrix} -0.001971625499639 & -0.110022889683153 \end{bmatrix}$$

Equation 6.6 was solved using the *dare* command in Matlab. Substitution of $\mathbf{P}$ into equation 6.5 was performed to compute the LQ controller gain. Lastly, The estimator gain ($\mathbf{L}$) was computed using the *kalman* command.

$$\mathbf{K}_{Gain} = \begin{bmatrix} 0.0003738 & 0.0001839 \end{bmatrix} \quad \mathbf{L} = \begin{bmatrix} -225.9966 \\ -14.6585 \end{bmatrix}$$

6.3 APDL scripting

ANSYS Parametric Design Language (APDL) is a scripting language that allows the user to parameterize models and automate tasks in ANSYS. Using commands, this scripting language allows the user to access the preprocessor and post-processor phase of the simulation. Logging into the preprocessor allows for the creation and/or altering of the FE model while logging into the post-processor allows for the retrieval of results from the FE model [46]. APDL scripting could therefore be used to embed the LQ controller within the FSI model which altered the original process of the FSI, as stated in section 2.6. Figure 6.3 shows the modified flow chart of the FSI process once the controller was embedded.

This flow chart describes when the modified FSI process calculated a new state-estimate and input-signal before updating the FE model. The FSI process solves both the FE and CFD models however, once the simulation reached the end of a time-step, a new state-estimate and input-signal were computed. The simulation then entered the following time-step and updated the FE model by compensating the ailerons' rotational DOF with the controller's input-signal. The simulation follows the original logic of solving the FE and CFD models and the process is repeated until the final time-step is reached and the simulation ends.

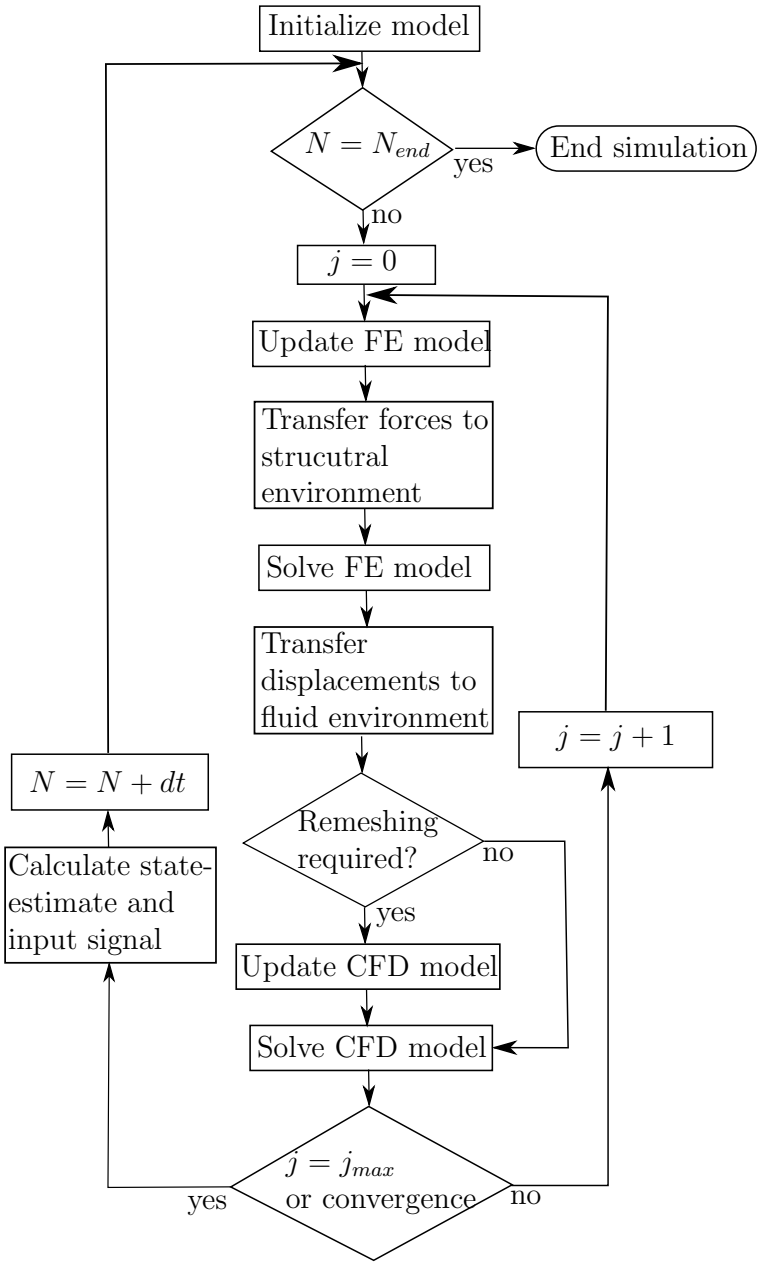

Figure 6.3: Modified FSI process with controller

Appendix C documents the APDL scripting used in the project. To better explain the APDL scripting and its logic, table 6.1 lists the lines of coding with their description (in accordance with Appendix C).

Table 6.1: APDL scripting logic

Line(s)	Description
8	The simulation enters the preprocessor
9-49	Define the state-space model used by the controller
51-55	The input-signal used to compensate the aileron's rotational DOF is computed using equation 6.3
62-72	The input signal for each aileron are defined
75-130	Update the FE model
79-85	Illustrates how Aileron1 was selected, switched to its local co-ordinate system and altered the rotational DOF with its respective input-signal
127	Simulation exits the preprocessor. The simulation continues to solve the FE model and CFD model for the current time-step
141	The simulation enters the post-processor
151-161	The state-estimate is computed using equation 6.2 and used in the following time-step
162-163	The input-signal is computed using equation 6.3 and used in the following time-step
185	The simulation enters the post-processor. This process is repeated again in the following time-step by updating the FE model, solving the FE and CFD models and calculating a new state-estimate and input-signal

Chapter 7

FSI simulation

The following chapter documents the results of the FSI simulations. Initial simulations were performed to determine whether aeroelastic instability was encountered. The findings of the initial simulations are discussed before a refined FSI model is presented. A sensitivity analysis of the FSI model, with regards to the time-step used, was performed before performing the simulations for the refined FSI model. The FSI model was then used in performing an open-loop simulation before applying the LQ controller in the closed-loop simulation.

7.1 Initial FSI model

The following details the initial simulations performed using the fine mesh for the FE and CFD models, as stated in sections 4.2 and 5.2 respectively. The initial simulations used the translational base excitation mentioned in section 4. Figure 7.1 depicts the initial FSI simulations performed with varying speeds used for the air velocity. Speeds of 50, 60 and 70 m/s were used in the 3 simulations. The curves generated indicate that the wing tip was observed to exhibit a stable oscillation. In addition, an increase in speed yielded a smaller wing tip displacement. This trend was evident in two instances. Firstly, the progressive increase in velocity amongst the 3 simulations displayed a corresponding smaller wing tip amplitude. Secondly, all 3 curves initially began with a larger oscillation before subsiding to a stable oscillation. This could be attributed to the velocity being ramped up to reach its maximum magnitude after 1 s.

To illustrate the effect of ramping the air velocity more clearly, the simulations of figure 7.1 were repeated. However, in this instance ramping of the velocity was prolonged. In each simulation the air velocity began with a value of 0 m/s and was increased to its maximum value at a time of 5 s. Figure 7.2 depicts the curves generated when the ramping of the air velocity was prolonged.

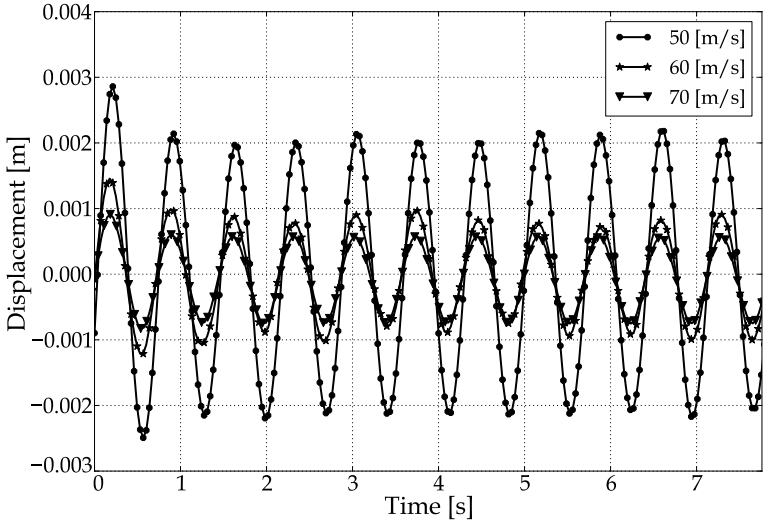

Figure 7.1: Wing tip displacement of the initial simulations

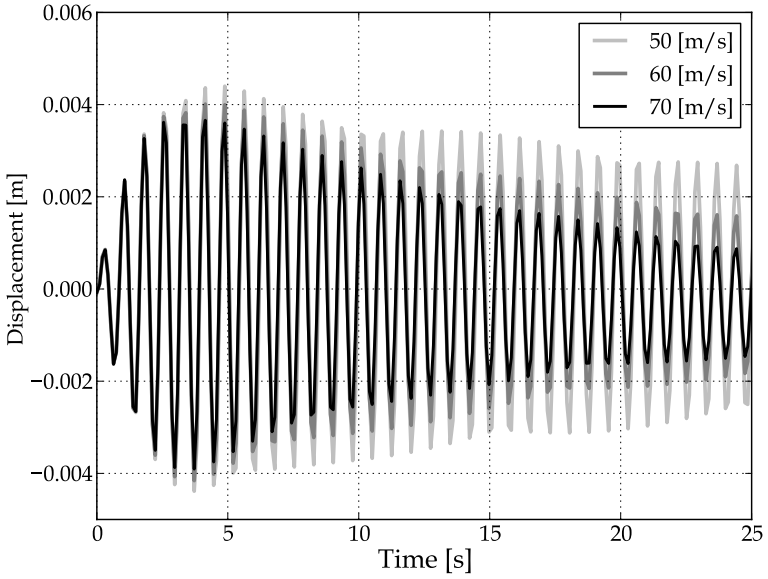

Figure 7.2: Prolonged ramping of the air velocity

The wing tip displacement was observed to decrease as the velocity of the air increased. These curves indicate that the aerodynamic damping of the system increased with an increase in air velocity and that the system became progressively more stable as the wing tip oscillation was observed to decrease. Aeroelastic instability was therefore not induced using this approach. According to theory, stated in section 1.1, disturbing the wing from its resting position is necessary to excite aeroelastic instability. The disturbance from the base excitation was therefore deemed inadequate to induce aeroelastic instability.

The air velocity was further increased to 85 m/s. In this instance, the wing tip was observed to follow an erratic vibration before generating negative cell volumes in the CFD model. Figure 7.3 depicts the curve generated using a velocity of 85 m/s. This figure indicates that aeroelastic instability was not encountered at speeds of 50, 60 and 70 m/s. However, at 85 m/s the wing tip was observed to experience erratic vibration before the simulation terminated (this irregularity is further investigated in section 7.3).

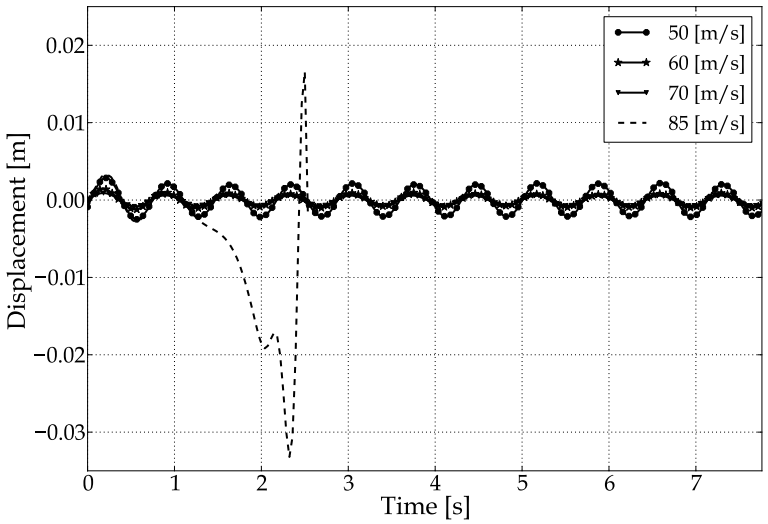

Figure 7.3: Erratic wing tip vibration at 85 m/s

According to the definition of classical flutter, stated in section 2.3.1, the flutter mechanism may involve the coupling of a bending and torsional mode. It was therefore concluded that, for the structure used in this project, the translational base excitation was not adequate in exciting flutter. The base excitation was therefore modified to a rotational base excitation, shown in figure 7.4 (using equation 7.1).

This modification would allow the structure to endure bending and torsion. The simulation was then performed again using the rotational base excitation at 50 m/s. Figure 7.5 depicts the wing tip displacement which was, in this instance, observed to increase progressively throughout the span of the simulation. The magnitude of wing displacement was also observed to be much larger compared to values from the previous simulations.

$$y(t) = 0.01 \sin(2\pi(1.409)t) \tag{7.1}$$

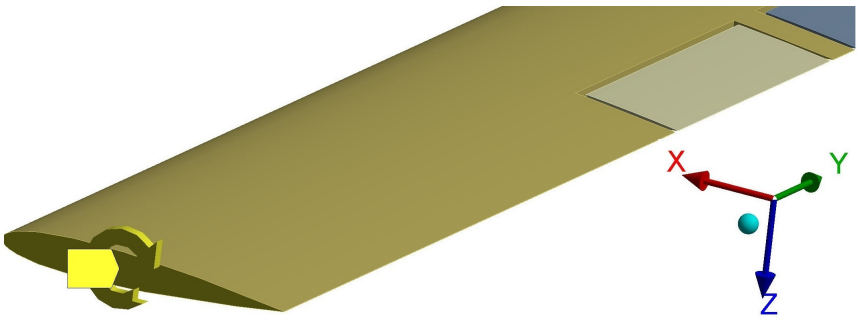

Figure 7.4: The rotational base excitation applied at the base of the wing

Figure 7.5 is an indication that aeroelastic instability was encountered as the wing tip displacement was observed to grow without bound. A study into the pressure distribution was performed to illustrate the rotational base excitation's ability to excite flutter.

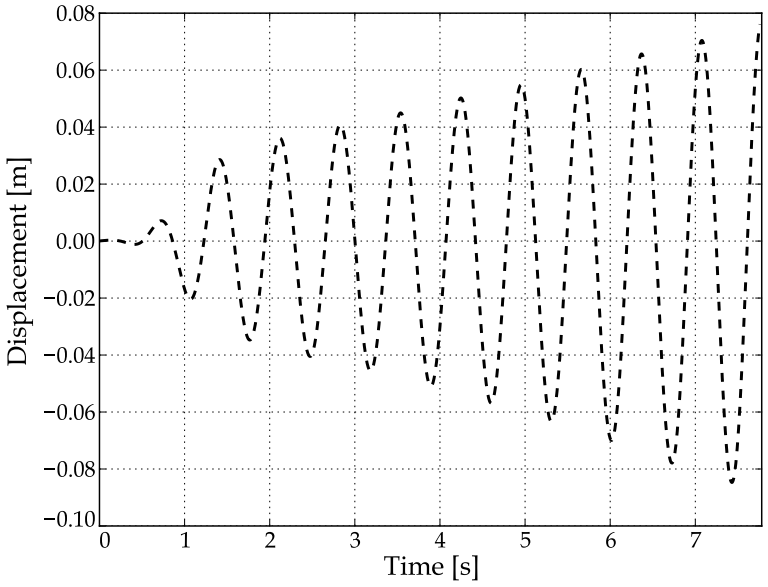

Figure 7.5: Initial simulation using the rotational base excitation at 50 m/s

Figures 7.6a and 7.6b depict the pressure plots of the aerofoil, at the wing tip, using the translational base excitation and the rotational base excitation respectively. As expected, figure 7.6a indicated that the stagnation point was located at the leading edge of the aerofoil. Symmetry of the pressure distribution was also observed about the chord line of the aerofoil, parallel with the x-axis. In the case of figure 7.6b, the stagnation point was observed to shift slightly. Symmetry of pressure distribution was not observed. A shift in stagnation point indicates that the effective angle of attack of the wing was altered.

The translational base excitation was not adequate in disturbing the structure,

whereas the rotational base was. Altering the wing's effective angle of attack subsequently allowed the structure to experience a torsional mode. Coupled with the bending mode, this bending-torsional mode was required to induce flutter.

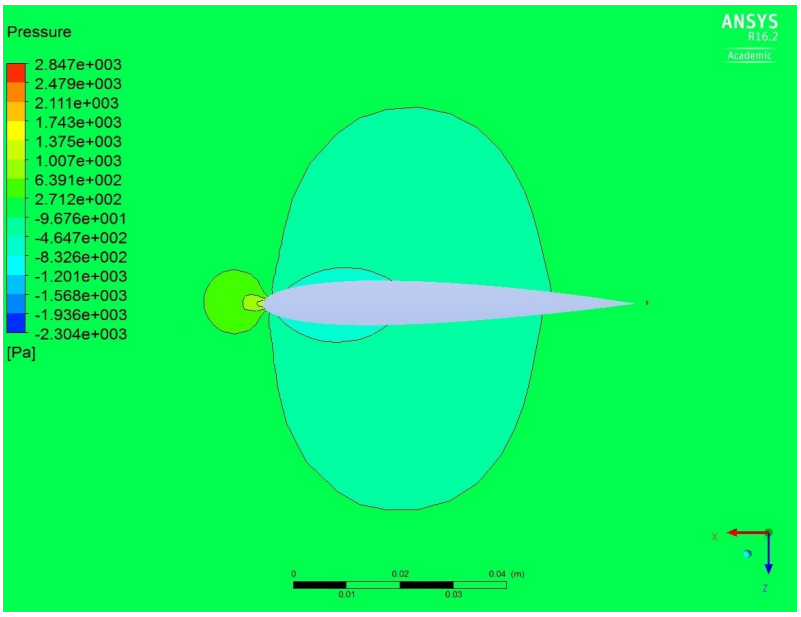

(a)

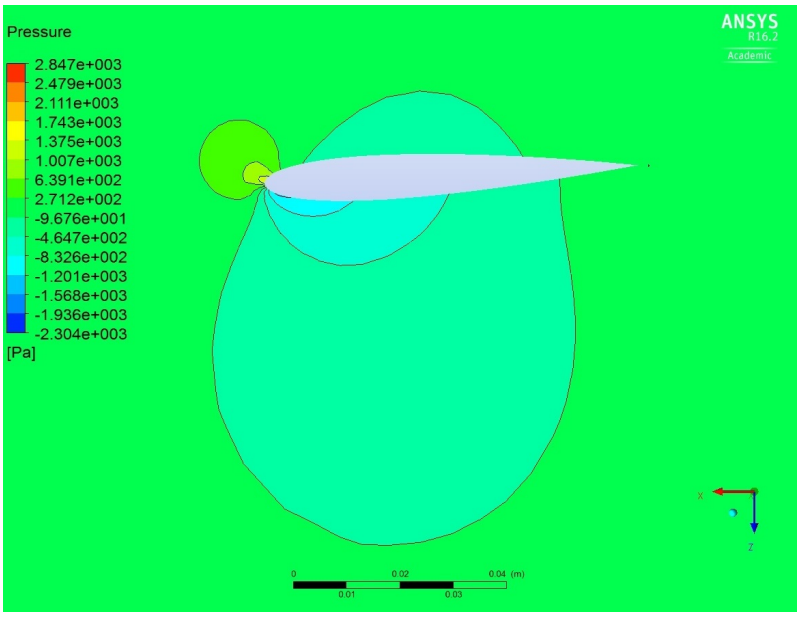

(b)

Figure 7.6: Pressure distribution of the aerofoil at the wing tip using the (a) translational and (b) rotational base excitation

Despite using a rotational base excitation, the resulting dominant displacement mode observed was the bending mode, shown in figures 7.7a and 7.7b. This bending mode is identical to the first natural mode observed in the modal analysis, performed in section 4.3.

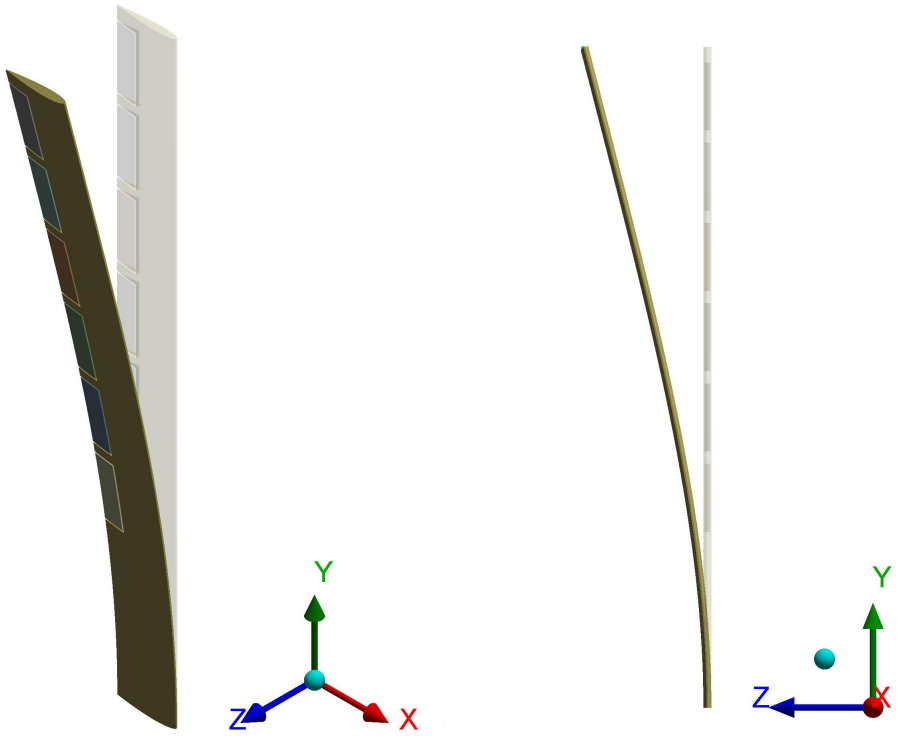

(a) (b)

Figure 7.7: Dominant mode

7.2 Time-step sensitivity

Using the staggered-approach required the FE and CFD solvers to use the same time-step value. This integration time-step influences the accuracy of the transient dynamic solution. Using a time-step that is too large induces errors that affect the response of the numerical model. Using too small a value grossly increases the computational effort. This is due to the fact that the time-step influences the total number of stagger-iterations performed in the entire span of the simulation and the subsequent CFD sub-iterations performed per stagger-iteration. ANSYS Inc (2012) recommends using a time-step which satisfies equation 7.2. This constraint ensures that 20 sampling points are taken per cyclic oscillation, to resolve the motion of the structure.

The motion of the structure can be thought of as the superposition of its natural modes. Therefore, the time-step size was chosen such that the highest mode (which contributed to the structure's response) could be resolved.

$$\Delta t < \frac{1}{20 \times f} \tag{7.2}$$

Using equation 7.2 to generate an initial value, a time-step of 0.0354 s was used in the initial simulation. Negative cell-volumes were encountered using this time-step. This error is an indication that the moving boundary in the CFD model has deformed the CFD mesh to the extent that certain elements have become highly distorted or twisted. One way of resolving this issue would be to decrease the time-step to allow remeshing to occur at a more frequent rate. A time-step sensitivity test was performed to determine when the time-step was small enough to resolve the negative cell volumes.

Figure 7.8 depicts the curves generated, of the wing tip, using values of 0.016 s, 0.008 s, 0.004 s and 0.002 s for the time-step. In this instance, negative cell volumes were encountered using a time-step of 0.016 s before the simulation terminated at 1.7 s. Negative cell volumes were not encountered using time-steps of 0.008 s, 0.004 s and 0.002 s as the simulations proceeded to complete at 8 s, shown in figure 7.9.

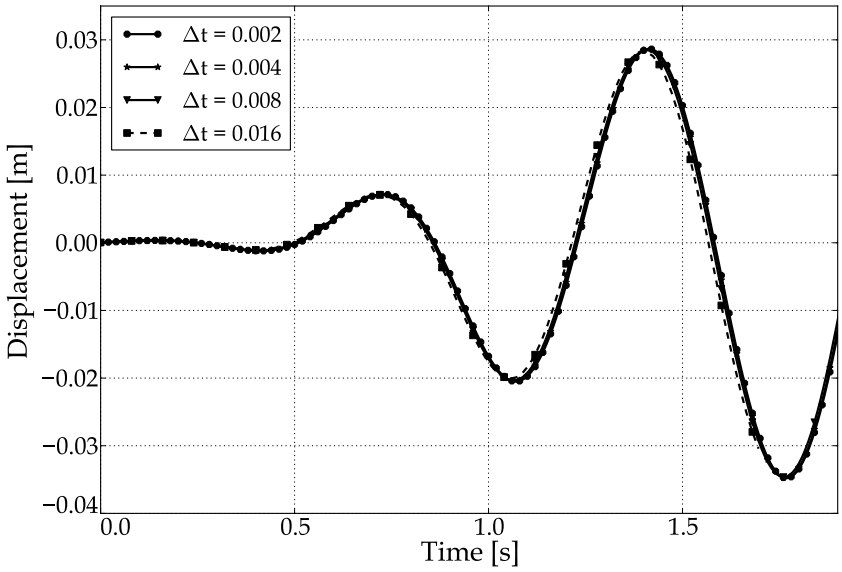

Figure 7.8: Time-step sensitivity test

Despite encountering negative cell volumes using a time-step of 0.016 s, figure 7.8 shows that the curve was coincident with the curves using smaller values for the time-step. This indicates that the sensitivity of the FSI model, with regards to the time-step, solely influenced the remeshing scheme's ability to circumvent distorted elements.

Figure 7.9 illustrates that no lag or lead trends were observed amongst the curves using time-step values of 0.008 s, 0.004 s, and 0.002 s. As a result, it was decided to use a time-step of 0.008 s since it was small enough to circumvent negative cell volumes and large enough to avoid wasting computational resources.

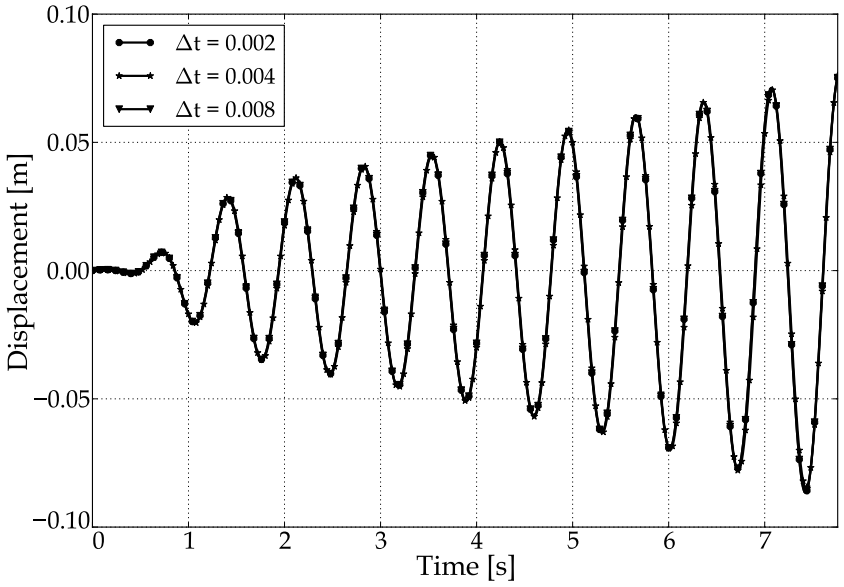

Figure 7.9: Complete simulation of the time-step sensitivity test

7.3 Refined FSI model

Following the results of the initial simulations, the refined FSI model was constructed. Once again, the fine meshes for the FE and CFD models were selected, as stated in sections 4.2 and 5.2. The rotational base excitation replaced the translational base excitation. A time-step of 0.008 s was used for both the FE and CFD solvers. Other refinements included a stagger-iteration sensitivity test. This process, documented in Appendix D, led to the conclusion that 3 stagger-iterations per time-step would be sufficient for the refined FSI model. The CFD model was also refined to ensure that the y^+ values of the FSI interface in the CFD model, were within the appropriate region. This process is documented in Appendix B.

7.3.1 Classical flutter

The open-loop simulation follows the original FSI process, previously described in figure 2.9. The closed-loop simulation was then performed by using the modified FSI process, previously described in figure 6.3.

Figures 7.10, 7.11 and 7.12 represent the wing's tip displacement, velocity and acceleration during the open- and closed-loop simulations at 50 m/s. The wing tip displacement, velocity and acceleration were observed to progressively increase in amplitude during the open-loop simulation. The curves of the open-loop simulation indicate that the structural damping was inadequate to dissipate the energy being fed into the system by the air. Therefore, it was concluded that aeroelastic instability was encountered which resulted in the unstable vibration witnessed in these simulations. Also, large wing tip deflections were observed in the open-loop simulations. This could be attributed to the high aspect-ratio of the wing. However, the fluid domain was large enough to model the structure's deformation.

The curves generated from the closed-loop simulation depict the structure following a stable oscillation at a lower amplitude. In this instance, the wing tip displacement initially began to increase before reaching a point where the displacements were observed to vibrate about a constant amplitude. The closed-loop simulation illustrated the LQ controller's capability to suppress flutter using existing control surfaces as the unstable and progressive trend of the wing's tip displacement, velocity and acceleration were all subdued. This indicates that controlled use of the ailerons increased the aerodynamic damping of the system, thereby aiding in dissipating energy being fed into the system.

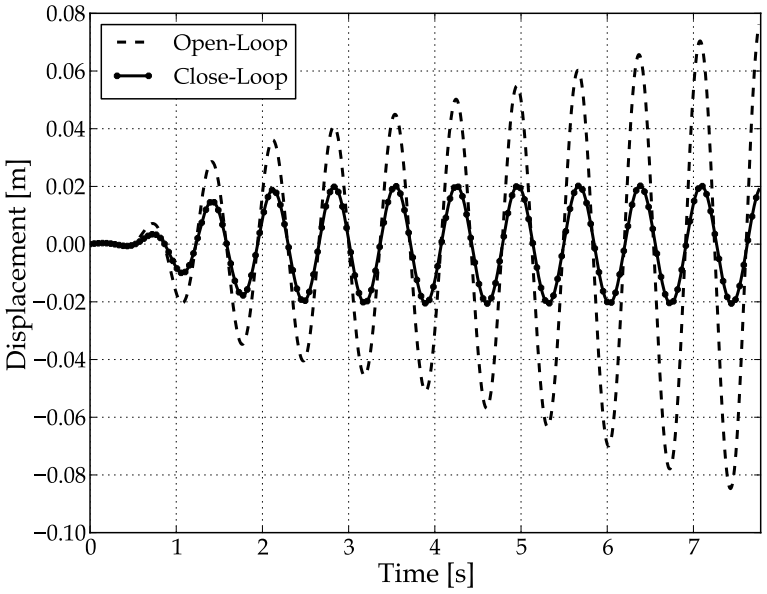

Figure 7.10: Wing tip displacement at 50 m/s

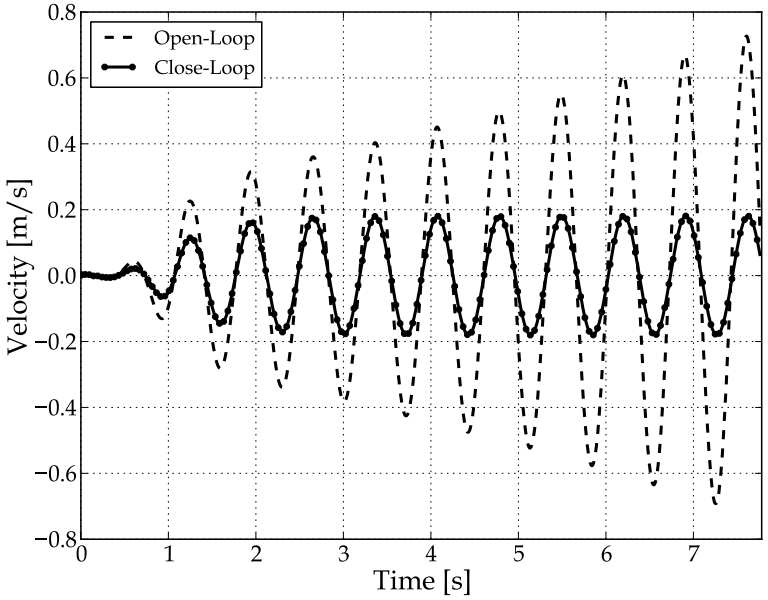

Figure 7.11: Wing tip velocity at 50 m/s

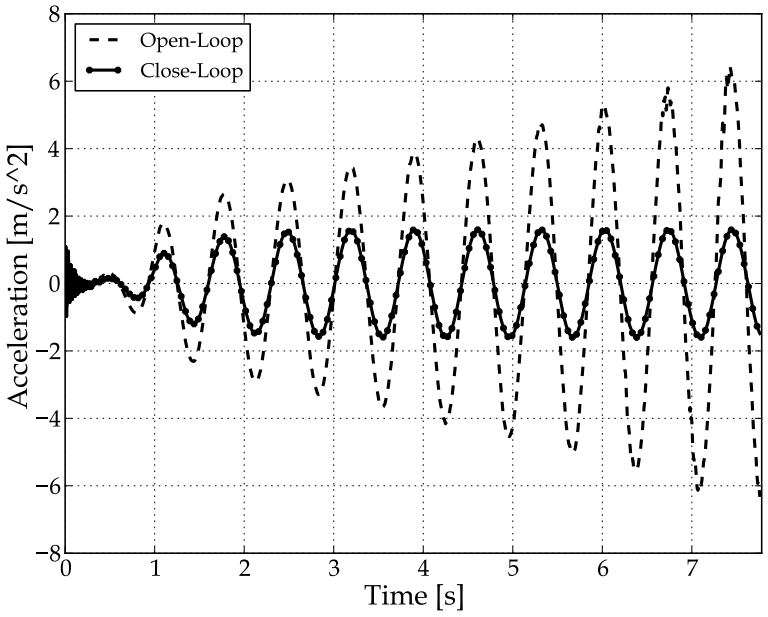

Figure 7.12: Wing tip acceleration at 50 m/s

7.3.2 Non-classical flutter

Increasing the air velocity to 70 m/s generated erratic wing tip vibration. The curve generated, using this open-loop simulation, is shown in figure 7.13. Erratic wing tip vibration was previously also witnessed using the translational base excitation in figure 7.3. This irregularity was further investigated to ensure that the erratic vibration was not a product of numerical instability. The following section details the study into the wall shear stress and swirling strength at air velocities of 50 m/s and 70 m/s.

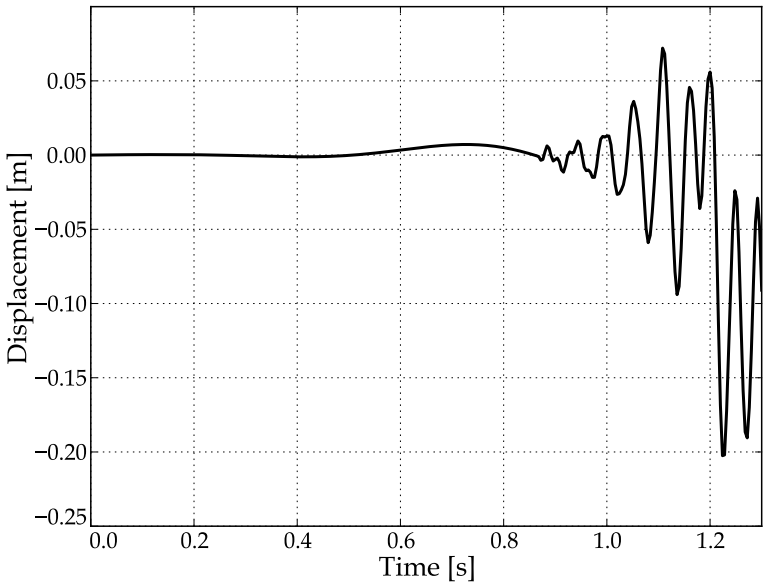

Figure 7.13: Erratic wing tip vibration at 70 m/s

An adverse pressure gradient may induce flow separation. The separation point occurs when the velocity, near the wing, retards to the extent that the wall shear stress reaches a value of 0. From this separation point, the wall shear stress becomes negative and the flow reverses, causing the fluid to detach from the surface. The wall shear stress across the wing was investigated in order to determine whether flow separation occurred.

Figure 7.14 depicts the wall shear stress plot across the structure at 50 m/s. A fluid's inability to adapt to changes in velocity, caused by changes of the surface's profile or contour, may cause the fluid to detach itself from the surface. Flow separation would therefore be expected to occur towards the trailing edge of the wing. However, no low wall shear stress regions were observed at 50 m/s.

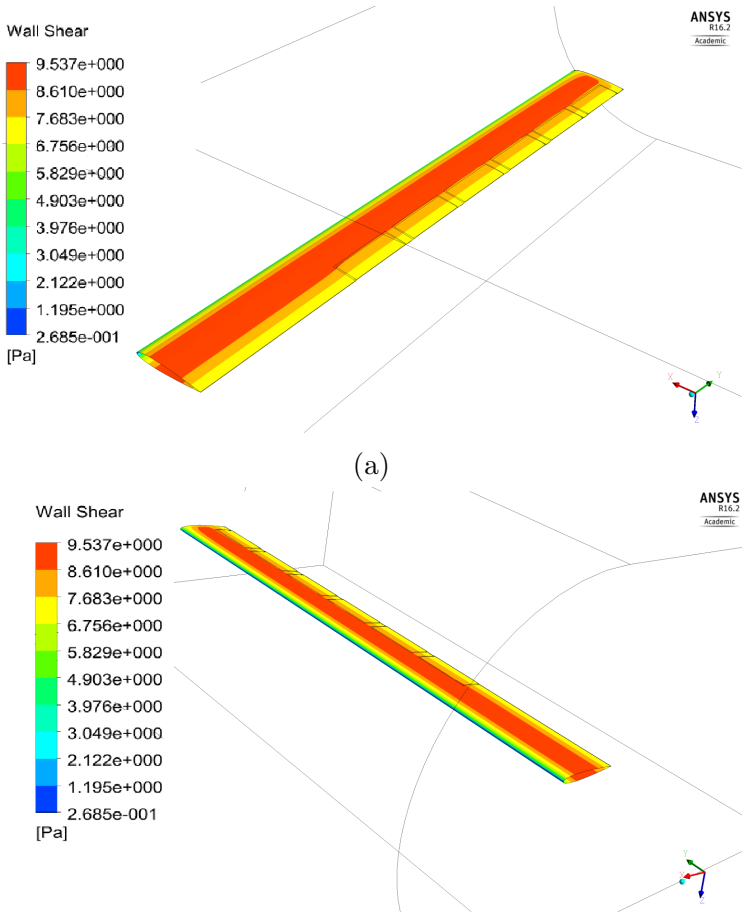

Figure 7.14: Wall shear stress plot of the wing surface at 50 m/s

Vortices may form from the regions of recirculating flow. Vortices are circular or spiral sets of streamlines. In ANSYS, a swirling strength plot represents the strength of swirling motion around local centres. Since turbulent flow is expected, a swirling strength plot of the fluid domain was performed to determine whether significant formation of vortices were present [39].

Figure 7.15 depicts the swirling strength at a speed of 50 m/s. Negligible presence of vortices were observed. Figure 7.15b indicates that formation of vortices existed at the wing tip however, this was attributed to the pressure difference across the wing tip. The superpositioning of the swirling strength and wall shear stress is shown in figure 7.16.

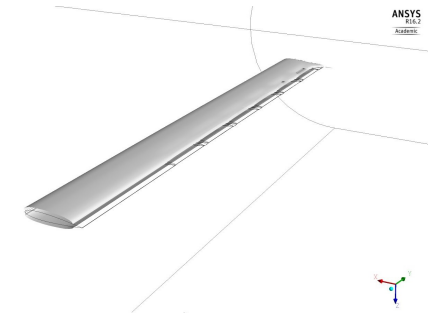

(a)

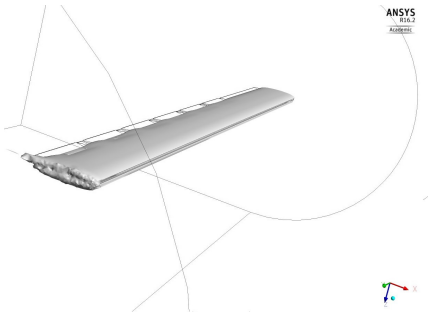

(b)

Figure 7.15: Swirling strength plot at 50 m/s

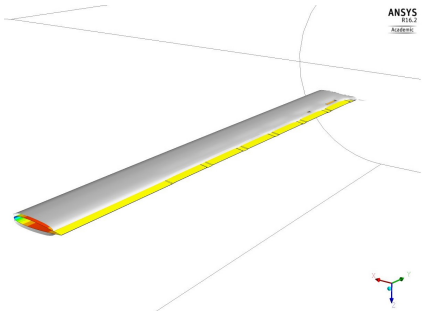

(a)

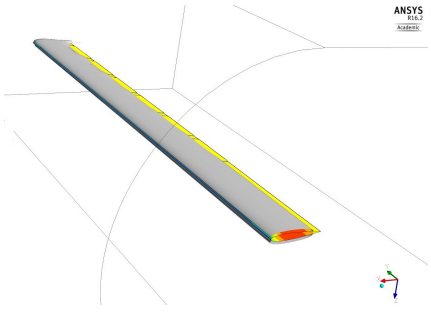

(b)

Figure 7.16: Wall shear stress and swirling strength plot at 50 m/s

Figures 7.17 depicts the wall shear stress plot of the wing surface at a speed of 70 m/s. Unlike the wall shear stress at 50 m/s, low values of wall shear stress were observed at the trailing edge of the wing. A minimum value of -0.0775 Pa was observed which implies that the flow reversed near the trailing edge of the wing.

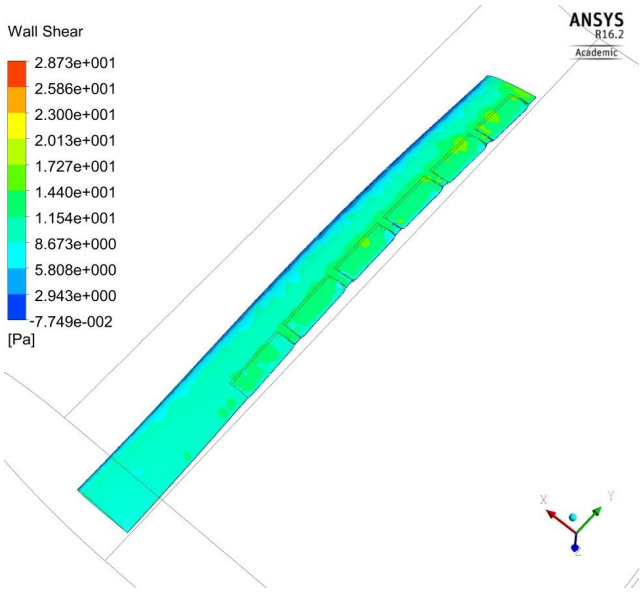

(a) Top view

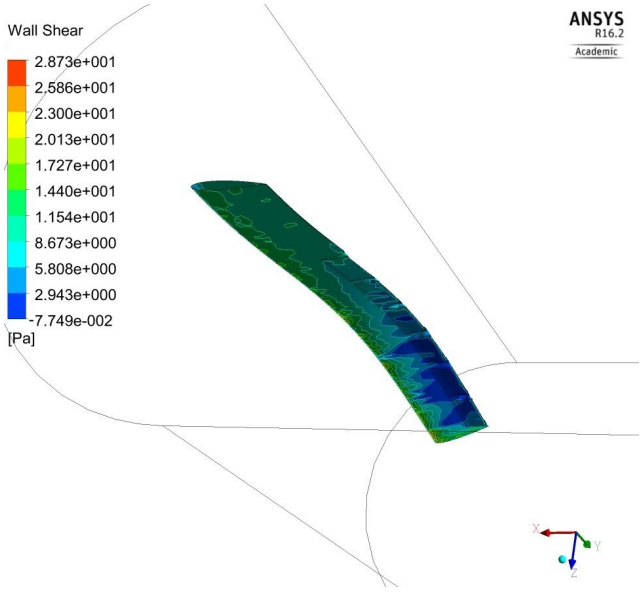

(b) Bottom view

Figure 7.17: Wall shear stress plot of the wing surface at 70 m/s

The swirling plots were also generated for the simulation at 70 m/s. In this instance, figure 7.18 indicates that significant formation of vortices were observed when the air velocity was increased to 70 m/s.

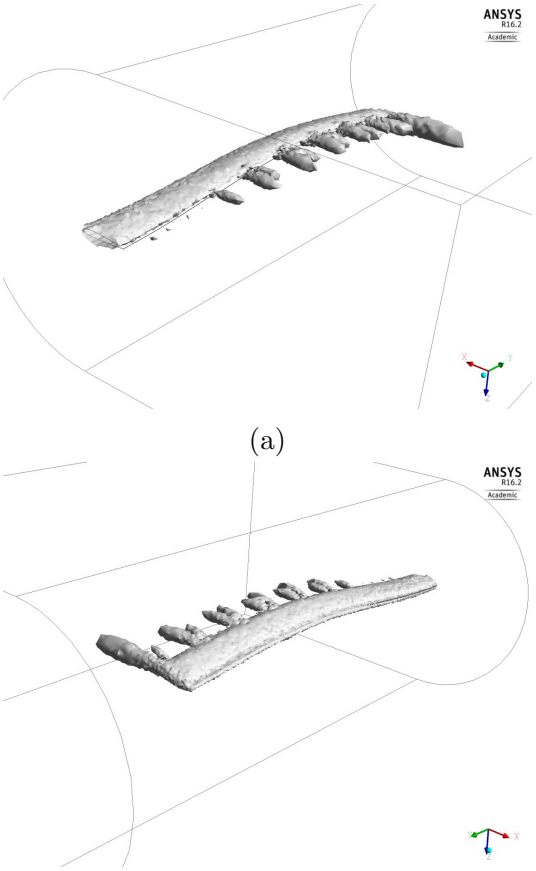

(a)

(b)

Figure 7.18: Swirling strength plot at 70 m/s

A top view of the swirling strength plot, shown in figure 7.19, revealed that the vortices were observed to be present in the region where the ailerons were located. These vortex regions formed at the adjacent areas between the wing and the ailerons. The superpositioning of the swirling strength and wall shear stress is shown in figure 7.20 where significant formation of the swirling strength was observed to coincide with areas where low shear stress values were observed.

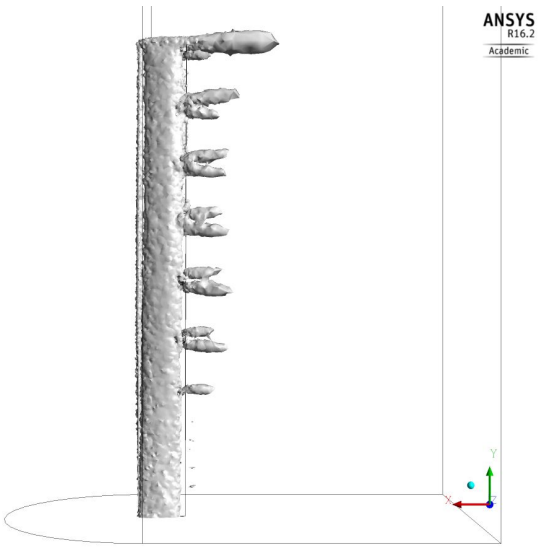

Figure 7.19: Vortices formation at wing-aileron regions at 70 m/s

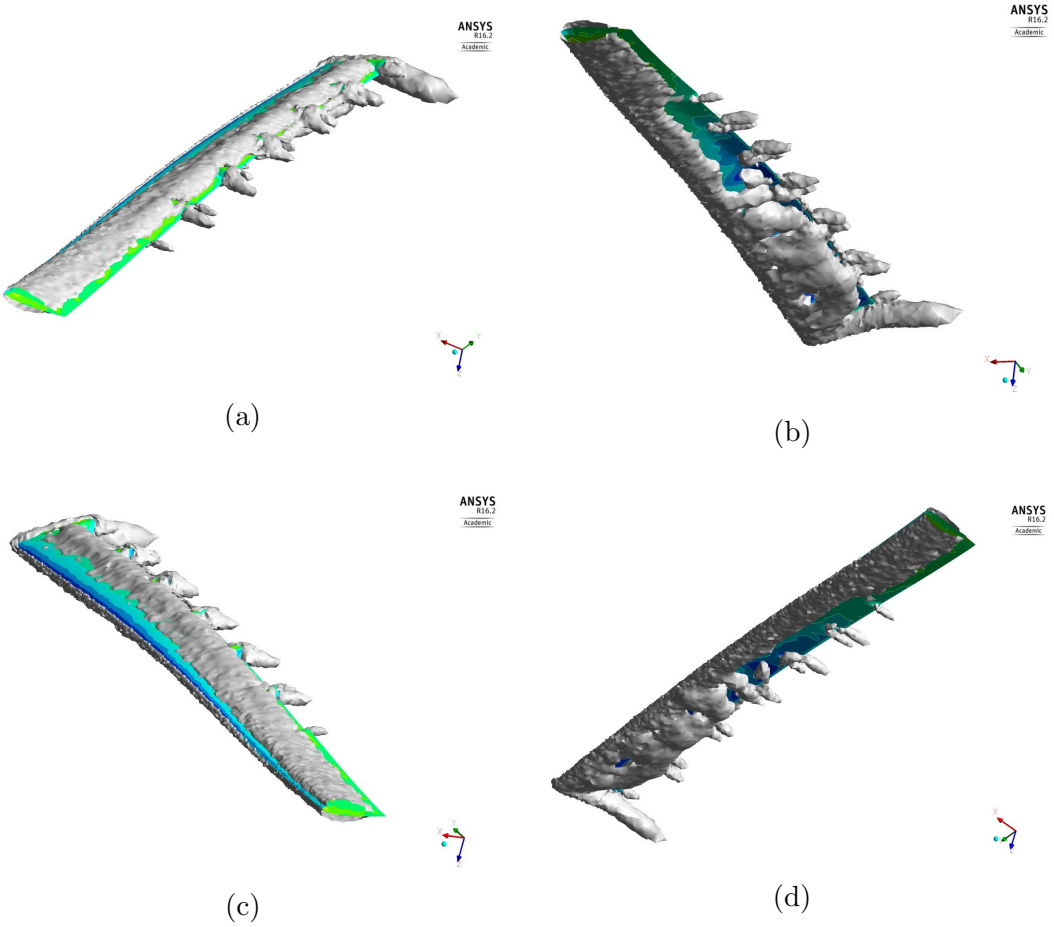

Figure 7.20: Significant vortex formation at low wall shear stress regions

The wall shear stress and swirling strength plots indicated that flow reversal did not occur at 50 m/s and no significant presence of vortices was observed. However, at 70 m/s the wall shear stress plot displayed regions where the wall shear stress reached values below zero. This is an indication that fluid flow reversed and detached from the surface. Significant formation of vortices were observed at 70 m/s. These vortex regions formed near the adjacent areas of the wing and ailerons. In addition, areas of low wall shear stress coincided with the regions where significant vortices were present. It was therefore concluded that flow separation occurred at an air velocity of 70 m/s but not at 50 m/s.

According to section 2.3.1, classical flutter requires the flow to be attached to the wing. The erratic vibration, observed in figure 7.13, could possibly be attributed to non-classical flutter. A close-loop simulation was therefore not performed at 70 m/s as non-classical flutter was deemed beyond the scope for this project. However, suppression of classical flutter at 50 m/s was achieved.

Chapter 8

Conclusion and recommendations

The design and evaluation of a flutter-suppression control system has been documented in this study. All objectives set out in section 1.2 were achieved. The following chapter summarizes the results of the project and concludes with recommendations for future work.

8.1 Structural environment

A structural and fluid environment was established in ANSYS which constitutes a numerical FSI model. Assuming the structure as solid bodies generated a wing which was too rigid. As a result, the wing's bending stiffness was altered to compensate for its increased rigidity. Since control surfaces were used in suppressing flutter, the ailerons' DOF were constrained to the extent that they could not contribute to the flutter mechanism. The modal analysis indicated that bending modes were dominant amongst those generated. This was attributed to the geometry of the high-aspect-ratio wing. A base excitation was used in exciting the first bending mode at its excitation frequency.

8.2 Fluid environment

The discretized fluid domain made use of hexahedral elements at particular sections of the CFD model. Using the spring-based remeshing scheme proved inadequate in remeshing the deforming fluid domain as this scheme is not ideal for fluid zones where non-tetrahedral elements are used. The diffusion-based remeshing scheme was therefore used which proved to be successful in remeshing the fluid domain. It must be noted that this remeshing scheme is computationally more intensive than its counterpart nonetheless, it proved sufficient for the project.

Large wing tip deflections were observed during the open-loop simulations. This could be attributed to the nature of the high aspect-ratio of the wing. However, the geometry of the fluid domain was adequate in capturing the deformation of the structure for this project.

8.3 Control system

A LQ controller was used in suppressing flutter. Constructing a full-order model of the system required a means of generating the state-space model of the FSI. The state-space model was generated using Matlab's System Identification toolbox. This method required a set of input- and output-data of the FSI model. These data sets were obtained by performing a characteristic behaviour simulation in which the ailerons' rotational DOF were forced to rotate with a desired input-signal, which resulted in a subsequent output displacement of the wing. The state-space model was then generated and embedded within the FSI model using APDL scripting.

8.4 Initial FSI model

Simulations performed on the initial FSI model indicated that a progressive increase in air velocity decreased the wing tip displacement and therefore, yielded a progressively stable vibration of the strucutre. As a result, the translational base excitation was deemed inadequate for the project as it could not excite flutter. However, aeroelastic instability was encountered when a rotational base excitation was used. Investigation of the pressure distribution at the wing tip revealed that altering the wing's effective angle of attack was required to induce aeroelastic instability.

8.5 Refined FSI model

Results of the initial simulations were used in constructing a refined FSI model. Open- and closed-loop simulations were performed to determine whether the LQ controller was capable of suppressing flutter. The controller regulated the wing tip displacement and suppressed the vibration experienced by the wing with the use of the ailerons. Open-loop simulations at 50 m/s revealed that aeroelastic instability existed as the wing tip displacement was observed to increase without bound. Closed-loop simulations were then performed which illustrated the controller's capacity to successfully subdue the unstable vibration by increasing the aerodynamic damping of the system.

At a velocity of 70 m/s, the wing-tip displacement was observed to follow an erratic vibration compared to the vibration at a velocity of 50 m/s.

An investigation into the wall shear stress and swirling strength led to the conclusion that flow separation occurred at 70 m/s but not at 50 m/s. In addition, significant vortex formations were observed at 70 m/s.

According to theory, classical flutter requires the flow to be attached to the wing. Therefore, classical flutter was encountered at 50 m/s and non-classical flutter at 70 m/s. A closed-loop simulation was not performed at 70 m/s as non-classical flutter was deemed beyond the scope of the project.

8.6 Recommendations

- Future studies should consider the large and highly non-linear deformations of high-aspect-ratio wings. Construction of the CFD model should ensure that the fluid domain is large enough, to the extent that the wing's deformation can be modelled.
- Use of modern control theory and the framework for the APDL scripting allows for the expansion of the control system to a MIMO control law in numerical modelling. This would prove beneficial as the large wing deformation (due to high flexibility) would result in accompanying changes in the aerodynamic loading.
- The controller was capable in suppressing classical flutter however, suppression of non-classical flutter has yet to be performed. Future work could be performed to determine whether suppression of non-classical flutter is possible.
- The control surfaces' DOF were constrained to the extent that their DOF did not contribute to the flutter mechanism. Therefore, future work could be performed in which these constraints are not enforced.

Appendices

Appendix A

Wing and aileron specifications

A.1 Wing and aileron dimensions

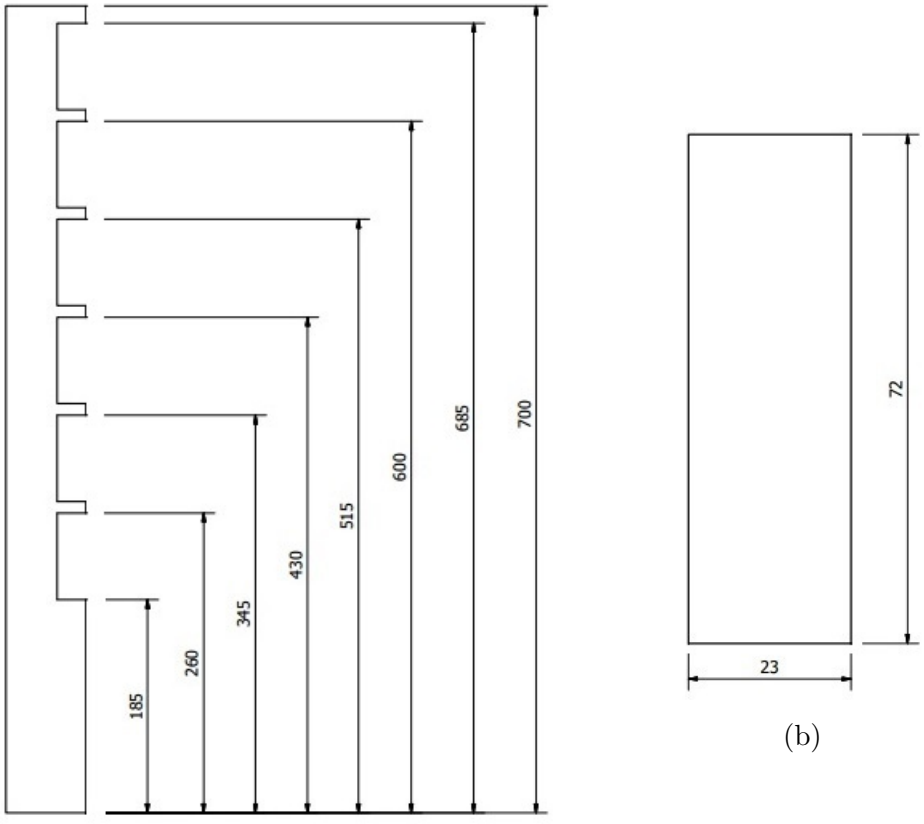

(a)

(b)

Figure A.1: Top view of the (a) wing and (b) aileron with relevant dimensions

A.2 Bending inertia of the aerofoil

The following details the method used in altering the wing's bending inertia. Section 4.1 states that the wing and ailerons were assumed to be solid bodies. The bending stiffness was therefore scaled to account for this assumption. Determining the wing's bending stiffness, shown by equation A.1, required the area (A) of the aerofoil, centroid axis (z_c) and area moment of inertia (I) to be computed. The area of the wing's aerofoil is expressed by equation A.2, the centroid axis is expressed by equation A.3 and the area moment of inertia by equation A.4 [10].

The parameters of the aforementioned equation are all based on the aerofoil diagram, shown in figure A.2, where the lower and upper surface distance of the aerofoil are represented by (Z_l) and (Z_u) respectively [10].

$$M = EI\kappa \tag{A.1}$$

$$A = \int_0^c [Z_u - Z_l]dx \tag{A.2}$$

$$z_c = \int_0^c \frac{1}{2A}[(Z_u)^2 - (Z_l)^2]dx \tag{A.3}$$

$$I = \int_0^c \frac{1}{3}[(Z_u - z_c)^3 - (Z_l - z_c)^3]dx \tag{A.4}$$

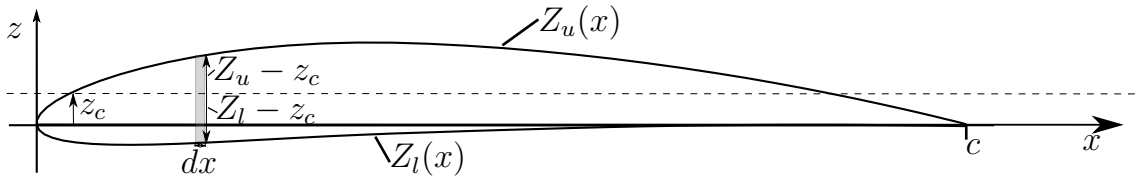

Figure A.2: Bending inertia of an aerofoil [10]

The centroid axis resulted in $z_c = 0$ due to the symmetric profile of the NACA 0012 aerofoil. Equation A.4 simplifies to equation A.5 which can then be solved using either using Z_l or Z_u.

The area moment of inertia, for this work, was computed and is shown in equation A.5. The default value of the Young's modulus for the aluminium alloy used was set at 7.1×10^{10} Nm^2. Using equation A.1 and the default values, the bending stiffness was calculated as 1.154×10^{10} Nm^2.

The bending stiffness of very flexible wings range from 10^4 Nm^2 to 10^6 Nm^2 [48] [49]. Although a very flexible wing was not required, the Young's modulus was decreased to avoid generating an overly stiff wing. The Young's modulus was therefore decreased to 1×10^9 Nm^2, in the ANSYS material database. These values were used in the FSI simulations.

$$I = \int_0^c \frac{1}{3}[2(Z_u)^3]dx = 3.4574 \times 10^{-9} \text{ m}^4 \tag{A.5}$$

Appendix B

y^+ value contour plots

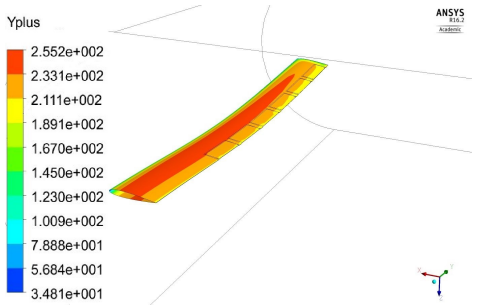

(a)

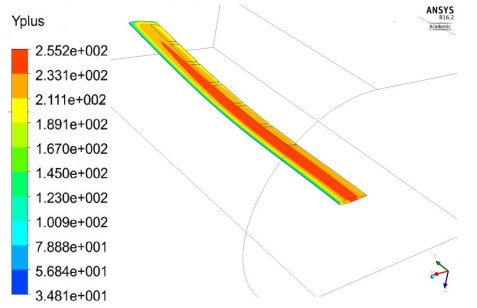

(b)

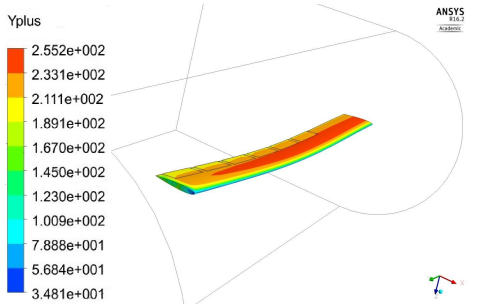

(c)

Figure B.1: y^+ value contour plots on the wing surface

Appendix C

APDL scripting

```
/batch
/solu
/gst,on,on
antype,4,rest,,,continue
finish

! ****** Begin /prep7 Command Snippet ******
/prep7
!*****************************************
!********* Begin State Space Models ********
!*****************************************
*DIM,DATAX,array,2,2
*VREAD,DATAX(1,1),MatrixX4,csv,,JIK,2,1
(1F50.8)

*MWRITE,DATAX,MatrixDATAX,csv,,JIK
%G, %G

*dim,x,array,2,1
x(1,1) = DATAX(1,1)
x(2,1) = DATAX(1,2)
*MWRITE,x,MatrixXPre,csv,,JIK
%G

*DIM,F,array,2,2
F(1,1)= -0.495388032094521
F(1,2)= -0.245403183489207
F(2,1)= 0.029835235514845
F(2,2)= 0.977820603959600
```

```
30
31 *DIM,G,array,2,1
32 G(1,1)= -1325.1854992698e
33 G(2,1)= 25.87471279129196e
34
35 *DIM,C,array,1,2
36 C(1,1)= -0.001971625499639
37 C(1,2)= -0.110022889683153
38
39 *DIM,K,array,1,2
40 K(1,1)= 0.0003738
41 K(1,2)= 0.0001839
42
43 *DIM,L,array,2,1
44 L(1,1)= -225.9966
45 L(2,1)= -14.6585
46
47 !*****************************************
48 !********** End State Space Models *********
49 !*****************************************
50
51 *DIM,DATAU,array,2,2
52 *VREAD,DATAU(1,1),Matrixut,csv,,JIK,2,1
53 (1F50.8)
54
55 GAIN = (DATAU(1,1))
56
57 *CFOPEN,'PreGAIN','txt'
58 *VWRITE,GAIN
59 %10.8f
60 *CFCLOS
61
62 Gain1 = 1*error                    ! Aileron1
63
64 Gain2 = 0.8*error                  ! Aileron2
65
66 Gain3 = 0.6*error                  ! Aileron3
67
68 Gain4 = 0.4*error                  ! Aileron4
69
70 Gain5 = 0.2*error                  ! Aileron5
71
72 Gain6 = 0.1*error                  ! Aileron6
73
```

```
74
75 !*****************************************
76 !****Start Update Aileron Rotation**********
77 !*****************************************
78
79 !AILERON1
80 csys,15
81 cmsel,s,Aileron1
82 !ngen,2,0,all,,,0,50
83 d,all, ROTY, Gain1
84 allsel,all
85 csys,0
86
87 !AILERON2
88 csys,15
89 cmsel,s,Aileron2
90 !ngen,2,0,all,,,0,50
91 d,all, ROTY, Gain2
92 allsel,all
93 csys,0
94
95 !AILERON3
96 csys,15
97 cmsel,s,Aileron3
98 !ngen,2,0,all,,,0,50
99 d,all, ROTY, Gain3
100 allsel,all
101 csys,0
102
103 !AILERON4
104 csys,15
105 cmsel,s,Aileron4
106 !ngen,2,0,all,,,0,50
107 d,all, ROTY, Gain4
108 allsel,all
109 csys,0
110
111 !AILERON5
112 csys,15
113 cmsel,s,Aileron5
114 !ngen,2,0,all,,,0,50
115 d,all, ROTY, Gain5
116 allsel,all
117 csys,0
```

```
118
119 !AILERON6
120 csys,15
121 cmsel,s,Aileron6
122 !ngen,2,0,all,,,0,50
123 d,all, ROTY, Gain6
124 allsel,all
125 csys,0
126
127 finish
128 !*********************************************
129 !******End Update Aileron Rotation**********
130 !*********************************************
131
132 ! ****** End /prep7 Command Snippet ******
133
134 /solu
135 solve
136 !save
137
138 !*********************************************
139 !******* Begin /Post1 Command Snippet ******
140 !*********************************************
141 /post1
142 *GET,basetip,node,15897,u,z
143 *GET,tip,node,15894,u,z
144
145 u = GAIN
146 *CFOPEN,'PostGAIN','txt'
147 *VWRITE,u
148 %10.8f
149 *CFOPEN
150
151 *MOPER,t1,F,MULT,x
152 *VFACT,u
153 *VFUN,t2,COPY,G
154 *MOPER,t3,H,MULT,x
155 t3(1,1) = tip - t3(1,1)
156 t3B = t3(1,1)
157
158 *VFACT, t3B
159 *VFUN,t4,COPY,M
160 *VOPER,t4,t2,ADD,t4
161 *VOPER,x,t1,ADD,t4
```

```
*MOPER, ut ,K,MULT, x
u = -ut(1,1)

*MWRITE, ut , Matrixut , csv , , JIK
(1F50.8)

*MWRITE, x , MatrixX4 , csv , , JIK
(1F50.8)

*DIM, val2 , array ,7 ,1
val2(1) = 3.2,u,3.2 , basetip ,3.2 ,5 ,3.2
*CFOPEN, 'Post ', 'csv '
*VWRITE, val2(1)
%10.8f
*CFCLOSE
!*********************************************
!******* End /Post1 Command Snippet ********
!*********************************************

!*********************************************
!****** Begin /Pos26  Command Snippet ******
!*********************************************
! Time history results
/post26
! Displacement
NSOL,5 ,15894 ,U, Z
STORE,MERGE
*GET, size , VARI, , NSETS
*dim , UX55, array , size
VGET, UX55(1) ,5
*CFOPEN, DIS , csv
*VWRITE, UX55(1)
(6x, f12 .8)
*CFCLOSE

! Velocity
NSOL,5 ,15894 , VEL, Z
STORE,MERGE
*GET, size , VARI, , NSETS
*dim , UX55, array , size
VGET, UX55(1) ,5
*CFOPEN, VEL, csv
*VWRITE, UX55(1)
(6x, f12 .8)
```

```
206 *CFCLOSE
207
208 ! Acceleration
209 NSOL,5,15894,ACC,Z
210 STORE,MERGE
211 *GET,size,VARI,,NSETS
212 *dim,UX55,array,size
213 VGET,UX55(1),5
214 *CFOPEN,ACC,csv
215 *VWRITE,UX55(1)
216 (6x,f12.8)
217 *CFCLOSE
218 !*********************************************
219 !******* End /Pos26 Command Snippet *******
220 !*********************************************
221 finish
222 /exit
```

Appendix D

Stagger-iteration sensitivity

The staggered approached, mentioned in section 2.6, requires sub-iterations to be performed during each time-step. In order to obtain a strongly-coupled staggered approach, the FE and CFD models were required to reach convergence before advancing the simulation to the following time-step. In order to determine whether a strongly-coupled staggered approach was achieved, simulations using 5, 3 and 1 stagger-iterations per time-step were performed. Figure D.1 depicts the 3 generated curves. The curves illustrate the sensitivity of the FSI simulation as the number of stagger-iterations were increased.

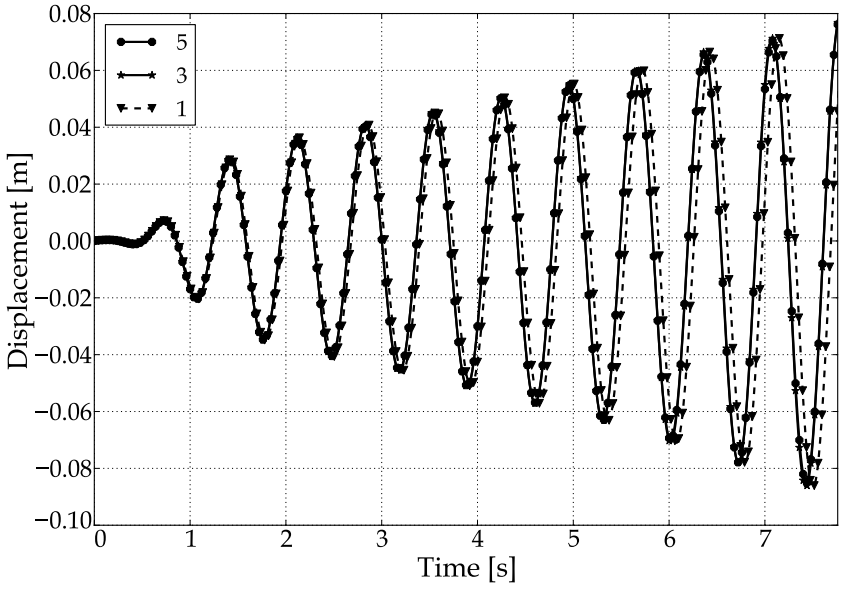

Figure D.1: Stagger-iteratation sensitivity test

The graph indicates that the simulation using 1 stagger-iteration, per time-step, lagged the simulations using 3 and 5 stagger-iterations. Using 1 stagger-iteration per time step is the minimum amount of what could have been performed and therefore represents a weakly-coupled staggered approach.

The lagging trend of the simulation using 1 stagger-iteration was therefore attributed to the lack of convergence in the FE and CFD models.

The simulations using 3 and 5 stagger-iterations yielded curves which were almost coincident. Figure D.2 shows an enlarged view of the previous graph, illustrating the negligible variation between using 3 and 5 stagger-iterations. A strongly-coupled staggered approach was therefore, achieved using 3 and 5 stagger-iterations per time-step. Increasing the number of stagger-iterations performed per time-step increased the computational effort required therefore the final FSI model made use of 3 stagger-iterations since the difference between the two curves were deemed negligible.

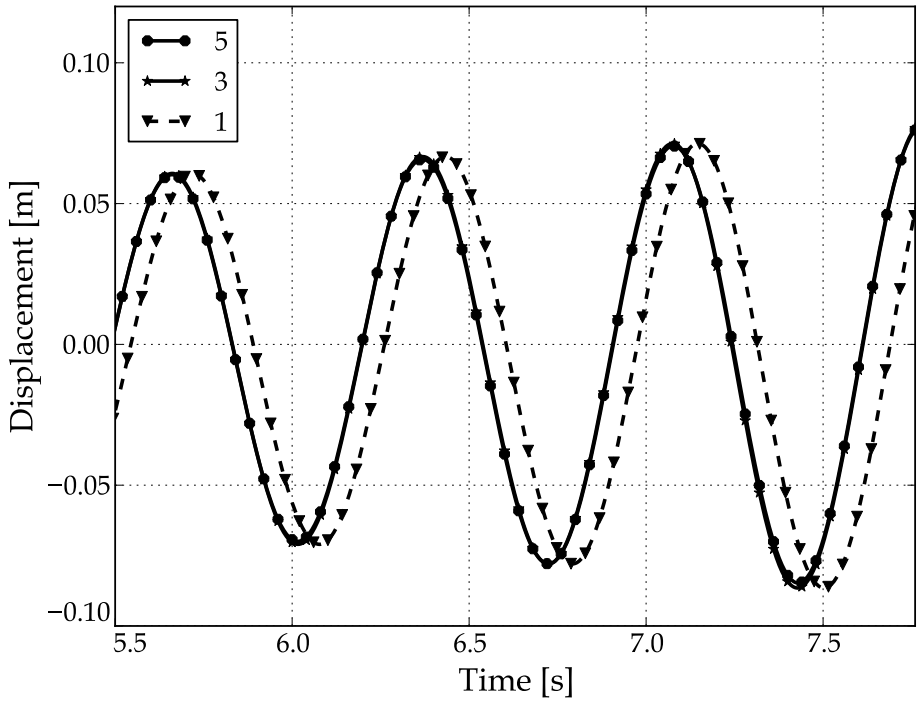

Figure D.2: Enlarged view of the stagger-iteratation sensitivity test

Appendix E

CFD boundaries

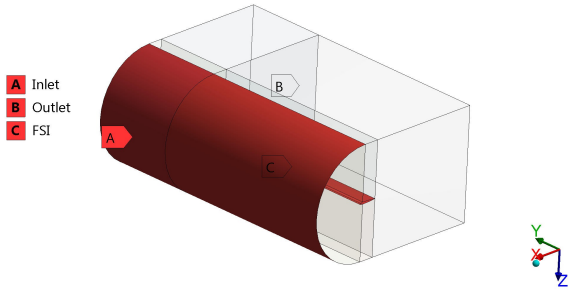

(a)

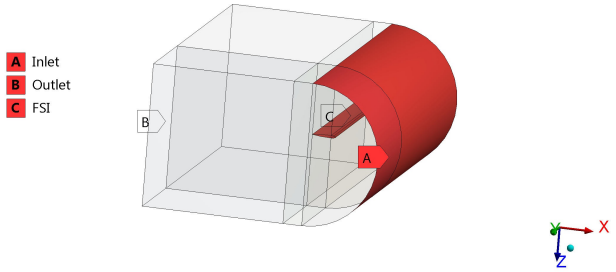

(b)

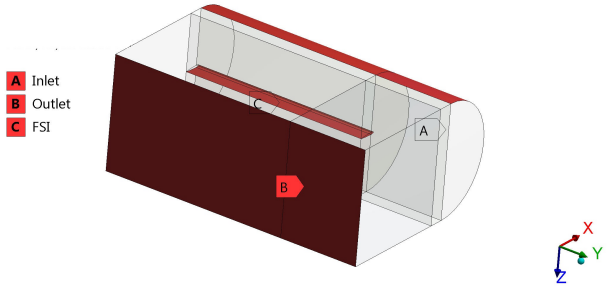

(c)

Figure E.1: CFD inlet, outlet and FSI boundaries

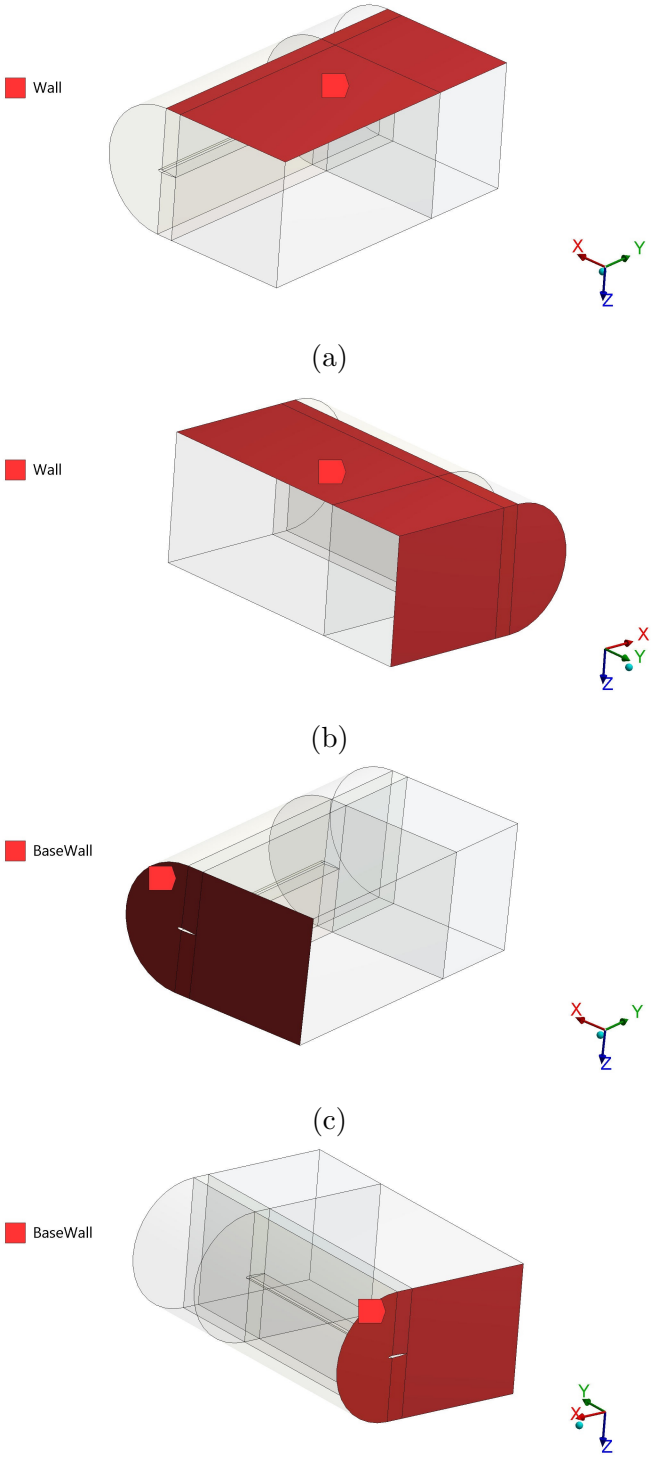

Figure E.2: CFD wall and basewall boundaries

List of References

[1] Riegels: *Aerofoil Sections*. 1st edn. Butterworths, London, 1961.

[2] Geothert, B.H.: *Transonic Wind Tunnel Testing*. 1st edn. Pergamon Press LTD, 1961.

[3] Science Learning: Wing aspect ratio. 2011.
Available at: http://sciencelearn.org.nz/Contexts/Flight/Science-Ideas-and-Concepts/Wing-aspect-ratio

[4] Moir, I. and Seabridge, A.: *Aircraft Systems: Mechanical, Electrical, and Avionics Subsystems Intergration*. The American Institute of Aeronautics and Astronautics, Inc., 2008.

[5] Civil Air Patrol: Fixed-wing aircraft primary controls. 2007.
Available at: http://www.cap-ny153.org/aircraftcontrols.htm

[6] Versteeg, H.K. and Malalasekera, W.: *An introduction to computational fluid dynamics : the finite volume method*. Pearson Education Ltd, Harlow, England New York, 2007. ISBN 9780131274983.

[7] Brandsen, J.D.: Prediction of axial compressor blade vibration by modelling fluid-structure interaction. 2013.

[8] Kulakowski, B. *et al.*: *Dynamic modelling and control of engineering systems*. Cambridge University Press, Cambridge New York, 2007. ISBN 9780521864350.

[9] Franklin, G. *et al.*: *Feedback control of dynamic systems*. Pearson, Upper Saddle River, N.J. Harlow, 2010. ISBN 978-0-13-500150-9.

[10] Pierson, S.H.: Composite rotor design for a hydrokinetic turbine. 2009.

[11] Lakin, G. and Haynes, J.: *Flutter and Aeroelastic Stability*. 1997.

[12] Scanlan, R.H. and Rosenbaum, R.: *Introduction to the study of Aircraft Vibration and Flutter*. The Macmillan Company., 1951.

[13] Garrick, I. and Reed III, W.H.: Historical development of aircraft flutter. *Journal of Aircraft*, vol. 18, no. 11, pp. 897–912, 1981.

[14] De Marqui Junior, C. *et al.*: Design of an experimental flutter mount system. *Journal of the Brazilian Society of Mechanical Sciences and Engineering*, vol. 29, no. 3, pp. 246–252, 2007.

[15] Wan, Z. *et al.*: Static aeroelastic analysis of a high-aspect-ratio wing based on wind-tunnel experimental aerodynamic forces. *Science China Technological Sciences*, vol. 54, no. 10, pp. 2716–2722, 2011.

[16] Marretta, R.M. and Marino, F.: Wing flutter suppression enhancement using a well-suited active control model. 2007.

[17] Jian, Z. and Jinwu, X.: Nonlinear aeroelastic response of high-aspect-ratio flexible wings. *chinese Journal of Aeronautics*, vol. 22, no. 4, pp. 355–363, 2009.

[18] Bisplinghoff and Raymond: *Principles of Aeroelasticity*. Dover Publications, New York, 1975. ISBN 9780486613499.

[19] Cook, R.D. *et al.*: *Concepts and applications of finite element analysis*. John Wiley & Sons, 2007.

[20] Schuster, D.M., Liu, D.D. and Huttsell, L.J.: Computational aeroelasticity: success, progress, challenge. *Journal of Aircraft*, vol. 40, no. 5, pp. 843–856, 2003.

[21] Fogell, N., Sherwin, S., Cotter, C.J., Iannucci, L., Palacios, R. and Pope, D.J.: Fluid-structure interaction simulation of the inflated shape of ram-air parachutes. In: *22th AIAA Decelerator Systems (ADS) Conference, Daytona Beach, Florida*. 2013.

[22] FLUENT Inc: Fluent 6.3 user's guide. *Fluent documentation*, 2006.

[23] Gidzak, V.M.: *A Method of Simulating Fluid Structure Interactions for Deformable Decelerators*. Ph.D. thesis, University of Minnesota, 2010.

[24] ANSYS Inc: Ansys system coupling user's guide. , no. 15.0, 2013.

[25] Vassen, J.-M., DeVincenzo, P., Hirsch, C. and Leonard, B.: Strong coupling algorithm to solve fluid-structure-interaction problems with a staggered approach. In: *7th European Symposium on Aerothermodynamics*, vol. 692, p. 128. 2011.

[26] Schmucker, H., Flemming, F. and Coulson, S.: Two-way coupled fluid structure interaction simulation of a propeller turbine. In: *IOP Conference Series: Earth and Environmental Science*, vol. 12, p. 012011. IOP Publishing, 2010.

[27] ANSYS Inc: Ansys coupled field analysis guide. *ANSYS, Inc*, , no. 10.0, 2005.

[28] Somenath, M. *et al.*: A theoretical formulation for flutter analysis of a typical subsonic aircraft wing (saras) using quasi-steady aerodynamic theory. 2005.

[29] Mashayekhi, M., Sedaghat, A. and Ghayour, M.: Linear flutter prediction for a cantilever wing model.

[30] Abbott, I.H. and Von Doenhoff, A.E.: *Theory of wing sections, including a summary of airfoil data*. Courier Corporation, 1959.

[31] Huang, R. *et al.*: Single-input/single-output adaptive flutter suppression of a three-dimensional aeroelastic system. *Journal of Guidance, Control, and Dynamics*, vol. 35, no. 2, pp. 659–665, 2012.

[32] Waszak, M.R.: Modeling the benchmark active control technology wind-tunnel model for application to flutter suppression. *AIAA paper*, vol. 3437, 1996.

[33] ANSYS Inc: Ansys element reference. , no. 12.1, 2009.

[34] Inman, D.J.: *Engineering Vibration*. Pearson Education, Boston, 2014. ISBN 978-0-273-76844-9.

[35] Mohammadi, M.A. and Johari, H.: Computation of flow over a high-performance parafoil canopy. *Journal of Aircraft*, vol. 47, no. 4, pp. 1338–1345, 2010.

[36] Kays, W., Crawford, M. and Weigand, B.: *Convective Heat and Mass Transfer*. McGraw-Hill Higher Education, New York, 2005. ISBN 007-123829-8.

[37] Menter, F.R.: Two-equation eddy-viscosity turbulence models for engineering applications. *AIAA journal*, vol. 32, no. 8, pp. 1598–1605, 1994.

[38] Eleni, D.C. *et al.*: Evaluation of the turbulence models for the simulation of the flow over a national advisory committee for aeronautics (naca) 0012 airfoil. *Journal of Mechanical Engineering Research*, vol. 4, no. 3, pp. 100–111, 2012.

[39] ANSYS Inc: Ansys fluent user's guide. *ANSYS Inc*, , no. 12.0, 2009.

[40] ANSYS Inc: Ansys fluent theory guide. *ANSYS Inc*, , no. 15.0, 2013.

[41] Nestorović, T.N.: Active control of mechanical structures in research and education. *Theoretical and Applied Mechanics*, vol. 40, no. 2, pp. 203–221, 2013.

[42] Nestorović, T. and Trajkov, M.: Active control of smart structures-an overall approach. *Facta universitatis-series: Architecture and Civil Engineering*, vol. 8, no. 1, pp. 35–44, 2010.

[43] Martin, R. *et al.*: Robust multivariable flutter suppression for the benchmark active control technology (bact) wind-tunnel model. 1997.

[44] Skogestad, S. and Postlethwaite, I.: *Multivariable feedback control : analysis and design*. 2nd edn. John Wiley, Hoboken, NJ, 2005.

[45] Takacs, G. and Rohal-Ilkiv, B.: Direct closed-loop active vibration control system prototype in ansys. In: *INTER-NOISE and NOISE-CON Congress and Conference Proceedings*, vol. 244, pp. 1–12. Institute of Noise Control Engineering, 2012.

[46] ANSYS Inc: Ansys workbench scripting guide. , no. 15.0, 2013.

[47] ANSYS Inc: Ansys mechanical user's guide. , no. 14.5, 2012.

[48] Dillsaver, M.J.: *Gust Response and Control of Very Flexible Aircraft*. Ph.D. thesis, United States Air Force, 2013.

[49] Su, W., Cesnik, S. and Carlos, E.: Nonlinear aeroelasticity of a very flexible blended-wing-body aircraft. *Journal of Aircraft*, vol. 47, no. 5, pp. 1539–1553, 2010.